UNIVERSITY OF CALIFORNIA, IRVINE

Measurement of Charged Pions from Neutrino-produced Nuclear Resonance

DISSERTATION

submitted in partial satisfaction of the requirements for the degree of

DOCTOR OF PHILOSOPHY

in Physics

by

Clifford Simon

Dissertation Committee:

Prof. David Casper, Chair
Prof. Henry Sobel
Prof. Steven Barwick

2014

Table of Contents

List of Figures

List of Tables

Acknowledgements

This research has been supported by a U. S. Department of Education GAANN Fellowship and a U. S. Department of Energy Grant. Steven Dytman has guided this work in every aspect. Emmanuel Pascos is thanked for his comments on the theory section. Anthony Mann and Richard Gran are thanked for constant conversation on many aspects of this work.

In the software department, I am grateful to several collaborators. Trung Le has led our codevelopment of a persistance scheme for true Monte Carlo particles with rescattering information. Jyostna Osta has provided different algorithms for track and blob reconstruction, the effects of which on scattered pions are an ongoing part of the research. Integration of my parts of the software into the experiment's software framework has been guided by David Schmitz and Gabriel Perdue.

Overlap in the work with other students has of course been frequent. My original work on strip-to-strip calibration and alignment has been brought to perfection by Chris Marshall, and I have attempted to present it with these important additions noted; all this body of work had been inherited by me in turn from an initial track-based alignment study by Ben Ziemer. The reconstruction and analysis algorithms are not my individual work: they have grown from a lengthy cooperation between myself and Brandon Eberly. My stopped particle-I.D. took its inspiration from an alternative energy loss profiling algorithm that was first coded by Tammy Walton, and later refined by B. Eberly. Brian Tice, and Jeremy Wolcott, along with the staff at Fermilab, are thanked for computing support.

The Low Energy Neutrino Cross Sections page maintained by Durham University (http://hepdata.cedar.ac.uk/review/neutrino/index.html) contains a useful index of published results and figures, which I have consulted while assembling the section on cross section results from bubble chambers.

Curriculum Vitae

- *2004: B.A. (with Honors), University of California, Berkeley.*
- *2014: Ph.D., University of California, Irvine.*

Abstract of the Dissertation

Measurement of Charged Pions from

Neutrino-produced Nuclear Resonance

by

Clifford Simon

Doctor of Philosophy in Physics

University of California, Irvine, 2014

Prof. David Casper, Chair

A method for identifying stopped pions in a high-resolution scintillator bar detector is presented. I apply my technique to measure the axial mass M_A^Δ for production of the $\Delta(1232)$ resonance by neutrino, with the result $M_A^\Delta = 1.16 \pm 0.20$ GeV (68% CL) (limited by statistics). The result is produced from the measured spectrum of reconstructed momentum-transfer Q^2. I proceed by varying the value of M_A^Δ in a Rein-Sehgal-based Monte Carlo to produce the best agreement, using shape only (not normalization). The consistency of this result with recent reanalyses of previous bubble-chamber experiments is discussed.

Chapter 1 Introduction

The positive charged pion (π^+) and its antiparticle (π^-) are active on nuclei. (The last pion, the π^0, travels only $c\tau \approx 25$ nm in matter or vacuum before decaying electromagnetically, a length too short to react observably on matter.) This property originally facilitated the discovery of the pion by the observation of its capture upon a nucleus [1].

If the pion is a product of a scattering process to be measured, then pion reactivity can complicate the measurement in some types of detectors. Scintillator-bar detectors, dependent on ionization tracks left by charged particles at low angles, are easily confused by pion reinteractions in dense detector matter. The effect is also hard to simulate. Cross-sections of πA scattering have been measured [2] but it is not clear that detector Monte Carlos are interpolating the measurement correctly. It is analogous to the well-known problem in neutrino flux simulations of hadronic reinteraction in thick targets.

I present a method to identify stopped pion tracks in a high-resolution scintillator detector. This is based on detecting pion-like energy loss near the endpoint of a track. The non-stopping background can then be subtracted out of the sample. By using a pure stopping sample for a measurement, a clean track sample is achieved (but at a cost in statistics of the measurement). The classification of pion tracks as stopping or not stopping by energy loss near the endpoint, is a method that appears not to have been tried in scintillator detectors previously.

I apply my technique to measure the resonant axial mass M_A^Δ. The plan of

this thesis is, first, to review the theory of resonance production and establish the M_A^Δ problem. I review the results of previous experiments measuring the resonant axial mass through the shape of a distribution of momentum transfer Q^2. Afterward, I introduce the present detector and the data set I am working with. There I describe how I reconstruct events and how I subtract reinteracted-pion background. The distinctive result of this measurement technique is a very precise reconstruction of the hadronic mass W of the event. Finally I present my best measurement of the Q^2 shape. The axial mass will be extracted by varying M_A^Δ in the Monte Carlo to produce the best agreement in shape.

The second chapter describes the MINERvA detector. I include here descriptions of the strip-to-strip calibration procedure, and the detector alignment. These came from my original service work in the MINERvA Collaboration and I leave them here as a reference for any parts that may have escaped documentation elsewhere.

1.1 Theory of Resonance Production

The distribution of matter within a hadron is represented by its form factors. With the arrival of high intensity νA (neutrino-nucleus) scattering, it becomes more possible to see *axial-vector* form factors, as these form factors are inaccessible to other types of scatterers. One hadron of interest is the $\Delta(1232)$ nuclear resonance. This resonance is an isospin $I = 3/2$ multiplet, coming in four varieties of charges ($\Delta^-,\ \Delta^0,\ \Delta^+,\ \Delta^{++}$): each variety decays to πN, where the nucleon N stands for either proton or neutron. This lightest reso-

nance provides an interesting probe of baryon physics. In addition, as resonant pions are a background to neutrino oscillation experiments, there is heightened interest in the resonance cross-section for neutrinos.

This theory section will outline the origin and meaning of each form factor for Δ-production by lepton scattering. A large number of Lorentz-allowed form factors will be reduced to only two *significant* and *independent* form factors. The derivation, to be sketched here, parallels the easier but better-known derivation of the Rosenbluth formula for electron-proton scattering. Compared to *ep* scattering, Δ-production substitutes a spin-3/2 fermion for the proton on the final side; additionally, it uses the weak rather than the electromagnetic interaction. Both differences greatly inflate the initial number of terms.

The derivation begins with the most general matrix element (M.E.) allowed by Lorentz invariance: this introduces a number of form factors not necessarily independent from one another. Regrettably, the most general M.E. is long enough that one searches for a way to abbreviate. On a single line, utilizing the accepted symbols for its eight Lorentz-allowed form factors, the entire M.E. is spelled out in Eq. (3.58) of reference [3]—the interested reader is encouraged

$$C_3^V(0) = \quad 2.13$$
$$C_4^V(0) = -1.51$$
$$C_5^V(0) = \quad 0.48$$

$$M_V = 0.84 \text{ GeV}$$

Table 1.1: *Vector form factors from electron scattering,* neglecting modifications to the dipole form. Values are taken from Eq. (IV.20) of reference [11].

to look there for the complete details. For our purpose, we will adopt an expedient method (from [9]) and write explicitly just the hadronic current, since the other parts (the leptonic current) are familiar, and not enlightening to write in full detail.

We will approach the general M.E. in the following manner. For lepton-nucleon scattering in the channel $\ell\, N \to \ell'\, \Delta$, we may begin with the matrix element in this form,

$$\begin{aligned} M(p,p',k,k') &= {}_{\rm out}\langle \ell'(k')\, \Delta(p') \,|\, \ell(k)\, N(p)\rangle_{\rm in} \\ &= \frac{G}{\sqrt{2}} \left(\bar{\psi}_{\ell'}\gamma^{\mu}(1-\gamma_5)\psi_{\ell}\right) \langle \Delta | V_{\mu} - A_{\mu} | N\rangle \end{aligned}$$

and work on the hadronic side one term at a time. The vector part of the hadronic current is given in [9] as

$$\begin{aligned} \langle \Delta(p')|V_{\mu}|N(p)\rangle = f(W) \\ \left\{ \bar{\Psi}_{\mu}(p') a_{\lambda} q^{\lambda} - \bar{\Psi}_{\lambda}(p') q^{\lambda} a_{\mu} + \bar{\Psi}_{\mu}(p') C_6^V(q^2) \right\} \gamma_5 \psi(p) \end{aligned}$$

where $q = p - p'$, a_{λ} is shorthand for

$$a_{\lambda} = \frac{C_3^V(q^2)}{m_N}\gamma_{\lambda} + \frac{C_4^V(q^2)}{{m_N}^2} p'_{\lambda} + \frac{C_5^V(q^2)}{{m_N}^2} p_{\lambda},$$

$f(W)$ is a Berit-Wigner function for the width of the resonance (with $W = \sqrt{p'_{\mu}p'^{\mu}}$ standing for the resonance mass), Ψ_{μ} is the Rarita-Schwinger spinor for the resonance, and ψ is the Dirac spinor for the nucleon.

This step has established four vector form factors $C_3^V \ldots\ C_6^V$. Notice that we have not used the lepton flavor. This is significant for *measuring* the

vector form factors: in the case of all isospin $I = 3/2$ resonances, the $\Delta(1232)$ resonance included, the C_i^V form factors measured by $\nu\, N$ and $e^-\, N$ scattering are identically the same (see reference [11]).

Next, the number of independent form factors deflates because of considerations beyond just plain Lorentz invariance. To achieve simplification we must consider all other kinds of constraints, both exact and approximate. According to the conserved vector current (referred to as CVC) imposed by the Lagrangian, C_6^V is forced to be exactly zero. According to the quark model, the $N \to \Delta$ transition is magnetic dipole. In the approximation of magnetic dipole dominance, $C_5^V \approx 0$ and $C_4^V \approx -(m_N/W)C_3^V$ (these approximate constraints are derived for the $\gamma\, N \to \Delta$ case in [4]). The literature takes C_3^V as the independent form factor. (Since each of the three nonzero form factors $C_3^V \ldots C_5^V$ can be extracted from electron scattering, some papers like [11] treat them as all independent.)

When the leptonic scatterer is electron, the interaction is only vector and only the vector form factors contribute. As stated previously, the electron and neutrino form factors are identical, meaning the vector form factors measured in electron experiments may be substituted directly into the neutrino M.E. The following approximation is interesting: at very small momentum transfers $|q^2| \lessapprox 0.35\ \mathrm{GeV}^2$, the vector contribution σ^V to the neutrino cross-section is directly proportional to an electromagnetic cross-section, as

$$\left(\frac{d^2\sigma}{dQ^2\, dW}\right)^V = \frac{G^2}{\pi}\frac{3}{8}\frac{Q^4}{\pi\alpha^2}\left(\frac{d^2\sigma}{dQ^2\, dW}\right)^{\mathrm{em}}$$

(see [9, Fig. 5]). In this approximation, vector/axial-vector interference is

neglected. To get from the approximate to the rigorous result, reference [11] describes the complete extraction of each C_i^V from electromagnetic scattering, with results summarized in Table 1.1. (Magnetic dipole dominance constrains C_3^V and C_4^V to have approximately the same mass parameter. In the formalism of Ref. [11], each form factor's exact mass parameter, if different than 0.84 GeV, is accounted for in modifications from exact dipole form.)

Finally, we repeat this procedure for the axial-vector part of the hadronic current. Starting again with every term allowed by Lorentz invariance, the axial-vector current takes the form

$$\langle \Delta(p')|A_\mu|N(p)\rangle = f(W)\left\{\bar{\Psi}_\mu(p')b_\lambda q^\lambda - \bar{\Psi}_\lambda(p')q^\lambda b_\mu \right. \\ \left. + \bar{\Psi}_\mu(p')C_5^A(q^2) + \bar{\Psi}_\lambda q^\lambda q_\mu \frac{C_6^A(q^2)}{m_N^2}\right\}\psi(p)$$

where b_λ is shorthand for

$$b_\lambda = \frac{C_3^A(q^2)}{m_N}\gamma_\lambda + \frac{C_4^A(q^2)}{m_N^2}p'_\lambda.$$

Now this establishes four more axial-vectors form factors $C_3^A \ldots C_6^A$. Again we pare down the number of independent form factors. One constraint arises from partially conserved axial current ($PCAC$), the property of the free quark Lagrangian being symmetric under the group of axial-vector rotations, except for its mass terms. The $PCAC$ constraint is $C_6^A = -m_N^2 C_5^A/(q^2 - m_\pi^2)$, derived (for example) in [11, §A.1]. A unique feature of this constraint is that is also allows us to evaluate the form factor numerically for one value of q^2. The limit $q^2 \to 0$ can be taken, with the result that $C_5^A(0) = 1.2$. This dimensionless

value is a combination of experimentally known constants (the pion decay constant, and a transition amplitude for $\Delta \to \pi\, N$), as explained fully in the reference.

Recalling how the vector form factors were reduced, we were next able to utilize magnetic dipole transition dominance to derive more (approximate) constraints. This does not yield any axial-vector constraints: we must fall back to more general considerations if more axial-vector constraints are to be discovered. Happily, *causality* provides two more constraints. The interested reader can go to reference [5] for a general discussion of causality in πN reactions.

In very brief summary, causality implies a disperson relation, including as a special case the Optical Theorem relating the total cross-section to the imaginary part of the scattering amplitude at $\theta = 0$. The general dispersion relation cannot be solved exactly. From approximate solutions to dispersion theory, it is found that $C_3^A \approx 0$ and $C_4^A \approx -C_5^A/4$: these form factor relations seem to have been introduced by S. L. Adler [6], and were followed in all later references ([9, 10, 11]). The literature takes C_5^A as the independent form factor.

One may now ask what function of q^2 each form factor is. Since q is spacelike, $q^2 \leq 0$ and we define $q^2 = -Q^2$ in order to use the nonnegative expression Q^2 in our formulas. Now, in the approximation that the Δ is a point particle, the form factors would be exact dipoles, as below:

$$\left.\begin{aligned} C_3^V(Q^2) &= C_3^V(0)\,(1 + Q^2/M_V^2)^{-2} \\ C_5^A(Q^2) &= C_5^A(0)\,(1 + Q^2/M_A^2)^{-2} \end{aligned}\right\} \text{point approximation}$$

since the dipole is related to the Fourier transform of the delta function $\delta^3(\vec{x})$.

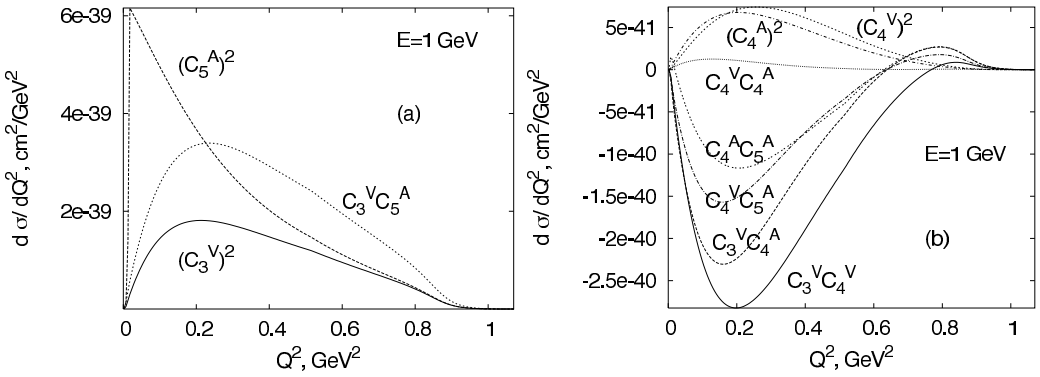

Figure 1.1: *Dominance of C_3^V and C_5^A.* The cross-section is evaluated using Fermi's golden rule, with $M_A = 1.05$ GeV and neutrino energy $E_\nu = 1$ GeV, shown on a coarse scale (a) and a fine scale (b). Plots from [10].

The two scale factors, and the numbers M_V (vector mass) and M_A (axial mass) are *undetermined parameters*. Theoretical models propose a variety of other functional forms, all approximately dipole, to account for the Δ's spatial extension; even in the spatially-extended case, however, M_V and M_A are still considered the first-order parameters along with the overall scales.

At last, Fermi's golden rule converts the M.E. squared into a differential cross-section $d\sigma/dQ^2$. This program is carried out completely in each of the references [9, 10, 11]; the reader is encouraged to refer to these self-contained papers for details. The result of matrix element squaring is presented visually in Fig. 1.1. The notable result is that C_3^V and C_5^A (and their interference term) contribute an order of magnitude more compared to the other terms and cross-terms.

1.2 Spectra of Momentum Transfer Q^2 from Previous Experiments

Since the vector form factors are known according to Table 1.1, and $C_5^A(0) = 1.2$ is established by *PCAC*, the neutrino experiment's immediate task is discovering the axial mass M_A in C_5^A. In principle, this is accomplished by fitting the measured differential cross-section $d\sigma/dQ^2$, where M_A is the free parameter of the fit.

A limited number of Q^2 spectra have been measured for neutrino resonance production. This measurement has been performed with a variety of detector technologies from 1978 to the present. Bubble chamber experiments have employed a magnetic field, whereas subsequent experiments have used non-magnetized technology. The strategy of event reconstruction changes considerably when the aid of magnetic field is removed.

In each of these experiments the measured differential cross-section $d\sigma/dQ^2$ is an average over a wide spectrum of neutrino energy E_ν, except the MiniBooNE experiment, which separates its $d\sigma/dQ^2$ into bands of E_ν.

Bubble Chamber

Cross-sections have been measured by bubble chambers at FNAL [12], CERN [13], Argonne [14], and Brookhaven [15]. The figures below show each experiment's result.

Event reconstruction in each of the bubble chamber experiments is performed by fitting of the event to several hypotheses, each hypothesis being an exclusive reaction channel. The Argonne experiment, for example, considers

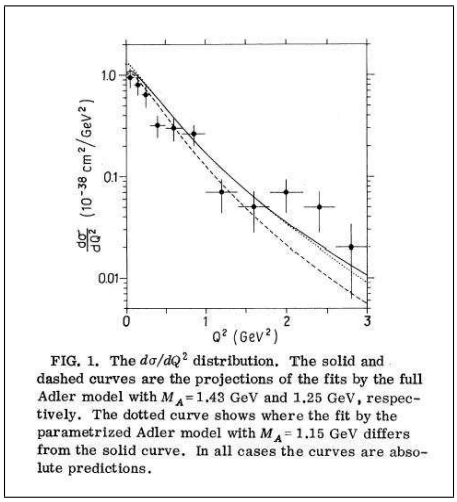

FIG. 1. The $d\sigma/dQ^2$ distribution. The solid and dashed curves are the projections of the fits by the full Adler model with $M_A = 1.43$ GeV and 1.25 GeV, respectively. The dotted curve shows where the fit by the parametrized Adler model with $M_A = 1.15$ GeV differs from the solid curve. In all cases the curves are absolute predictions.

Figure 1.2: FNAL *bubble chamber* $d\sigma/dQ^2$. From 138 events passing the fit to $\nu\, p \to \mu^-\, p\, \pi^+$, taken in the FNAL hydrogen bubble chamber. The cut $M(\pi^+ p) < 1.4$ GeV is applied. The spectrum of E_ν turns on at 5 GeV, is flat from 10 to 30 GeV and falls off until 100 GeV. Original figure from [12].

fits to $\nu D \to \mu^-\, p\, \pi^+\, n_s$, $\nu D \to \mu^-\, p\, \pi^0\, p_s$ and $\nu D \to \mu^-\, n\, \pi^+\, p_s$ (where D is the target deuteron and n_s or p_s is the spectator nucleon). The hypothesis with the greatest χ^2 probability is taken, but if the probability does not exceed some small lower bound, typically 1%, the fit is bad and the event is rejected.

These magnetized experiments were insensitive to pion reinteractions so long as the reinteraction occurred sufficiently far from the vertex. Only a primary segment of sufficient length is necessary when momentum is measured with the help of the magnetic field.

Scintillator Bar Detector

This type of detector is constructed of planes of scintillating bars, with air space or additional material between planes. The planes are normal to the beam direction; the more finely spaced the planes and bars, the higher the

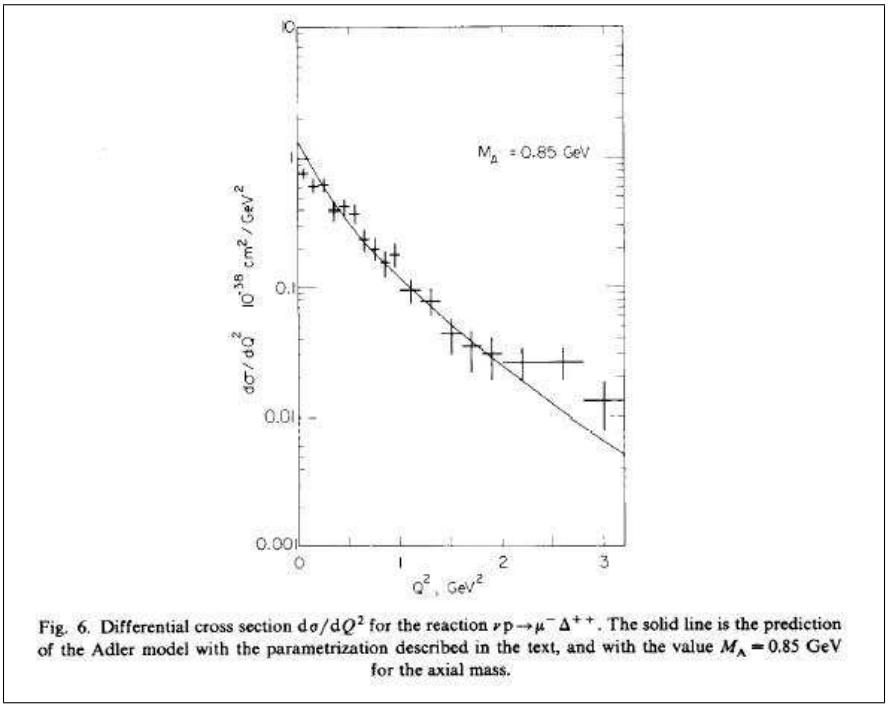

Fig. 6. Differential cross section $d\sigma/dQ^2$ for the reaction $\nu p \to \mu^- \Delta^{++}$. The solid line is the prediction of the Adler model with the parametrization described in the text, and with the value $M_A = 0.85$ GeV for the axial mass.

Figure 1.3: CERN *bubble chamber* $d\sigma/dQ^2$. From 551 events on hydrogen. The cut $M(\pi^+ p) < 1.4$ GeV is applied. Neutrino energy E_ν ranges from 5 to 200 GeV. Original figure from [13].

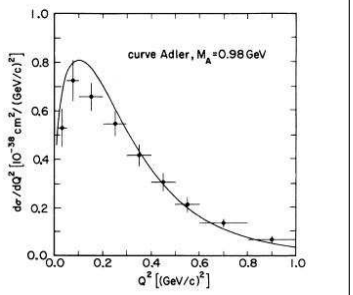

FIG. 11. Differential cross section $d\sigma/dQ^2$ evaluated with the selections $0.5 \le E_\nu < 6.0$ GeV and $M(p\pi^+) < 1.4$ GeV. The curve is the flux-averaged prediction of the Adler model with the dipole form factor and $M_A = 0.98$ GeV.

Figure 1.4: *Argonne bubble chamber* $d\sigma/dQ^2$. From 871 events on deuterium, fit as $\nu D \to \mu^- p \pi^+ n_s$. Original figure from [14].

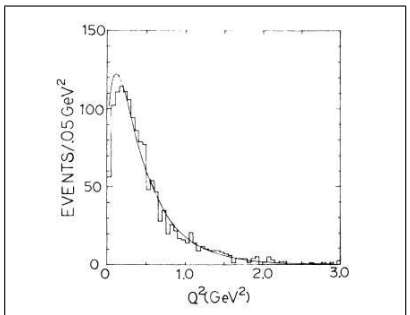

FIG. 10. Q^2 distribution for $\mu^- p \pi^+$ events with $M(p\pi^+) < 1.4$ GeV for $0.5 < E_\nu < 6.0$ GeV. The solid curve is the prediction of the Adler model with $M_A = 1.28$ GeV normalized to the events with $Q^2 > 0.02$ GeV^2.

Figure 1.5: *Brookhaven bubble chamber* dN/dQ^2. From 1384 events on deuterium. The E_ν spectrum peaks at 1.2 GeV. Original figure from [15].

detector resolution.

The non-magnetized SciBooNE experiment [16] uses a scintillator bar detector (the SciBar detector) with rectangular strips. The strip cross-sectional dimensions are 1.3 cm $\times$ 2.5 cm. The experiment has produced a dN/dQ^2 spectrum for Δ resonance production by neutrino (Fig. 1.6), but not as a stand-alone result however. It was incidental to their analysis for *coherent* pion production (and this means the resonant events in this case are actually the *background*). For both resonant and coherent pion production, this experiment improves pion identification in scintillator detectors by use of the energy loss on the pion track.

In SciBooNE's pion scenario, the muon is identified by penetration into a muon range detector (M.R.D.). The recoiling nucleon is not energetic enough to penetrate many bars, so its presence is tagged by extra activity seen near the vertex. The second track is therefore expected to be the pion. The experiment tags pions through the "muon confidence level," MuCL, which measures how similar the hits are to the expected hit from a minimum-ionizing particle (MIP), which is calibrated to muons. A charged pion is somewhat close to minimum-ionizing, but a proton is not at all (Fig. 1.6, left).[1] So the MuCL acts as a p/π separator. The pion candidate is allowed to exit the SciBar detector, as the MuCL score does not place special emphasis on the track endpoint.

Coherent events (the signal) are separated from resonant events (the background) by the absense of energy at the vertex. Resonant event vertex energy should be consistent with a recoiling nucleon. The recoiling proton of a resonance event is typically not energetic enough to leave a track in the SciBar

[1]This I.D. is insensitive to pion reinteraction in the scintillator, since to first approximation, if the pion does not stop, it looses its Bragg rise and looks only more MIP-like.

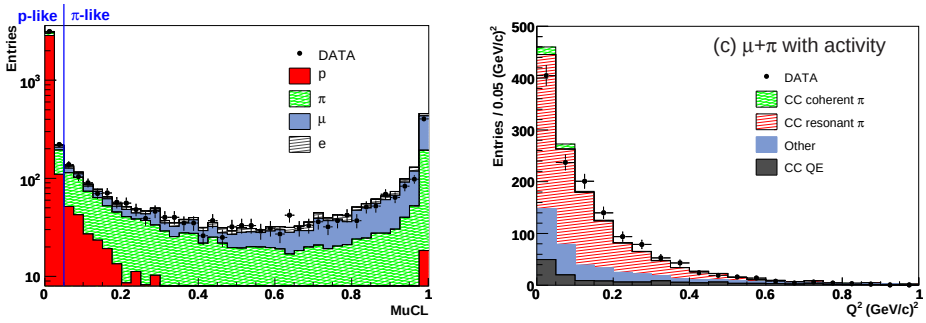

Figure 1.6: *SciBooNE particle I.D. and* dN/dQ^2. From [16].

detector.

Although the pion is I.D.'d effectively, no attempt is made to measure its energy. This measurement was not needed because the SciBooNE analysis computes the coherent momentum transfer Q^2 *without* using the pion four-vector as input. Resonant events can be reconstructed in a variety of ways, even from the muon alone if the resonance mass is assumed, but they cannot be reconstructed correctly by the C.C.Q.E. hypothesis[2]. This is no mistake, though, since SciBooNE has (obviously) no need to produce the real kinematics for its background.

Čerenkov Radiation Detector

The MiniBooNE experiment [17] is the current leader of the pack in neutrino-produced resonance cross-section. This non-magnetized experiment does not have an external muon I.D., therefore, both the pion and the muon are identified by the combination of a non-showering Čerenkov cone plus a time-delayed

[2]The SciBooNE coherent reference [16] uses Monte Carlo to argue that the momentum transfer Q^2 produced by a charged-current quasi-elastic (C.C.Q.E.) hypothesis is close enough for coherent. This argument appears to succeed despite that coherent events are nothing like C.C.Q.E. physically.

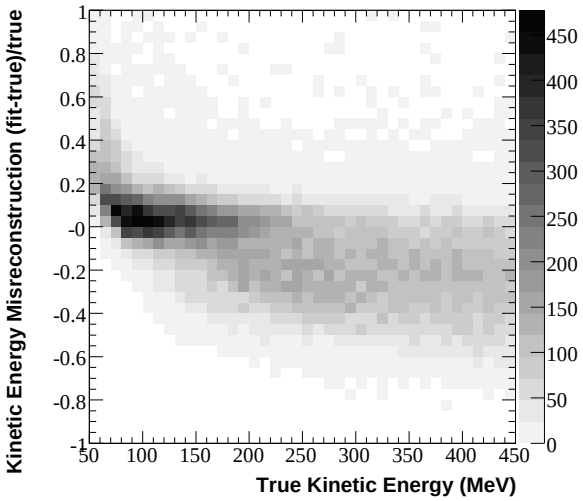

Figure 1.7: *MiniBooNE error in T_π.* From [17].

Michel electron. The event is fit to the hypothesis of $\nu\, N \to \mu^-\, \pi^+\, N'$.

Čerenkov cones from muon and charged pion are indistinguishable. Confusion of the pion and the muon would ruin the estimation of momentum transfer Q^2, by causing the appearance that most of the momentum is transfered to the hadrons. So as not to error in this way, MiniBooNE requires the π^+ to scatter once in the mineral oil, and produce a secondary cone. This scatter serves as the pion I.D. tag. (The event is then composed of three non-showering cones: muon, primary pion, and rescattered pion. The N' is invisible.) This method of reconstruction is no longer insensitive to pion reinteraction. Quite the other way, a specific topology of reinteraction is necessary.

Pion energy measurement with reinteractions is a challenge to non-magnetized experiments, and MiniBooNE's case typifies this universal quest. In MiniBooNE's case, the reconstructed energy is centered on the true kinetic energy up to 150 MeV, but wider and not centered for higher true kinetic energy; the center of reconstruction comes out 20% too low for higher energy

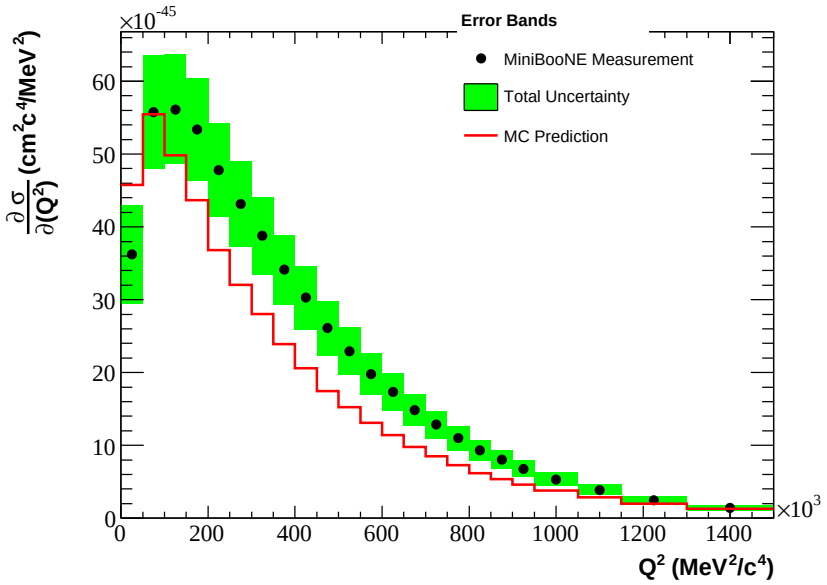

Figure 1.8: *MiniBooNE $d\sigma/dQ^2$, flux-averaged.* From [17].

pions (Fig. 1.7). The muon energy reconstruction, which is more important,[3] is narrow and centered. Misreconstruction effects are unfolded out of the data for the final result. The differential cross-section in bins of E_ν from 48,322 events is reproduced in Fig. 1.8 and Fig. 1.9.

1.3 Conclusions about M_A^Δ from Momentum Transfer Spectra

From the differential cross-sections from existing experiments, a value of the resonant axial mass M_A^Δ close to 1 GeV is indicated. This value can be visualized as in the neighborhood of the mass of a proton. But this estimate is a rough one. It is difficult to find a single, precise value of M_A^Δ that satisfies all

[3]The error from T_π is typically diminished when propagated into E_ν, W, or Q^2, since T_π enters into W or Q^2 only through $E_\nu = E_\pi + T_N + E_\mu$. Typical events have $T_\pi \ll E_\mu$, so the E_ν error is mostly explained by the muon.

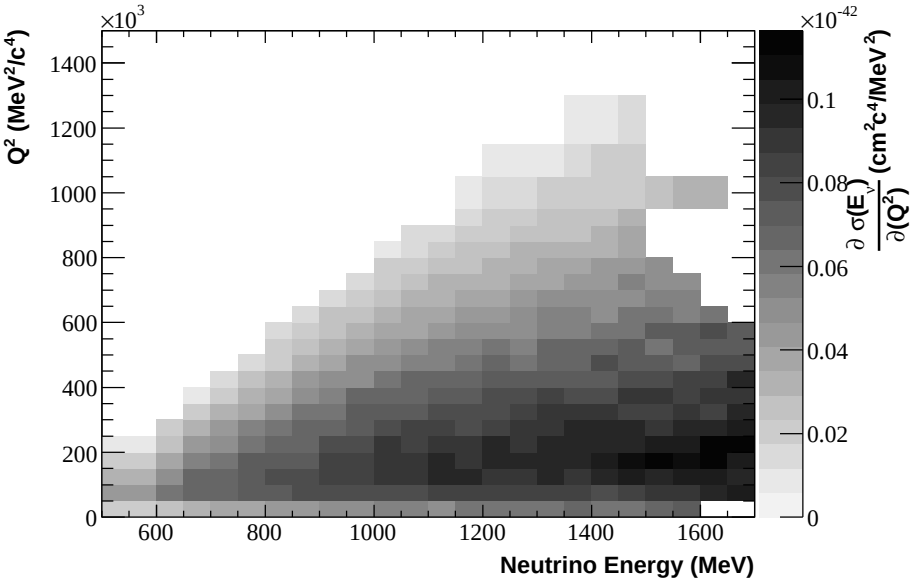

Figure 1.9: *MiniBooNE* $d\sigma/dQ^2$. From [17].

the experiments.

O. Lalakulich and E. A. Pascos, in reference [10], using modifications to the dipole shape as suggested by resonant $e^- N$ scattering, M_A^Δ. These authors find that the Brookhaven cross-section is closely predicted by $M_A^\Delta = 1.05$ GeV. Argonne, on the other hand, is predicted by $M_A^\Delta = 0.84$ GeV if the same modified dipole is used. The experiments at higher neutrino energy—FNAL and CERN—are less sensitive to the axial mass, and appear to fit well with either value. These conclusions typify the problems with extracting the resonant axial mass with existing data.

We conclude that current experimental data gives the resonant axial mass $M_A^\Delta \approx 1$ GeV. The MiniBooNE cross-section, a current topic of discussion at the time of this writing, is well-situated to improve the situation. My intention using MINERvA data is to develop a pion reconstruction that is complimentary

to MiniBooNE's (focused on unreacted rather than reacted pions), and sensitive to as few as possible of the systematics associated with reinteraction. My plan in the subsequent chapters will explain this further.

1.4 Experiments Measuring the Total Resonance Cross-Section

The differential cross-section $d\sigma/dQ^2$ is a difficult measurement. More data points are available from measurements of the total resonance cross section $\sigma^{\Delta}(E)$ as a function of the neutrino energy E in the lab frame.

The total cross section $\sigma^{\Delta}(E)$ can also be used to measure the axial mass M_A^{Δ} through its functional dependence on E. In this scenario, however, states Reference [8], "the numerical value of M_A^{RES} $[= M_A^{\Delta}]$ is vastly dependent of the particular dynamic model for the resonance production."

Ref. [8] has reviewed all the available bubble-chamber data for $\sigma^{\Delta}(E)$. Results from ANL, BNL, FNAL, CERN and IHEP are included. A simultaneous fit has been performed to all the data using a model derived from Rein and Sehgal [7]. The result of this procedure is that under the assumptions of the modified Rein-Sehgal model, $M_A^{\Delta} = 1.12 \pm 0.03$ GeV.

Chapter 2

Beam and Detector Description

The MINERvA detector [18, 19] is a non-magnetized scintillator bar detector. This chapter will outline the detector's main features as they are used in this thesis. For a complete detector description the reader is encouraged to rely on reference [19]. The detector is running in the NuMI beamline's Near Detector Hall at Fermi National Accelerator Laboratory.

The low energy (L.E.) configuration of the NuMI beam has been used to produce the events in this thesis. The MINERvA experiment's L.E. run lasted from 22 March, 2010 until 30 April, 2012. During this run, 2.99×10^{20} protons-on-target (P.O.T.) worth of beam exposure was delivered to the detector during its analysis livetime. After the L.E. run, the MINERvA experiment will continue running in other beam configurations.

2.1 Layout of the Beam, including Flux Estimation

The high-intensity neutrino beam is a marvel of modern engineering. The reader is encouraged to see Chapter 2 of Reference [18] for a complete and very accessible description of Fermilab's NuMI beam, from the proton accelerator to the target, focusing, decay, and *in situ* monitoring. I will give a briefer description of NuMI here. For a review of neutrino beams in general, reference

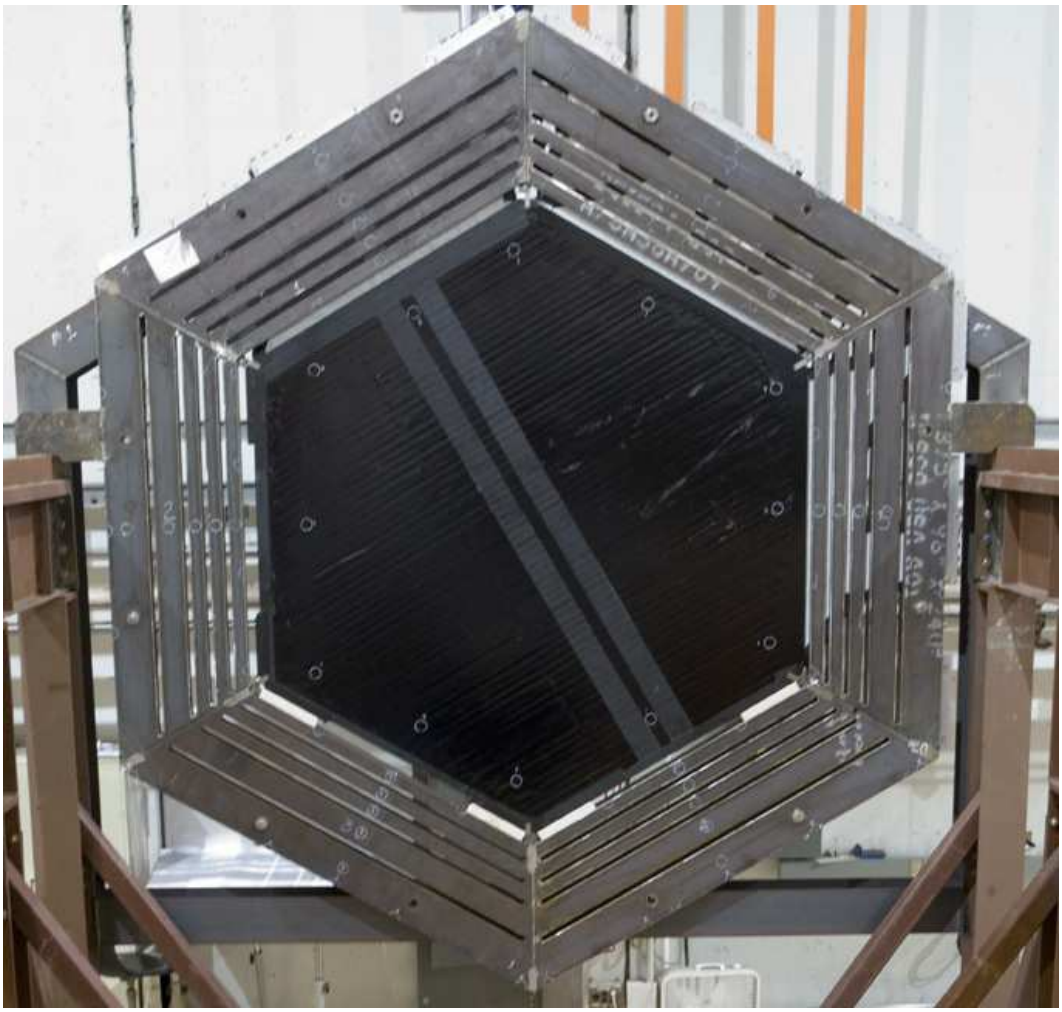

Figure 2.1: MINERvA *module.* Scintillator strips are seen in the black light-tight bag, center. The visible strips run in the slanted V direction (see Fig. 2.4 for the explanation of strip direction designations X/U/V.) The O.D. scintillators, optical cables and lead-plate absorbers of the ECAL are lacking. Photo from Fermilab Visual Media Services, Negative No. 07-0113-01D.

[21] is definitive.

To produce the neutrino beam, accelerated protons are aimed at a graphite cylinder target. Protons with energy $E = 120$ GeV in the lab frame react with carbon nuclei in the target. Pions and kaons are produced. These products exit the target cylinder transversely, and possibly reinteract on their way out.

Charged pions and kaons exiting the target are collected by the magnetic field of the horn system. The horns are devices meant to select singly charged particles ($q = +e$) at a fixed momentum p, and deflect all others. The NuMI horn system consists of two horns. Each horn has a double-parabolic conductor shape.

Horns work in analogy to geometric optics. The "focal length" f of a double-parabolic horn is given as

$$f = \frac{1}{e}\frac{\pi}{\mu_0 a I}p \tag{2.A}$$

where e is the fundamental charge, a is a parameter describing the horn's conductor shape as $z = ar^2$, I is the current setting up the horn's magnetic field, and p is the focused momentum [21, Eq. (12)]. Once the target-horn distance f has been determined, I can be adjusted to select the focused momentum p.

The second horn of NuMI is situated at $f = 10$ m from the focal point, and its a parameters are given by $a = 0.1351$ cm^{-1} on the upstream side ($a = 0.2723$ cm^{-1} cm on the downstream side) [22]. When a double horn has different parabolas, the a referenced in Eq. (2.A) is effectively the mean of the two a's, so $a = 0.2$ cm^{-1} $= 20$ m^{-1} should be applied. The horn current is 185 kA for the L.E. configuration of the beam. Applying Eq. (2.A), the focused

momentum is found to be 4.4 GeV/c.

The first horn's focusing properties are not as easy to estimate as the second. The second horn of a two-horn system is usually for refocusing particles that for any reason escaped being focused by the first horn. In the L.E. configuration of NuMI, the target and the focal point are both inside the first horn. The geometric optics approximation (Eq. (2.A)) cannot apply to the first horn, since the target and horn are overlapping. The focusing properties of the first horn need to be assessed using Monte Carlo (§4.1).

Focused pions and kaons head toward the evacuated decay pipe. These experience two-body leptonic decays, $\pi^+ \to \mu^+ \nu_\mu$ (and $K^+ \to \mu^+ \nu_\mu$). Any neutrinos that decay in the forward direction head toward the experiment hall. The charged particles (decay muons, and undecayed mesons) are stopped by a beam absorber.

The absolute flux is difficult to predict. "The prediction of the neutrino flux starting from the yield of secondary hadrons from a target is the bane of every neutrino experiment," states Reference [21]. The analysis I present is area-normalized, meaning it does not care about the absolute flux. The shape of the flux (only) will be important.

The estimate of the neutrino flux presented to MINERvA comes from a combination of methods. First, hadron production in the NuMI target can be estimated with hadron production experiments using similar thick targets. The flux shape used in this thesis is tuned to hadroproduction data from Fermilab experiment E118 [28] and CERN experiment NA49 [29]. Further constraints on the flux come from *in situ* monitoring. A flux shape prediction by *in situ* methods is shown in Fig. 2.2.

The key shape features of MINERvA's flux in the L.E. beam are its peak near $E_\nu = 3$ GeV, steep decline until 5 GeV and long tail. At the analysis stage, I reject events with reconstructed $E_\nu > 10$ GeV so most of the tail is not seen.

One final aspect of the beam is its timing. Protons are delivered to the beam target in spills lasting 10 μs. The absolute number of protons on target (P.O.T.) is measured once each spill. The number varies with time, as upgrades to the beam allow it to increase in intensity, but a typical value is 35×10^{12}. The spill rate is 2 Hz, resulting (from the detector data acquisition point-of-view) in a very short pulse of activity, followed by a long time available for

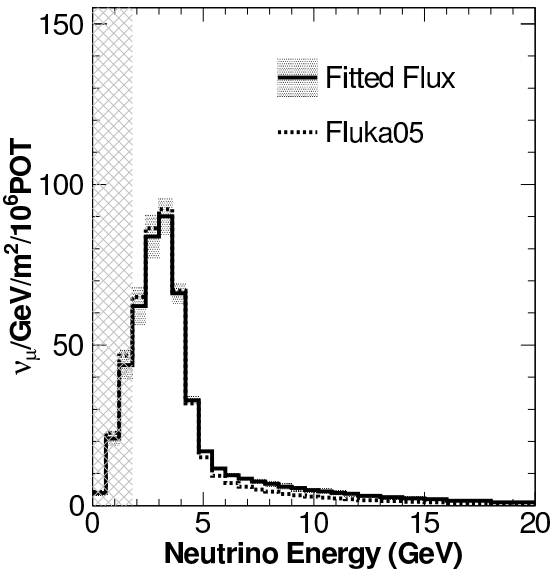

Figure 2.2: *Flux in the* NuMI *Near Detector Hall.* Figure from [23]. This figure shows a flux shape constrained by *in situ* muon monitors with different thresholds. The solid curve with errors uses estimated hadron production from monitor measurements (the hatched area is a region of extrapolation). The dashed curve is a separate Monte Carlo. The muon-antineutrino ($\bar{\nu}_\mu$) and electron-neutrino ($\nu_e,\ \bar{\nu}_e$) fluxes are not shown.

data transfer, at each spill of the beam.

2.2 Layout of the Detector

Longitudinally, the MINERvA detector is arranged as veto, targets, tracker, electromagnetic calorimeter (ECAL) and hadronic calorimeter (HCAL). The *tracker* layer, which is situated in the middle of the sandwich, is primarily composed of hydrocarbon scintillator and is the neutrino target for this analysis. Neutrino-produced pions must also stop within the tracker for this analysis, to allow their ionization to be fully measured in the tracker. The layout of MINERvA is shown in Fig. 2.3.

The MINOS Near Detector, a magnetized detector, serves as muon detector for the MINERvA experiment. The MINOS N.D. is located behind the rear face of MINERvA's hadronic calorimeter after a gap. (This arrangement of the muon detector is the cause of the 1.5 GeV threshold for muon energy.)

The MINOS N.D. itself is another scintillator-bar detector, with 152 scintillator planes and a toroidal magnetic field of average strength 1.3 T. The scintillator planes of MINOS are separated from one another by steel absorbers. The detailed layout of MINOS planes and absorbers is not critical for understanding this analysis, since the detector is only being used to measure the momentum of muons which have exited MINERvA (Fig. 2.5). Either the curvature of the muon in the magnetic field, or the range of the muon if stopped by the steel absorbers, can be used to measure the muon momentum. Details of the muon reconstruction can be found in §5.2.

This analysis uses mainly the tracker layer of MINERvA. The fiducial vol-

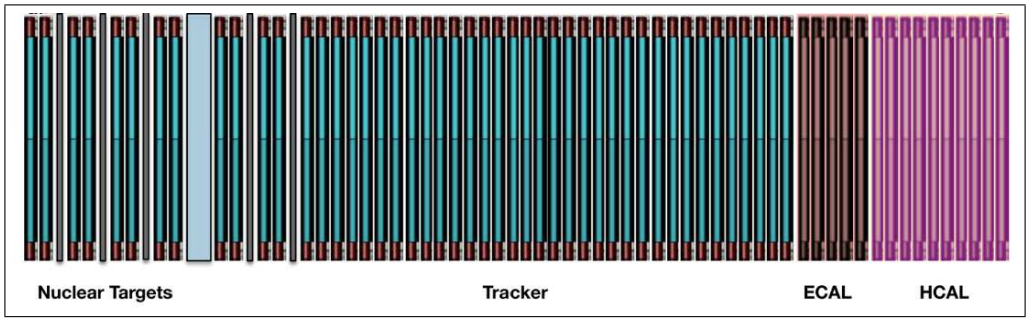

Figure 2.3: MINERvA *detector, top view.* Beam is left to right. The MINOS Near Detector (functioning as our muon detector), not shown, is after the HCAL. Diagram from [20].

Element	Atoms $\times 10^{23}$ per cm^2	Protons $\times 10^{23}$ per cm^2	Neutrons $\times 10^{23}$ per cm^2
H	0.903	0.903	.....
C	0.889	5.334	5.344
O	0.024	0.192	0.192
Cl	0.00189	0.0321	0.0349
Ti	0.00176	0.0387	0.0456
Si	0.00129	0.0118	0.0182
Al	0.00111	0.0144	0.0288
Sum		6.526	5.664

Table 2.1: *Plane composition (Tracker).* In the 85 cm fiducial apothem, each plane contributes 1.633×10^{28} target protons and 1.418×10^{28} target neutrons, for a total of 3.234×10^{30} target nucleons in 106 tracker planes. Column 2 is reproduced from reference [18, Table 3.1]. Column 4 uses isotope fractions from [41].

ume for my analysis contains 3.2×10^{30} target nucleons in the tracker planes (see Table 2.1 with caption). The pion must both start and stop in this layer. For charted particles, each plane presents a thickness at $\theta_{\mathrm{Det}} = 0$ of 2.02 g/cm^2 for energy loss. Of that thickness, 1.65 g/cm^2 is scintillator, and the remaining is passive material such as light-sealing bags.

Layers outside the tracker will play only a brief role in my analysis. The total hadronic energy in MINERvA including all layers will be relied upon to reject events with an extra pion. Extra π^0's, for instance, can be expected to light up the ECAL. Each other layer is different from the tracker by containing additional material. The targets layer, which is situated between veto and tracker, holds extra material at different mass numbers A, for experiments seeking the cross section A-dependence. ECAL has absorbers of lead, and HCAL has wider spacing of scintillator with absorbers of steel.

The beam is almost normal to the face of MINERvA (it is actually aimed 3.34 degrees downwards). Transverse to the beam, MINERvA appears as concentric hexagons. As one travels outward from the center, one sees a scintillator core, a middle ring of ECAL and an outer shell of HCAL. Scintillator extends up to 90 cm apothem. The ring of ECAL begins at 90 cm, and the ring of HCAL begins at 1 m. The outer shell of HCAL, also called the outer detector (O.D.), is also a supporting steel frame. The fiducial apothem is 85 cm, to allow some spacing between the event vertex and the edge of the lead in the ECAL.

Parallel scintillator strips make up the core of each plane (photo, Fig. 2.1). The plane has 127 triangular strips. When viewed from the front, the numbering of strips goes from right to left because positive x points to the *left* in beam's-eye view (y up, z into page) to preserve right-handedness. The 64$^{\mathrm{th}}$

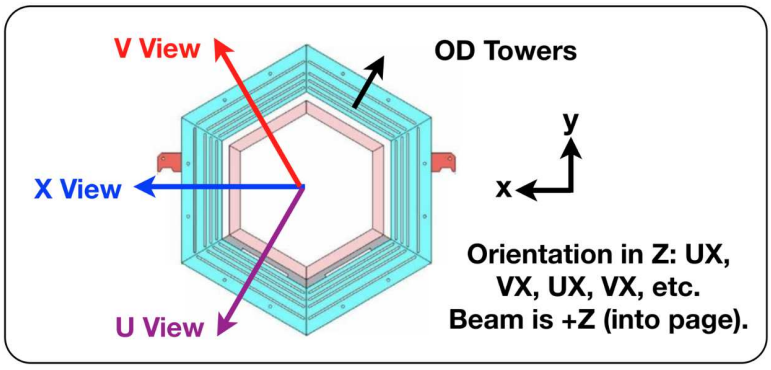

Figure 2.4: MINERvA *plane, beam's-eye view.* Arrows show the direction of increasing strip number for an X-plane, a U-plane and a V-plane. Strip numbers in the O.D. increase radially. Diagram from [20].

strip, the longest in the set, is always a diameter of the bounding hexagon.

In order to reconstruct tracks in three dimensions—the z-dimension and two transverse dimensions—planes are installed with alternating strip directions. With the bounding hexagon left invariant, the scintillator core can be rotated in 60° increments to produce three orientations or "views," named X, U and V (Fig. 2.4). As the orientation changes, the track transverse position is seen in different bases. X planes with vertical strips see in the x-direction while U and V planes see directions slanted at ±60°.

One important consequence of the layout is the minimum number of consecutive planes required to define a track. This number depends on the exact sequence and ordering of views. The tracker planes are installed with a fixed pattern of views. As one travels in the beam direction, no two views are consecutive but every even-numbered view is X, while the odd-numbered views alternate U and V. Nearest U's (for example) are separated by three intervening planes, an XVX sequence. According to this pattern, the minimum track length can be deduced. If *fewer than five* consecutive planes, a line is

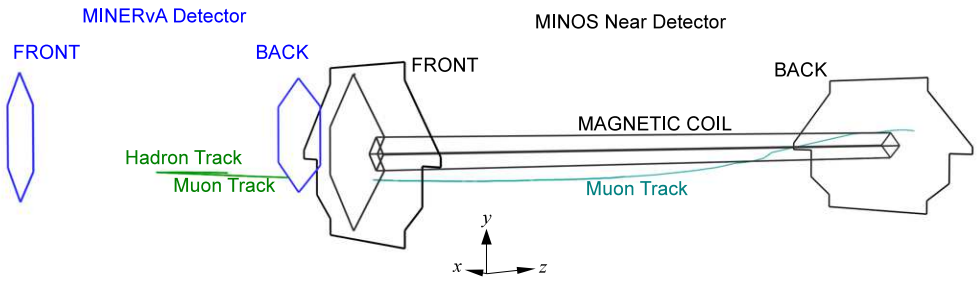

Figure 2.5: *The* MINERvA *and* MINOS *detectors,* in linear perspective. A muon track exiting the back of MINERvA (green) projects into a muon track entering and exiting the MINOS near detector (blue). This muon's energy can be found by its curvature in MINOS. (Diagram produced by the ARACHNE Display [40].)

not defined. Tracks of exactly five planes define a line always and colinearity sometimes—this is the result of a somewhat boring exercise of listing every 5-plane sequence. (Some 5-plane sequences have 3 of one view, but some do not.) If *six planes or more* consecutively, three X's are guaranteed and the colinearity test is always possible. In summary, a particle has to go about 6 planes, maybe 5 in extreme cases, before it can be a line. The threshold for hadron tracking is found here and turns out to be ≈ 60 MeV for pions.

Different coordinate systems are defined for the detector and for the beam, and care must be taken to distinguish them. What does a polar angle θ mean? In the detector system, θ_{Det} is the angle for calculating the length of material $L \sec\theta_{\text{Det}}$ presented to an ionizing track. In the beam system, on the other hand, θ is the angle for resolving a collision into its transverse and longitudinal momentum components, $p_T = p\sin\theta$ and $p_z = p\cos\theta$. Unless otherwise noted, position coordinates will be given in the detector system, but momentum vectors will be given in the beam system. Subscripts may be used

where confusion might arise.

2.3 Detector Optical and Electronic System

Each MINERvA scintillator strip has an optical fiber running down its center. The fiber is mirrored on the bottom (negative y) end. At the top (positive y) end, the fiber is routed by a series of optical connectors to one channel of a 64-channel photomultiplier tube (P.M.T.). Each tube is powered and read out by its electronics board. With sixty-four strips serviced by each P.M.T., each row of twenty P.M.T.'s and boards is configured to service eight consecutive planes. Sixteen P.M.T.'s cover the 127 core scintillator strips per plane. The four additional P.M.T.'s service the 30 more O.D. scintillators per plane in the group of eight.

The electronics boards record detector activity during a synchronized 16 μs gate. The gate is timed to begin approximately 1 μs before the beam spill arrives. By extending past the end of the 10 μs spill time, the gate also captures delayed activity, including Michel decay electrons originating from stopped pions.

During the gate, when a discriminator fires, time and charge information for that discriminator's channels are pushed onto a volatile memory stack. (Charge for each channel is measured at three different gains to improve the dynamic range of the charge measurement.) If the same discriminator fires again during the gate, the channel data is pushed again onto the stack, which is able to go several levels deep before there is loss of information. This arrangement allows a limited amount of event pile-up. After the gate, the board

waits in a "full" state until it is read out and reset by the D.A.Q. crate.

The electronics boards communicate by a token-ring network with the data acquisition (D.A.Q.) system. This system is set up in a V.M.E. crate beside the detector. The D.A.Q. reads and sorts the data arriving from the electronics boards. Zero-suppression occurs at this readout time, meaning channels with charge consistent with zero are not saved. Every beam spill is then written to disk. Since MINERvA takes data at a low rate (2 Hz is the rate of the beam spill), there is no need to filter at the data acquisition stage. Filtering of the beam spills will be done at the analysis stage. The data also needs to be matched up with MINOS Near Detector data for muon reconstruction. Offline, the MINERvA stream will be matched up spill-for-spill to the MINOS stream, and the combined streams will then be fed to the analysis stage.

Chapter 3 Calibration

The calibration stages can be roughly separated into two: first, the stage that operates on each channel by itself, and second, the stage of calibrations that involve two or more channels at a time. The first stage involves exactly three scaling factors per channel: (*1*) the conversion of charge from analog-to-digital converter (A.D.C.) counts to femtocoulombs (fC); (*2*) the conversion of fC to photoelectrons (p.e.) at the P.M.T. anode; and (*3*) a dimensionless factor representing fiber attenuation between the anode and the center of the scintillator bar.

More complex calibrations than these use tracks. Because of the interlocking triangle shape of MINERvA strips (Fig. 3.2), calibrations involving tracks work on a minimum of two channels at a time. This chapter focuses on my work on the detector alignment, which is the step that begins tracking-based calibrations.

3.1 Charge, p.e., and Attenuation Factors

The A.D.C.-counts to fC conversion is measured on each electronics board before installation, as illustrated in [19, Fig. 18].

For converting fC to p.e., the pedestal level and 1p.e. level of each P.M.T. is measured continuously during detector running. This dynamic calibration allows for effects due to fluctuations in temperature, voltage, and other operating conditions. Pedestal levels are measured between beam spills when no detector

activity is expected. The level of 1p.e. is measured by "light injection," where a diode is flashed through a separate fiber-optic at all the P.M.T.'s. This also occurs between beam spills. Offline, the charge distribution of injected light is measured, and the 1p.e. peak is found by fitting the distribution. An example fit is shown in [19, Fig. 20].

Attenuation is measured in each plane before installation. The plane is scanned with a radioactive source, and a table of signal vs. fiber length is produced for each scintillator in the plane. Because of the mirror at the far end of the fiber, the expected functional form of this data is a double exponential. For some strips, the actual function can be very different than a simple double exponential, when defects such as broken fibers and "glue holes" produce discontinuities in the signal vs. length function. (A glue hole is a refractive air bubble in the glue. The glue is supposed to bind the fiber to the scintillator.) By saving all scan data, these defects will be accounted for during the attenuation factor calculation at reconstruction time.

There are two ways to apply the attenuation factor at reconstruction time. If a reconstructed track is not available, the attenuation at the center of the strip is used. This is usually a good approximation, but it does not make use of the entire attenuation vs. fiber length data that the attenuation scanning has produced. For isolated hits in the detector, this central attenuation is the best that can be done.

For hits that belong to a reconstructed track, however, the true fiber position has been measured, so a better attenuation factor is applied, using a function of attenuation vs. position, from an interpolation of the scanning data.

3.2 Pre-Calibration Compensation for Alignment Variations

Framed pairs of MINERvA planes (modules) have no rigid connection to one another. Plane placement varies even within a module, since the O.D. frame puts stresses and strains on the scintillator. Installed planes therefore end up misaligned. The detector alignment was first investigated by B. Ziemer in [25].

These misalignments are measured *in situ* by the method I document here. The triangular cross-sectional shape of MINERvA's strips will be utilized for position precision. The tip of each triangle is determined to millimeter precision, from muon tracks. Next these positional data are expressed as affine transformations acting on the planes as rigid bodies. The transformation parameters become MINERvA's "alignment constants."

The alignment constants are needed for track finding, and also for energy calibration. I will show how the alignment supports the energy calibration, and then will describe my contributions to the energy calibration.

Utilization of Triangular Strip Shape

The unique feature of the MINERvA detector is its triangular strips, installed in alternating directions to form planes (photo, Fig. 3.1). The MINERvA design means that a relative energy calibration ("strip-to-strip" calibration) must be delayed until after the alignment constants are provided. To see why this is so, consider that a strip-to-strip calibration means taking every channel's spectrum of $q/\delta S$ for minimum ionizing particles (MIPs), where q is the measured energy and δS is the distance through the scintillator. This problem is easier

Figure 3.1: *Scintillator strips,* without optical fibers, laid out on a table. Individual strips are coated with white TiO_2 paint. Photo from Fermilab Visual Media Services, Negative No. 05-0144-16D.

for rectangular-strip detectors than for MINERvA.

In detectors of rectangular strips, there is no difficulty finding tracks with known length δS. When the hit is a "single," *i.e.,* having no adjacent hits in the same plane, then the track length through that scintillator is given by $\delta S = L \sec\theta$, where L is the scintillator thickness, and θ is the track angle to the detector z-axis. It should be clear that MINERvA does not have this convenience. Tracks crossing triangular strips can take any length (Fig. 3.2). The track length will correlate very little to the angle θ.

I suggest the solution to this problem in Figs. 3.2 and 3.3. The solution is to discover a different variable, instead of θ, that predicts the track length in one scintillator. The total distance crossed in one plane remains $L \sec\theta$ but this distance is spread across two independent channels, with distance δS_1 in the first channel and δS_2 in the second channel. Neither δS_i is knowable from the track angle θ alone. Fig. 3.3 suggests how the x-position[1] should be used to calculate δS for shallow angle tracks.

[1]In this section, the x direction refers to the direction of increasing strip number. This is the detector coordinate x only when the view is X.

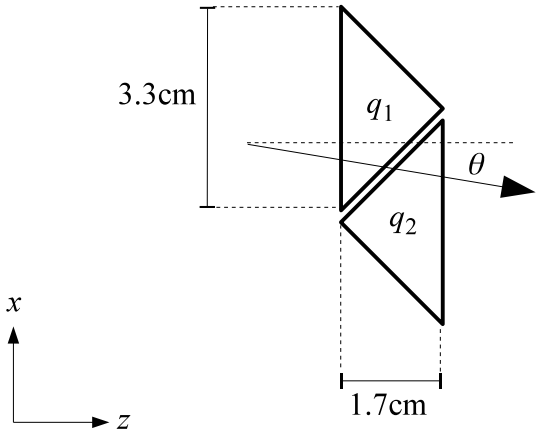

Figure 3.2: *Track in two* MINERvA *strips.* In general, the strips have different MIP levels. Without a single MIP factor for the two strips, there is no exact relation between the track length $L \sec\theta$ and the total charge q_1+q_2. ($L = 1.7$ cm is the strip height and the plane thickness.)

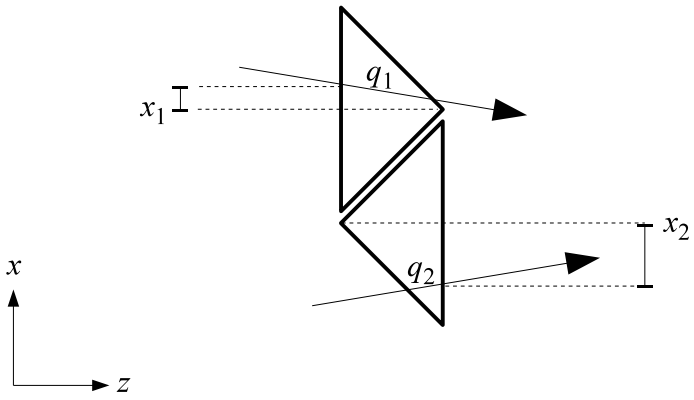

Figure 3.3: *Expected charge in one* MINERvA *strip.* For shallow angle tracks, the deposited charge q_i is approximately proportional to $L - |x_i|$ (Equation (3.A), since the triangle is close to right isosceles). The sign of x is important. This figure depicts a small positive x_1 and a large negative x_2.

Locator of Triangle Tip for Shallow Angle Tracks

I will use the x-positional data to find track lengths δS, but this assumes critically that the strip boundaries are known well. This is the argument for putting the detector alignment first, prior to the strip-to-strip calibration. In this subsection, I will find all the strip boundaries in x using muon tracks.

In the approximation that follows, all track angles θ are less than a few degrees.

We define the base variable x as the coordinate where the track enters/exits the triangle on the base side (Fig. 3.3). This x is zero on the midpoint and takes on values from $-B/2$ to $B/2$ (where $B = 3.3$ cm is the base length). The path can now be estimated as

$$\delta S \approx L - |x|. \tag{3.A}$$

For approximation (3.A), the triangle is made exactly right isosceles, and the track is made exactly normal incident (so that θ is ignored entirely). Muons entering the front of MINERvA do not have high enough θ to break this approximation significantly.

The trick now is to check, experimentally, whether the greatest charge occurs at $x = 0$. If it does, the plane is aligned. If not, an alignment parameter will be applied to line it up.

We assume that the plane is a rigid body that has translated away from its ideal position, by a distance s along its x-axis. We measure that translation as follows. From a sample of muon tracks, hits are selected where two conditions coincide: (a) there is a hit above zero-suppression in some electronics channel

in that plane, and (b) the fitted track line[2] enters and exits the ideal strip volume corresponding to that channel.

Generally, conditions (a) and (b) are almost identical. A few events satisfy only one or the other of the conditions. A hit of small value may cause a strip to lie in the geometrical track line, while zero-suppression hides the charge in the electronics channel. On the other hand a delta ray (δ-ray) may cause a neighboring strip to have charge that does not lie in the line. These occurrences are usually infrequent and can be ignored. When the mismatch is not infrequent, it indicates bugs in the mapping of physical scintillators to electronics channel numbers, from optical fibers having been plugged into the wrong electronics channels. The data obtained here can clear the bugs. This idea will be pursued further (§3.3).

To complete the measurement of s, the user now measures mean charge $\langle\, q \,\rangle$ versus base coordinate x for the plane under consideration. The result looks like Fig. 3.4. The triangular cross-sectional shape of the MINERvA strip is clearly seen. We measure the peak position by fitting the plot to a triangle-shaped function, such as

$$y(s, q_0; x) = q_0 \, |L - (x - s)| \tag{3.B}$$

(where s and q_0 are the parameters of the fit). After the fit, the peak position s is the shift that puts the plane into alignment. The rounding of the peak, visible in Fig. 3.4 data but not in the fit function, is thought to be due to the fiber hole, which runs down the middle of the strip though the height. (The

[2]Tracking can be performed before alignment as perfect track-fitting is not needed here.

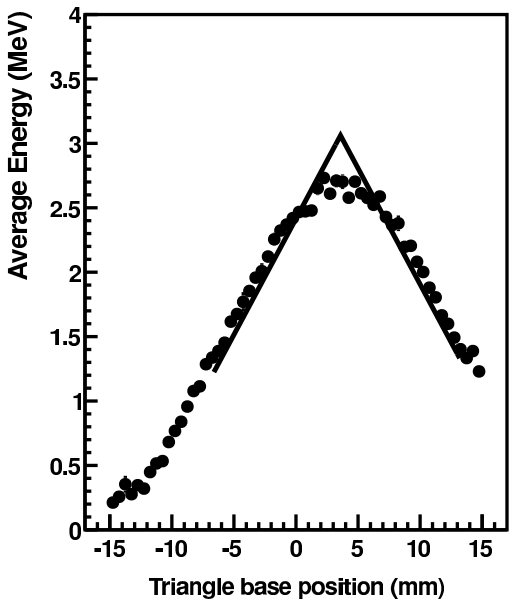

Figure 3.4: *Method to measure rigid plane shift.* Plot by C. M. Marshall and the present author. This example shows MINERvA module 61, plane 1. Fitting function (3.B) is shown. The x-axis bins are 0.5 mm wide.

other fit parameter q_0 is a scale parameter that is thrown away. The strip-to-strip calibration will provide the correct scale, per individual channel.)

Rotation About the z-Axis

The plane's affine transformation will include a rotation θ about the z-axis. The rotation is found by the same process as above, with a slight variation. Let the plane be divided into a handful of sections in the y-direction like Fig. 3.5, where two measurement sections are shown. By comparing the s returned for each section the rotation can be determined. If the plane is not rotated about z, then all sections will return the same s. But if the plane is rotated, the difference of s_{bottom} and s_{top} (for example) measures the rotation in radians

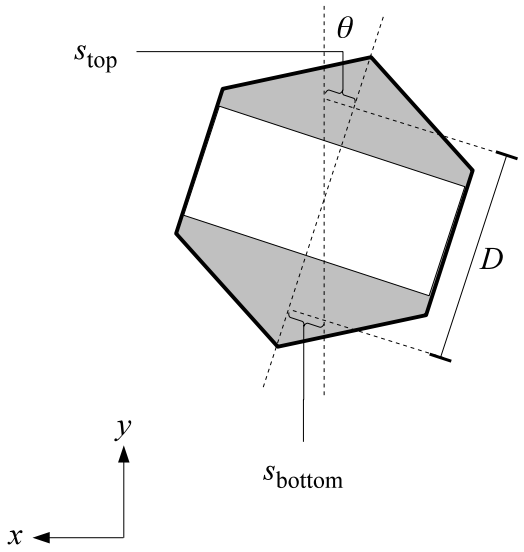

Figure 3.5: *Method to measure rigid plane rotation.* The plane with a rotation θ about the z-axis is seen. To measure θ we divide the plane into a handful of sections. Shift s_{top} (s_{bottom}) is measured with muons restricted to the top (bottom) shaded section. The distance D is between the sectional midpoints. The rotation θ about the z-axis can be calculated by equation (3.C).

by

$$\theta = \frac{s_{\text{top}} - s_{\text{bottom}}}{D} \tag{3.C}$$

where D is the distance from the midpoint of the top section to the midpoint of the bottom section. With $D \approx 2$ meters and $s \approx$ centimeters, rotations in milliradians are found. More sections can be used for greater confidence. My actual implementation uses six sections. This is illustrated fully in Figure 24 of reference [19].

Generalization to Steep Tracks

The MINERvA Test Beam detector, situated above ground and calibrated with cosmics, was found to fail the alignment procedure. The problem was high-

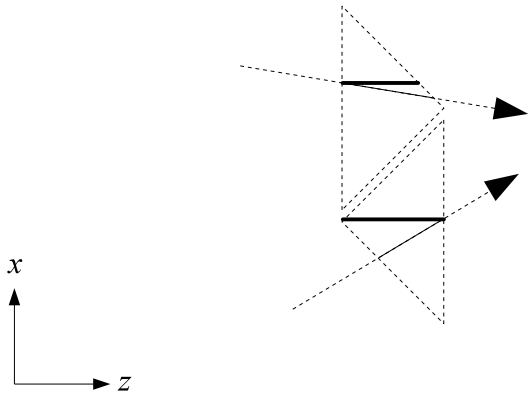

Figure 3.6: *Normal incidence correction.* The true path δS is represented by the thin solid lines, while the normal-incident path $\delta S_\perp$ is represented by the thick lines. The true path may have a component in the $\pm y$-direction (normal to the page) whereas the normal-incident path may not. Note that $\delta S_\perp = \delta S$ when $\theta = 0$. Figure adapted from [26].

angle cosmic tracks break approximation (3.A) badly.

The author of [26] rescued the procedure with a simple correction. Reference [26] defines the normal-incident path ($\delta S_\perp$) as the distance along a line, normal to the base, from the track entry/exit to an arbitrary point on the other leg (Fig. 3.6). The two paths δS and $\delta S_\perp$ will be calculated with ray tracing and not with approximation (3.A). Now, the user makes the graph of

$$\left\langle \frac{q\,\delta S_\perp}{\delta S} \right\rangle \tag{3.D}$$

versus x, in place of uncorrected $\langle\, q \,\rangle$ versus x.

Formula (3.D) is valid because it reduces to $\langle\, q \,\rangle$ when the track angle is small, so the shallow angle procedure is unmodified by this change. But for tracks of steep angle, it approximately predicts the energy loss that a shallow angle track would have at the same base (see Fig. 3.6). The alignment can proceed as before.

The plane affine transformation as far as we measure it has just shift along the transverse axis and a rotation about the z-axis. This parameter set does not attempt to describe all alignment effects. However, it is demonstrated sufficient for its main purpose, which is accomplishing the strip-to-strip calibration. The alignment does not require a second iteration. Re-running after the first iteration is found to return residual shifts and residual rotations all consistent with zero. Reference [26] states, "The resolution of the alignment is several tenths of millimeters and several tenths of milliradians; further iterations will not improve these figures."

3.3 Validation of Fiber Routing

As mentioned previously, the alignment algorithm also produces a tool for debugging the routing of fibers. During the alignment we make a database of strips that do not lie in the track or do not fire when expected. The most common error of this type is the pair swap, where two adjacent fibers cross. The pair swap looks to the detector like Fig. 3.7.

Pair swaps are detected by producing Fig. 3.8 once per channel. This plot of q vs. x shows whether the strip is misplaced one strip-width to the left or to the right. The plot can be viewed by eye for the list of suspicious strips, or scanned by an automated script for the entire detector. Normal strips will be peaked at $x = 0$ since this has already been corrected at the alignment stage. But in the case of a swapped pair, the lower strip number in the pair will be centered at $+B/2$ and the higher strip at $-B/2$. These anomalies were not detected earlier by Fig. 3.4, since the 125 correct strips dominate the sum. Since the shift is unmistakably large, it is easy to spot this pattern for every case where it occurs. Fig. 3.8 shows a normal strip compared to to a strip that was discovered pair-swapped with its adjacent neighbor after installation.

After pair swaps have been exhausted, when other suspicious strips remain, an algorithm (originated in [26]) systematically correlates the q in one strip against the δS of every other strip until matches occur. The alignment procedure may be run "for real" after routing errors are completely corrected.

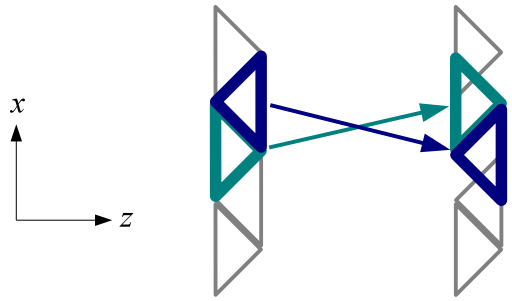

Figure 3.7: *Diagram of a pair swap.* The crossing of two optical fibers causes adjacent strips to appear in each other's place.

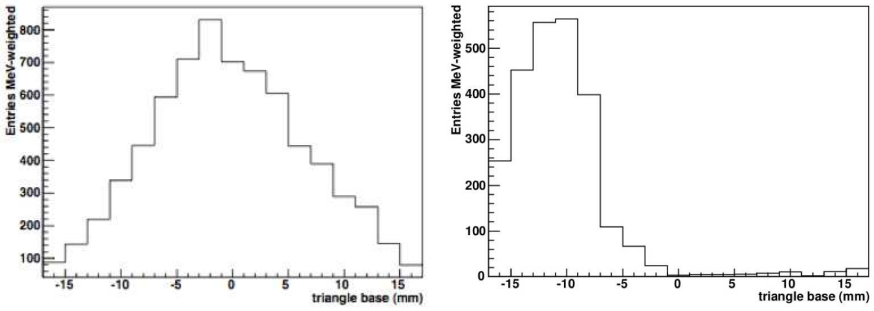

Figure 3.8: *Method to detect pair swaps.* This pair of plots is q vs. x for two individual channels (left: module 75, plane 2, strip 63; right: module 2, plane 1, strip 76). The swap in module 2 was corrected after its discovery. The horizontal axis is the base coordinate x, in bins of 2 mm; the vertical axis is the sum of q in each bin.

3.4 Relative Energy Response Calibration

This author developed MINERvA's strip-to-strip calibration initially. The final form of this calibration is described well in reference [19], so I only need to give an outline of it here.

The rate of energy loss $\langle\, dE/dx \,\rangle$ of minimum-ionizing muons is a slowly-varying function of the muon energy. NuMI muons from the upstream rock provide a constant source of these MIPs, and all strips in the detector are exposed to the same MIP spectrum. The $\langle\, q/\delta S \,\rangle$-response of each strip should be scaled by a multiplicative constant to make them uniform.

The initial problem in strip-to-strip calibration for MINERvA is measuring δS, to produce a spectrum of $q/\delta S$ that accurately reflects the MIP-level in a channel. The physical part of the problem is solved in the alignment as described in the section previous. We are now ready to measure q and δS in any strip. To accomodate MINERvA's strip shape the path δS is measured by ray tracing.[3] Ray tracing has already been mentioned in connection with the steep-tracks generalization of alignment, and will be used again here.

For each front-entering muon track, we determine a parametric equation $\vec{x}(t)$ for the track line or curve.[4] For each strip, solve this equation for the two values of t where the track intersects the strip surfaces. The strip is modeled as a triangular prism with five faces (three long sides and two caps). The intersection points will usually fall on the base side and one of the lengthwise sides; the two caps rarely play a role here only rarely, for tracks very near the

[3] We now abandon Equation (3.A), as this was just a trick to make the alignment go initially.

[4] t is an arbitrary geometric parameter, not necessarily time. The method is called "ray tracing" because t gives the curve a direction, as a ray.

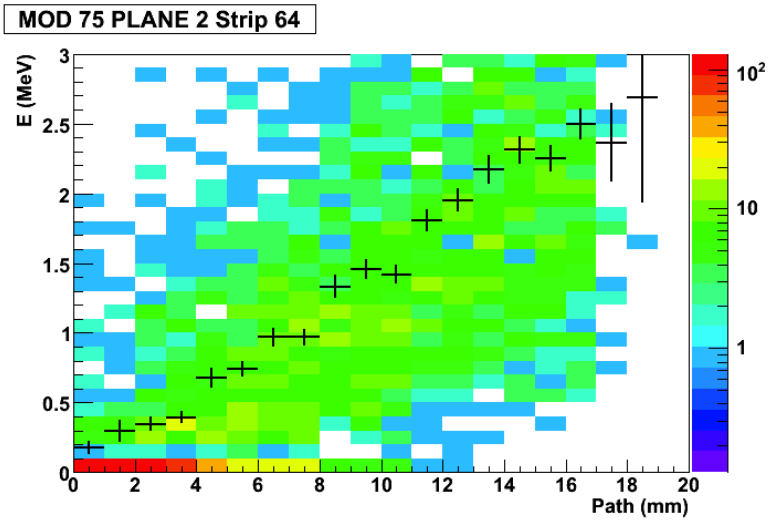

Figure 3.9: *Deposited energy versus scintillator path.* This two-dimensional graph shows the linear relationship between $\langle\, q \,\rangle$ and δS for one strip in the detector. The black points show the mean of q in each column. No truncation is applied. In order to make $\langle\, q \,\rangle \to 0$ as $\delta S \to 0$, events in the bottom row ($q = 0$) must be included when the column mean is taken.

edge. When the entry and exit parameters t_1 and t_2 are determined, then

$$\delta S = |\vec{x}(t_2) - \vec{x}(t_1)|. \tag{3.E}$$

Detector software frameworks may provide the capability to do this ray tracing as part of their detector geometry package. The strip description can be pulled from a geometry database, the same way it would be accessed by the detector simulation package. Intersection values of t can be found using library functions in the framework.

Now the $q/\delta S$ measured in this manner should be averaged over many tracks in the one channel. Long calibration intervals are defined in order to collect thousands of muons per channel. Fig. 3.9 shows $(\delta S, q)$ in MINERvA module 75, plane 2, strip 64. It is demonstrated that the average q (untrun-

cated) is proportional to δS. To get $\langle\, q \,\rangle \to 0$ at small path, and preserve the proportionality, it is critical to count events where the track clips a small corner of a strip, when no charge is recorded above suppression. These events are needed to pull down the average q at small paths. These "hits" of $q = 0$ can only be found by ray tracking.

When this data is presented as a 1D plot of $q/\delta S$ it becomes a distribution with Landau-like features (round peak, long thick tail). The reader may see [19] for details of the calculation of a truncated mean MeV/cm. This mean is now a representation of the MIP-level in that channel.

The MIP-levels for all channels will finally be expressed as dimensionless scaling constants. Using x_i as the the truncated mean $q/\delta S$ (MeV/cm) for the i^{th} channel in the detector, the calibration constant defined as

$$C_i = \frac{{x_i}^{-1}}{\langle\, x^{-1} \,\rangle} \tag{3.F}$$

(where the average in the normalization factor is taken over all the strips in the detector) is the scaling applied to that channel to get uniform MIP-level across MINERvA.

Lastly, a correction-to-the-correction for handling the peak-mean difference in different detector regions is described in [19].

3.5 Absolute Energy and Timing

The calibration of absolute energy is a small step away from the equalization of relative strip response. The absolute calibration uses muons of known momen-

tum, which have been measured in the MINOS N.D. At each plane, the true muon energy is computed, by adding the energy loss in downstream materials to the muon energy at its entry into MINOS. The measured energy loss dE/dx, computed now by $E \sec \theta_{\mathrm{Det}}$ for the total muon energy in that plane, can now be compared to the result of energy loss theory [36]. A single correction factor for the entire MINERvA detector now converts measured charges to calibrated energy in MeV.

A final aspect of the calibration chain is timing. Time data from muon tracks is found by converting the fiber length to a delay (assuming light travels through the fiber at a known speed), in the same manner as converting the fiber length to an attenuation. Using this time data, electronics boards at different locations in the detector are synchronized to one another, by using c as the speed of muons through the detector. Every hit can now be assigned a time along with its charge. For isolated hits, without a track, the true fiber position has not been measured. In this case the hit time is assigned as the discriminator time minus the delay to the center of the scintillator.

Chapter 4 Simulation

4.1 Monte Carlo Beam Simulator

The GEANT4 v9.2.p03 simulation softare [27] is used to generate the neutrino flux to the detector. The simulation begins with protons interacting with the graphite target at 120 GeV. The produced pions and kaons are transported through a simulation of the NuMI beamline, and then allowed to decay. The uncertainties are summarized in Table 4.1, along with cross-section uncertainties.

Hadroproduction in the target is adjusted to match data [28, 29]. Hadrons are produced using a certain model FTFP_BERT in GEANT4, however, the results will be adjusted in such a way that the model is not necessarily preserved. Each hadron produced is given an event weight. The value of the

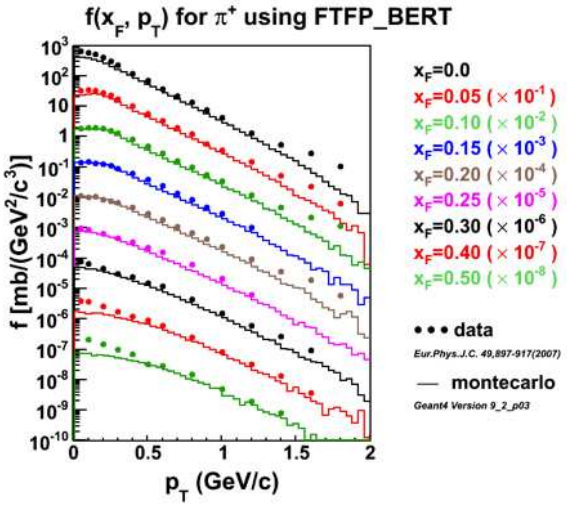

Figure 4.1: $\pi\,^{12}$C *interaction model for beam simulation.* From [30].

weight is a function of its Feynman scaling variable x_F and its transverse momentum p_T. The weight attempts to make the simulated hadroproduction agree with data. By choosing an appropriate weighting function, the weighted simulation can be always be a good model of the data, whatever the bare results of the unweighted simulation. Figure 4.1 shows the weighted simulation cross-section for π^+ production in the target, along with hadroproduction data points from [29].

The hadroproduction uncertainty model can be explained briefly. When the neutrino's mother particle is the direct product of a p^{12}C collision in the target, *and* the collision's kinematics (x_F, p_T) are within the coverage of our external hadroproduction data sets, then the model reweighted to data is used. The uncertainty is propagated from data [29]. It includes systematic uncertainties totalling 3.8%, plus statistical uncertainty depending on the (x_F, p_T)-bin, but generally under 10%.

Use of the model reweighted to data is possible on only about 70% of events. For the remaining 30%, where the neutrino may descend from a reinteracted (or "tertiary") hadron, or where the kinematics are out of the external data set's coverage, we must resort to model spread within the Monte Carlo to estimate an uncertainty. The hadroproduction model in GEANT4 is changed to: QGSP, FTFP_BERT, QGSC_BERT, QGSP_BERT and FTF_BIC. The model spread can be the dominant uncertainty for events in the high energy tail of E_ν.

Parameter	Value	Uncertainty
Flux		
P.O.T. per Spill	$\approx 35 \times 10^{12}$	$\pm 2\%$
Fraction of Protons in Baffle	0.001	$\pm 0.25\%$
Target Offset (z)	0 cm	± 4 cm
First Horn Offset (r)	0 mm	± 1 mm
Horn Current	185 kA	$\pm 1\%$
Horn Conductor Skin Depth	7.7 mm	(6 mm, ∞)
Hadron Prod. Cross-section (stat.)	$f(x_F, p_T)$	$\pm(1, 10)\%$
Hadron Prod. Cross-section (syst.)	–	$\pm 3.8\%$
Model Spread for "tertiary" events	Different Models	
(Quasi-) Elastic Model		
N.C. Elastic M_A	0.99 GeV	$\pm 25\%$
N.C. Elastic η	0.12	$\pm 30\%$
C.C.Q.E. M_A	0.99 GeV	$+25(-15)\%$
C.C.Q.E. Normalization	1.0	$+20(-15)\%$
C.C.Q.E. Vector F.F. Shape	Dipole or B.B.B.A.	
C.C.Q.E. Pauli Blocking Momentum Cutoff	k_F	$\pm 30\%$
Resonance Model		
C.C. Resonance Normalization	1.0	$\pm 20\%$
Resonance M_V^{Δ}	0.84 GeV	$\pm 10\%$
Non-Resonant Pion Production Model for the Transition Region at $W < 1.7$ GeV (Value is fraction of B.Y. cross-section)		
Non-Resonant $\nu p \to 1\pi$, $\bar{\nu} n \to 1\pi$	0.1	$\pm 50\%$
Non-Resonant $\nu n \to 1\pi$, $\bar{\nu} p \to 1\pi$	0.3	$\pm 50\%$
Non-Resonant $\nu p \to 2\pi$, $\bar{\nu} n \to 2\pi$	1.0	$\pm 50\%$
Non-Resonant $\nu n \to 2\pi$, $\bar{\nu} p \to 2\pi$	1.0	$\pm 50\%$

Values and uncertainties compiled from [24], [29], [31], [32].
Notation (a, b) means the uncertainty is produced by shifting the value from a to b.
Notation $\pm(a, b)\%$ means the uncertainty varies between $\pm a\%$ and $\pm b\%$.

Table 4.1: Systematic uncertainties affecting flux × cross-section.

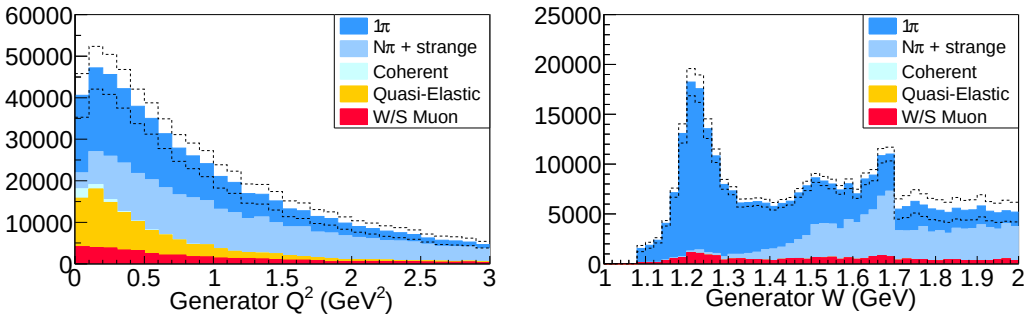

Figure 4.2: *Generated C.C. events.* This figure shows two example quantities for charged-current events generated in the fiducial volume. Wrong-sign muons, from $\bar{\nu}_\mu$ in the flux simulation, are colored in red. The dotted band shows the flux $\times$ cross-section uncertainty.

4.2 Monte Carlo Event Generator

For generation of events in the detector, GENIE v2.6.2 event generator software [31] is used, with neutrinos from the flux simulator provided as input. In GENIE v2.6.2 the available physics model for resonance production is a representation of the classic model of Rein and Sehgal [7]. The implementation sets the parameter M_A^Δ to a default of 1.12 GeV (the value suggested in [8]). To change it to another value of M_A^Δ, the implementation allows events to be reweighted. Using reweighting, I apply values of the resonant axial mass from 0.45 GeV to 1.79 GeV. Table 4.1 includes uncertainties applied to other cross-sections to generate the total flux $\times$ cross-section error.

The event generator produces neutrino events for all helicities and flavors (ν_μ, $\bar{\nu}_\mu$, ν_e, $\bar{\nu}_e$). The spectrum of generated events, for our simulated flux, is shown in Fig. 4.2. The discontinuity at $W = 1.7$ GeV arises from the transition from the resonance model to the Bodek-Yang (B.Y.) D.I.S. model. In order to include non-resonant B.Y. background at low W, while avoiding double-counting, the cross-section at $W < 1.7$ GeV is modeled as the sum

of the resonance cross-section and a fraction of the B.Y. cross-section. (The fraction used, for each target nucleon and pion multiplicity, is given in the Value column of Table 4.1.) At $W > 1.7$ GeV the transition model is dropped and the full B.Y. cross-section is used. The reader can refer to §2.1.3 of the "GENIE Physics and User Manual" [31] for a more complete description of its cross-section model and handling of the transition region.

The events are generated upon target nuclei in a subvolume of the MINERvA detector. The generation volume includes all of the tracker, but the O.D. and all modules downstream of the tracker are excluded. To get O.D. events and entering muons in the simulation, a sample of these events are recorded from data, to be interleaved with Monte Carlo-generated events. In this way, a simulation stream of mixed event types is created.

Each generated C.C. event falls in one of these categories: "Q.E." for quasi-elastic, "Coherent" for coherent pion, "1π" for single pion other than coherent, and "$N\pi$ + strange" for all others. I use these categories in plot legends frequently. Fig. 4.2 is an example. One clarification regarding the legends: Like every modern event generator, GENIE has a final-state interaction (F.S.I.) model for $A > 1$ nuclei, that allows hadrons to reinteract upon spectator nucleons. F.S.I. can change the final state particles before they are ever handed off to the detsim for propagation through the detector. By definition, F.S.I. only applies to target nucleons with $A > 1$. The MINERvA tracker contains a variety of mass numbers but principally carbon, $A = 12$ (see Table 2.1).

The demarcation between Q.E. and 1π on nuclei with $A > 1$ in the presence of F.S.I. is sometimes a matter of some confusion. By the "theorist" convention, an event is Q.E. (1π) if and only it is Q.E. (1π) *before* F.S.I. However,

when the F.S.I. model executes, any generated Q.E. event could become an "experimenter's" 1π event, by the proton reacting inelastically on a spectator. In the other direction, a theorist's 1π can become an experimenter's Q.E. by its pion getting destroyed on a spectator. In the nomenclature that seems to be emerging around this problem, the names "Q.E.-like" and "1π-like" are employed for the post-F.S.I. status, so that an event is Q.E.-like (1π-like) if and only if it has no (one) pion *after* F.S.I. I use the "theorist" convention.

While the precise effects of F.S.I. are not always important, one place where a difference is made is in interpreting the reconstruction acceptance. Events that are generated as 1π but do not reconstruct with a pion track are a mixture of two categories. The first category is true reconstruction failures, where the pion ionizes the scintillator but reconstruction returns no track for it. The second category is Q.E.-like events where the pion is destroyed before exiting the nucleus. A true reconstruction acceptance figure should be measured on the first category only.

4.3 Monte Carlo Detector Simulator

Final state particles from the event generator are handed to a GEANT4 [27]-driven detector simulator. At this point, I will begin to look at pion reinteraction in detail. Detail of a GEANT4-based presistence scheme for pion reinteractions appears in Appendix A.

For pions from 1π events generated in the fiducial volume, the simulation predicts that 13.7% of pions stop. The remainder of the pions scatter (elastically or inelastically), decay in flight, are captured in flight, or exit the

detector without stopping. The fraction of pions that stop in the fiducial is 9.5%. We can set an upper bound on reconstuction efficiency by continuing this calculation one step further. The threshold of tracking is about six planes. By requiring the pion stopped in the fiducial to have gone six planes (either forward or backward) from its piont of origination, the fraction is reduced to 3.2%. Since tracking has a 6-plane threshold, and the analysis will require the pion to stop in the fiducial, 3.2% is an absolute upper bound on the reconstruction efficiency.

In the general case, the pion may scatter. The simulation will return a "lifeline" (Appendix A) showing the place and type of each activity experienced by the pion. Let us suppose that one activity point is chosen as a reference. (For reconstructed pions, the reference will actually be chosen at reconstruction time, and it will be the activity which is spatially nearest to the end of the reconstructed track.) For each pion in the simulation, I will choose a reference from its lifeline and classify it based on its activity at the reference. I use these categories:

1. Stop, if the pion is at rest (i.e., magnitude of the 3-momentum is zero) at the reference point. It may decay or be absorbed at the rest point.

2. Decay in flight (D.I.F.), if it decays at the reference point and is not at rest.

3. Absorption in flight (A.I.F.), if it is absorbed at the reference point and is not at rest

4. Elastic Scatter (E.S.), if pion scatters elastically at the reference point.

5. Charge exchange (Q.E.X.), if it becomes π^0 through a nuclear interaction. This may occur in flight or (less frequently) at rest. (It should be noted that charge exchange from π^+ to π^- is a charge exchange process physically, but I count these events under Inelastic Scatter and not under this category.)

6. Inelastic Scatter (I.S.), if the pion scatters inelastically at the reference and the products contain exactly one π^+ or exactly one π^-.

7. Multiproduction, if the inelastic process produces other pion(s). Experimentally this appears as either a forked track, or a $\pi^0 \to \gamma\gamma$ pointing back to a kink point. Since our pions are well below hadronic showering energies, this category is rare.

Changing the reference point causes pions to migrate among these categories.

In the next chapters, I will separate Stop versus the other categories using the ionization profile at the end of the found track. With that direction in mind, let us now turn to the topic of event reconstruction.

Chapter 5

Reconstruction and Selection of Events

Event reconstruction proceeds in three stages. First, I require a muon track: this track must originate in the fiducial volume and continue into the MINOS N.D. Second, I consider the total hadronic energy in the MINERvA detector. Third, if the hadronic invariant mass $\widetilde{W}$ as measured by this method passes a D.I.S.-rejecting cut at 1.5 GeV (and some other cuts at this stage are applied, as will be explained in the below text), then I look for two more features in the event: (*1*) other tracks at the muon vertex, assumed to be hadron tracks, and (*2*) a Michel decay electron at the end of a hadron track. If these are found, and the event is consistent with 1π kinematics, then the event is selected.

5.1 Hadronic Calorimetry

We would like to begin searching for single-pion events, by separating these events from D.I.S. Our first tool is to use MINERvA entirely as a calorimeter for hadrons. This involves taking a muon track, which enters the MINOS N.D., and subtracting out the energy deposited by it—ionization by the muon, delta rays, and cross-talk. The remaining (hadronic recoil) energy is measured by calorimetry.

The calorimetry measurement is described in [19] and summarized here. In

Region	C_i
Tracker	1.222
ECAL	2.013
HCAL	10.314

$$\alpha = 1.568$$

Table 5.1: *Calorimetric constants.*

an event with a MINOS muon, hits considered part of the hatronic response fall in the time window defined by -20 ns $< t < 35$ ns, where t is from the time of the muon appearance. The hadronic recoil energy $\widetilde{E_H}$ will be measured as,

$$\widetilde{E_H} = \alpha \sum_i C_i E_i \tag{5.A}$$

where E_i is the energy in the i^{th} channel and C_i is a calorimetric constant. The constant C_i represents ionization energy deposited in passive materials surrounding that scintillator. (If the hit E_i does not belong to a reconstructed track, then no y-position information is available, so the optical attenuation at the fiber mid-point will be applied. But if the hit is a member of a reconstructed hadronic track the attentuation can be applied more accurately.) The overall scale α represents energy carried away by non-ionizing particles. Finally, a small "polyline" correction is made to the result of Eq. (5.A) to correct from the mean true E_H to the peak true E_H. This last step alters $\widetilde{E_H}$ a few percent from the result of Eq. (5.A). The polyline-corrected $\widetilde{E_H}$ is the one used.

I use the notation of a tilde, $\widetilde{\ }$, to keep this variable distinct from the other hadronic energy, $E_H = E_\pi + T_N$, that is calculated by the hypothesis

that the event is $\nu\, N \to \mu\, \pi\, N'$. The kinematic E_H can be more accurate on actual single-pion events than the calorimetric $\widetilde{E_H}$.

The constants C_i and α are given in Table 5.1. The complete set of "tilde" variables can now be calculated for events with an analyzed muon, as follows:

$$\begin{aligned} \widetilde{E_\nu} &= E_\mu + \widetilde{E_H} \\ \widetilde{Q^2} &= 2\,\widetilde{E_\nu}\left(E_\mu - p_{\mu z}\right) - m_\mu^2 \\ \widetilde{W} &= \sqrt{\max\left(0,\, m_N^2 + 2\,m_N\,\widetilde{E_H} - \widetilde{Q^2}\right)} \end{aligned} \tag{5.B}$$

The hadronic mass $\widetilde{W}$ can now be used to enhance single-pion events, as shown ahead (Fig. 5.4).

5.2 Track and Particle Recognition

The μ^-

In a charged current (C.C.) event having one or more found tracks, one track will be tagged as the muon. The track pattern recognition [19] is used first to determine an "anchor" track. This is the longest track in the event. If the anchor track agrees by time and by spatial projection with a muon track entering the MINOS near detector, then this track is labeled the muon and the reconstruction continues. (The kinematical space for MINERvA muons entering into MINOS is somewhat narrow. The muon must have momentum more than 1.5 GeV/c and angle less than 25 degrees.)

The muon's energy is determined by the sum of its MINOS energy and

the energy that was absorbed by material between the event and the front of MINOS. This material usually including some interdetector material, the entire length of the MINERvA detector's ECAL and HCAL, and (finally) tracker material. If the muon stops in MINOS, its energy is determined by range, otherwise by curvature. The momentum resolution is 5% by range or 10% by curvature [19].

The π^+ and optional p

After the muon is tagged, and if its starting point is found to be within the tracker, my reconstruction proceeds by attempting to supply the tracks representing π^+ and N', in the event hypothesis $\nu\, N \to \mu^-\, \pi^+\, N'$. Tracks themselves are not constrained to exactly touch at vertices. There is allowed to be, for example, a 2 cm gap in z (the separation of planes) between tracks that appear to connect at a vertex. When new tracks are added near a vertex, a vertex point is assigned at minimum distance of closest approach (D.O.C.A.)

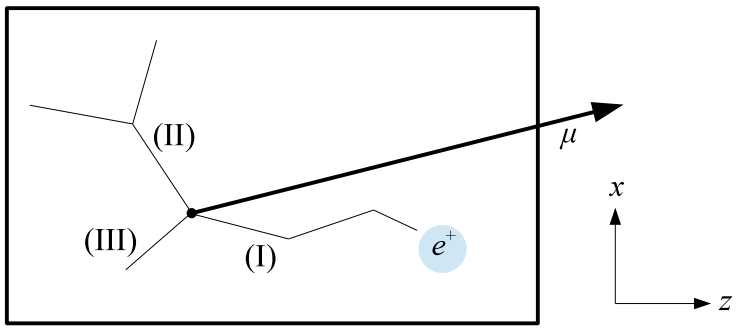

Figure 5.1: *Reconstruction Strategy.* Beginning at the muon vertex, a recursive search is made for other tracks.

from each of the connected tracks. But the vertex point is a separate piece of data from the track endpoints.

I attempt to build tracks branching out from the muon vertex. In overview, this is a search for any number of tracks, followed by a search for Michel electrons at track endpoints. The event is rejected unless one and only one Michel electron signal is found. The track representing N' (presumably a proton p) may or may not be found during this search.

In full detail, the search proceeds as follows. I use an algorithm which attempts to build tracks near any supplied vertex. Beginning with the muon vertex, the algorithm proceeds recursively at each new track's end vertex until no more tracks can be made. After the recursive track-building is finished, a search for suitable Michel electron signals is made through the track tree. This search attempts to find exactly one Michel signal among the non-forked primary tracks. A primary track satisfies the Michel electron search if and only if two conditions are satisfied: (a) it is not forked; thus, it is a line or polyline, and (b) a Michel electron signal is detected at the leaf of the polyline. Fig. 5.1 illustrates a situation with exactly one primary track satisfying the tree search. Primary track (I) leads to a leaf with no forks. The leaf initiates a Michel signal search and the signal is found. In the case of primary track (II), the search for a Michel signal never occurs because the search of the track tree terminates at a fork. Primary track (III) comes to a leaf with no Michel signal.

For typical events, all this machinery is not necessary. Forked tracks are only vanishingly probable. Tracks with more than one level of depth are about 4% of the sample (see Fig. 5.5). Thus, the search for a Michel-tagged primary

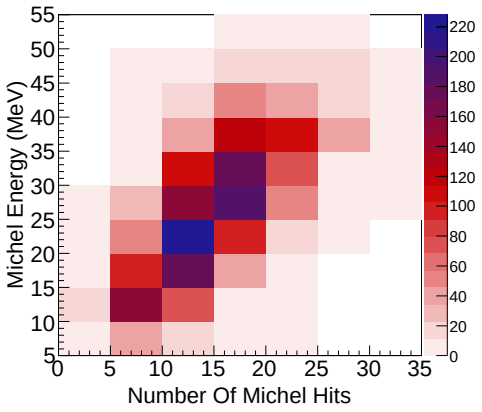

Figure 5.2: *Michel e^+ signal.* Data with cuts according to Table 5.2.

track is usually not complicated. It reduces to checking the track endpoint for the Michel electron signal.

If one Michel-tagged primary track is found, then reconstruction is successful. The pion energy is set by the range of a stopping pion. Note that this is wrong more often than not; less than half the pions actually stop. Implications of this will be discussed ahead (Chapter 6).

The Michel e^+

Obviously, the Michel electron signal is the vital part of this reconstruction. This technique appear to be a MINERvA first. Earlier scintillator experiments have not used Michel electrons for pion identification, so far as I know, although it was used to good success by MiniBooNE with Čerenkov. Reference [33] will have the description of MINERvA's Michel electron finding algorithm so I will give just an outline of it here.

Physics events in MINERvA generally are contained in a "time slice," which

is a span of a few tens of nanoseconds. Hits corresponding to a Michel electron are expected to occur long after the slice. The principle of the Michel search is that random activity at the spatial point of an earlier track end is unlikely. Hits found near that point at any later time are possible Michel activity. A space point (corresponding to the end of a found track) and an initial time are given to start the search.

Michel electrons do not meet the 5-plane threshold for line definition. For this reason, the signal will be built out of clusters (contiguous groups of scintillators with activity) but not out of tracks. A cluster has a z-coordinate and one transverse coordinate but no coordinate for the third dimension. To define the search region, a rectangular window is drawn around the search point. The search rectangle sides are 25 cm in z and 35 cm in any transverse coordinate. Clusters falling within this window must be later in time than the search time parameter, have a fired discriminator[1] and a cluster energy of at least 0.8 MeV. If any clusters in the window meet all these criteria they are counted as the Michel signal. The window size and threshold energy had been deduced from the Michel spectra of stopped, front-entering muons.

The Michel electron finder is 80.9% efficient [34] on muons that enter the front of MINERvA and stop in the tracker. Most of the inefficiency seems to be the loss of prompt Michel electrons, occurring < 1 μs after the muon or pion stops. These events may be lost during the electronics "dead time," while the electronics channels reset themselves in preparation for recording another hit during the same gate.

[1]The discriminator fire guarantees a valid time stamp. Invalid time stamps can occur when the discriminator on a *different* channel forces readout of all channels in an electronics group.

Cut	Description	See Figure
Target In Fiducial	see note (*1*)	5.3
Event Energy	$\widetilde{E_\nu} < 10$ GeV	7.5
1π Enhancement	$\widetilde{W} < 1.5$ GeV	5.4
Pion Not Kinked	$\mathsf{segments} = 1$	5.5
Length End-to-end	see note (*2*)	5.6
Length Vertex-to-end	see note (*3*)	5.6
End Contained	see note (*1*)	5.3
Sane Michel Energy	$5.0 < E < 55$ MeV and note (*4*)	5.2
Sane Michel Hit Count	$\mathsf{hits} < 35$	5.2
Proton Rejector	$\chi^2_p > 36$	6.7
Allowed Kinematics	$\sum_{\{\mu,\pi\}} (E - p_z) < m_N$	7.1
Coherent Event Rejector	$T_N > 40$ MeV	7.3
MINERvA Detector Live	$\mathsf{tdead} < 2$	5.5
2- or 3-Track	$\mathsf{tracks} < 4$	5.5
Muon Charge -1	$q/p < 0$	5.7

(*1*) $27 \leq \mathsf{module} \leq 79$ and $\rho_6 < 85$ cm. (*2*) $|\mathsf{pion\_last\_plane} - \mathsf{pion\_first\_plane}| \geq 6$. (*3*) $|\mathsf{pion\_last\_plane} - \mathsf{vertex\_plane}| \geq 6$. (*4*) If all the Michel hits are in the same view, and if the Michel hits are simultaneous with another time-separated event, then the second event deposits less than 100 MeV in MINERvA.

Table 5.2: Cuts defining [C.C./$1\pi^+$/resonant].

5.3 Cuts

At this point in our algorithm, muon and pion reconstruction have completed, and we are able to refer to their results. We define cuts to select *charged current, single charged pion, resonant* events. I abbreviate this selection using the symbol [C.C./$1\pi^+$/resonant]. The cuts are summarized in Table 5.2.

To better present the cuts, they are arranged into four cut categories.

The first cut category selects single pion events; the second category selects quality pion tracks; the third category selects events which are kinematically compatible with the hypothesis $\nu N \to \mu^- \pi^+ N'$; and the last category is a miscellaneous collection of sanity checks. The cut descriptions, below, are followed with a suite of figures, illustrating the action of each cut. In the plots that follow, the Monte Carlo is scaled to match the data (area normalized).[2]

Non-D.I.S./Single Pion from Fiducial Target

The counterintuitive part is that, after so much work has been done to obtain a pion track, we cannot *use* it until we think there are no *more* pions in the event. Many pions, π^0's most obviously, and high angle $\pi^\pm$, do not leave findable tracks. This first cut category attempts to narrow down as much as possible to single pion events on scintillator. We use calorimetric variables (Eq. (5.B)) before we are sure the found pion track is safe to look at. The pion track complexities are handled in the next cut categories rather than here.

- *Target In Fiducial.* The fiducial region in z corresponds with the tracker region of MINERvA, with a few centimeters of veto space on all sides. The coordinate in z is measured by module number, and extends from module 27 to 79. The contained pion, usually forward-going, prevents the vertex from approaching too close to the downstream boundary in z, at the 79^{th} module (Fig. 5.3(a)). The radial coordinate ρ_6, plotted

[2] I use a simple convention for plots which illustrate the action of cuts. If the x-axis variable is a cut variable, and the axis range extends beyond the cut value, then a marker is drawn at the cut, and that cut is turned off for the outside of the marker. Area normalization is applied to the inside of the marker. Besides this exception, every histogram has cuts as in Table 5.2 exactly.

I use the rule that the same plot should not appear in two chapters. My placement of figures corresponds best as possible with the associated chapter text.

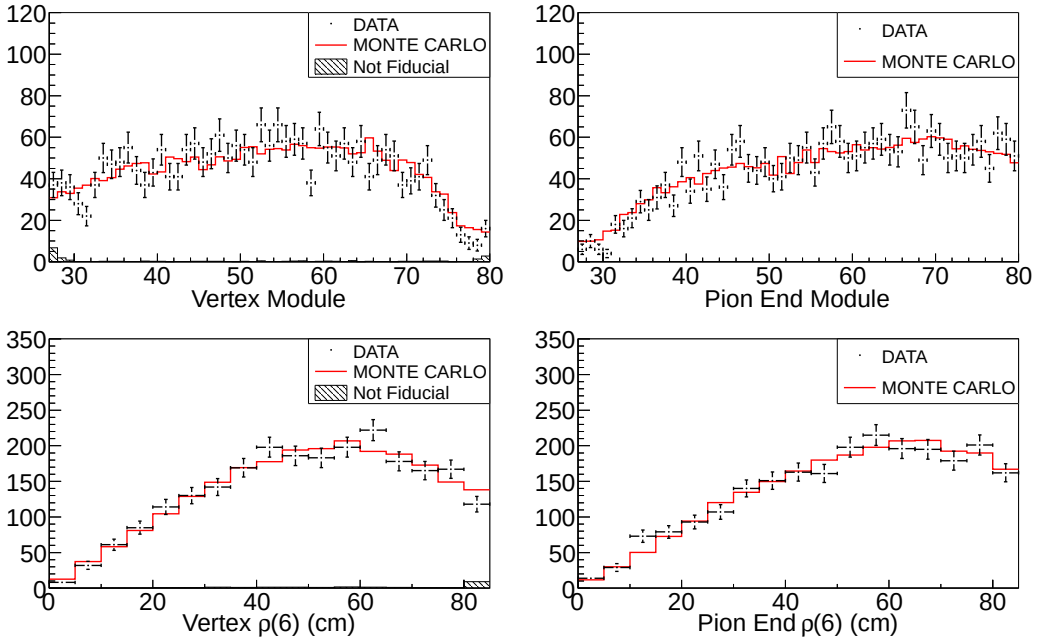

Figure 5.3: *Event Vertex and Pion End Point.* The left column shows the point of neutrino interaction; the right column shows where the pion stops.

in Fig. 5.3 bottom row, is defined to be the apothem of the smallest hexagon enclosing the point (x, y) in the plane normal to detector-z. An explicit formula for ρ_6 is,

$$\rho_6(x,y) = \begin{cases} |x| & (x^2 \geq 3y^2) \\ \frac{1}{2}|x| + \frac{\sqrt{3}}{2}|y| & (x^2 < 3y^2). \end{cases}$$

The radial boundary of the allowed region can now be stated as $\rho_6 < 85$ cm.

- *Event Energy.* The Monte Carlo model of flux times cross-section cannot be reliable in the far tail of the flux. I do not consider events beyond 10 GeV. Since the flux nearly cuts off at 5 GeV (Fig. 2.2), this cut is a gentle one.

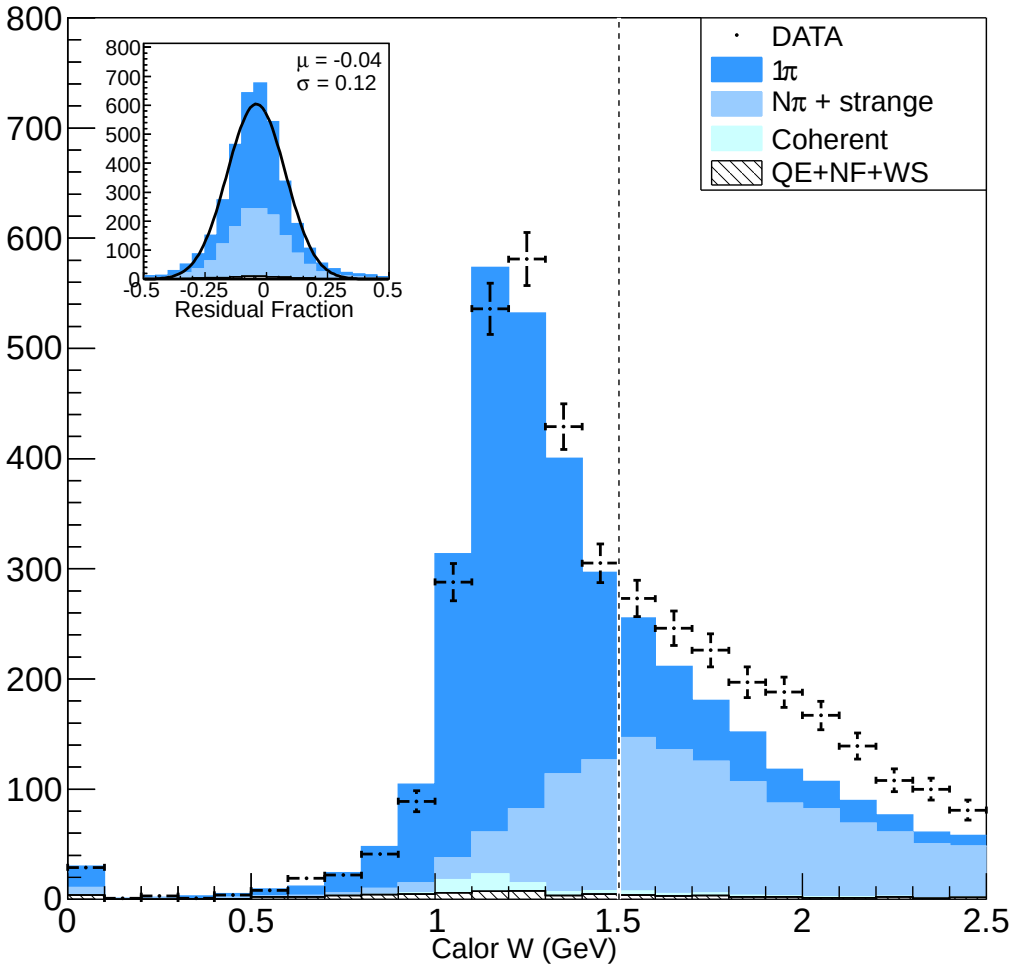

Figure 5.4: *Hadronic mass* $\widetilde{W}$. From Equation (5.B).

- *1π Enhancement.* The hadronic mass $\widetilde{W}$ cut at 1.5 GeVis meant to eliminate multi-pion events, from D.I.S. and higher-order resonances, and to focus on single pion events. This cut is illustrated in Fig. 5.4.

Quality of Pion Track

The second cut category selects pions which are likely to reconstruct correctly. Most significantly, I require pion containment. The pion has to stop in the tracker volume, where I can take a finely-sampled ionization profile that will be used to test for stopping (Chapter 6).

Besides containment, I require a number of sanity cuts on the pion, each explained below. The most significant of the sanity cuts is the proton rejector. This cut removes about 15% of data events—false positives of the Michel electron finder—while the other sanity cuts are more gentle.

- *Pion Not Kinked.* The pion track must be a single segment. This cut is consistent with my technique of using pions that range out and stop. Throwing away this cut would increase the sample by 4% only. The use of kinked tracks is an area of future study.

- *Length End-to-end/Vertex-to-end.* This pair of cuts concerns the number of planes spanned by the found pion track. The 6 plane end-to-end threshold, although nearly satisfied automatically because the MINERvA design does not allow tracks shorter than 5 planes (page 26), is imposed because I want to take 6 samples of the endpoint ionization. The duplicate requirement (end-to-end/D.O.C.A.-to-end) eleminates some misreconstructions. See Fig. 5.6 for illustration of this difference.

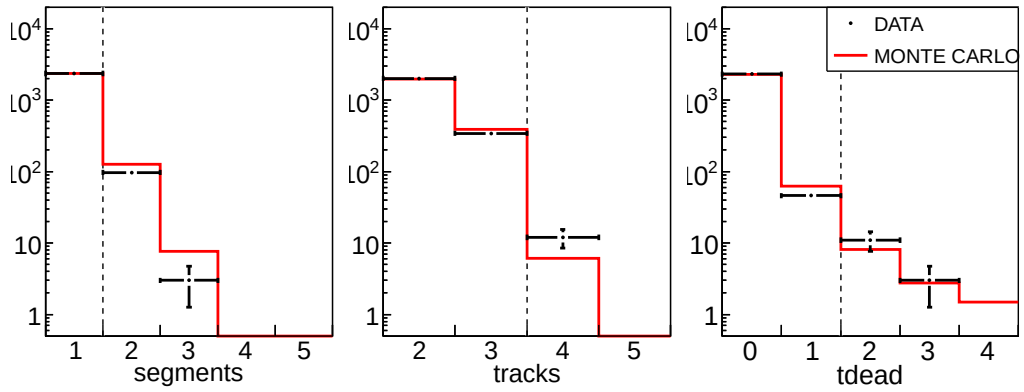

Figure 5.5: *Integer variables.* Segments in the pion track, tracks in the event, and count of dead discriminator groups.

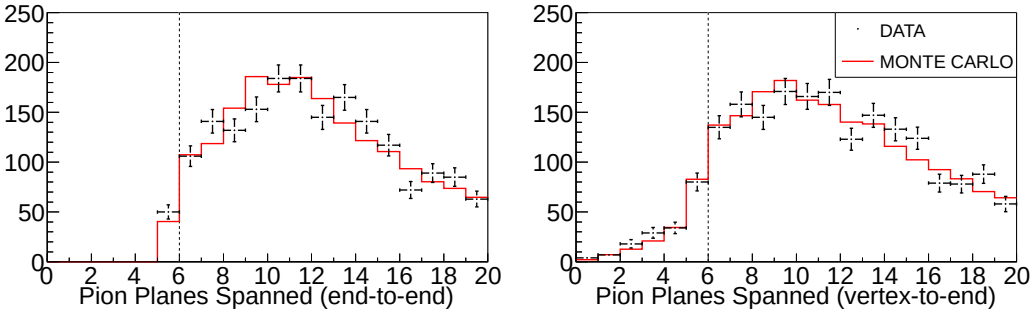

Figure 5.6: *Planes spanned by the pion.* The plot on the right uses D.O.C.A. as the track starting point. Both figures have > 400 events in the overflow bin.

- *Pion End Contained.* The pion energy is assigned according to its range, as measured vertex-to-end. The range requirement alone means that the pion must stop in MINERvA. But because I also wish to sample the endpoint ionization, the stop volume has to be reduced to the tracker, with no dense material between scintillator planes. These requirements are satisfied when my containment volume is the same as my fiducial.

- *Sane Michel Energy/Hit Count.* The originator of the Michel finder [33] suggests a combination of cuts to be used with it. The Michel

electron energy is not to exceed 55 MeV, and the (integer) number of hits comprising it is not exceed 35. Electrons appearing all in a single plane are more difficult; see the text accompanying Table 5.2 for an extra rule regarding this case. Each of these cuts has been tuned by the decays of muons that enter the front of MINERvA and stop. I also add $E > 5$ MeV because of a data excess there, as shown in Fig. 5.9.

- *Proton Rejector.* The Michel finder is not perfectly pure. My proton identifier, introduced ahead in Chapter 6, cleans up proton tracks that have a coincidental Michel electron tag (see Fig. 6.7). This cut removes 15% of the data after all other cuts are applied.

Resonant Kinematics

The cuts in this group refer to the applicability of the $\nu N \to \mu^- \pi^+ N'$ hypothesis.

- *Allowed Kinematics.* It is necessary to check the kinematic space for $\nu N \to \mu^- \pi^+ N'$. One statement of the allowed kinematics is that the sum of $E - p_z$ for the muon and the pion cannot exceed the nucleon mass m_N (see §7.1 for proof). After other cuts are applied, this cut does not remove any data events. We take comfort that the cuts in categories 1 and 2 return events with the expected kinematics already. See Fig. 7.1.

- *Coherent Rejector.* The cross-section for coherent pion production is not well-known. According to Monte Carlo, when coherent events are reconstructed in the (incorrect for coherent) hypothesis of $\nu N \to \mu^- \pi^+ N'$,

they behave as if N' is nearly at rest. I avoid this by requiring my recoiling nucleon to have at least 40 MeV of kinetic energy (Fig. 7.2).

Miscellaneous

- *Minerva Detector Live.* This cut eliminates an error caused by dead discriminators. The integer variable tdead (Fig. 5.5) counts the number of dead discriminator groups upstream of the event tracks. In events with high tdead, a muon from outside the detector may appear to originate in the tracker, because its upstream half is not recorded. No data events were found to fail the standard tdead cut (tdead < 2) after the other cuts were satisfied.

- *2- or 3-Track.* The variable tracks counts the number of found tracks, including the muon. Our events are expected to have up to three tracks although they may have only two when N' is low energy, or is a neutron. As Fig. 5.5 shows, about 0.5% of events have more than the expected number of tracks. These are cut, since they cannot satisfy the hypothesis $\nu\, N \to \mu^-\, \pi^+\, N'$.

- *Muon Charge* -1. Parents of $\bar{\nu}_\mu$ (negative pions and kaons) are not focused by the magnetic field of the horns. Fig. 4.2 shows the Monte Carlo prediction of flux $\times$ cross-section for $\bar{\nu}_\mu$ C.C. events. Most of these are in the high tail of E_ν due to unfocusing. The muon charge-to-momentum ratio, q/p, as measured in the magnetized MINOS N.D., is a useful cut independent of energy to ensure negative muons (Fig. 5.7). Muons reconstructing with positive curvature are 7% of the data after the other

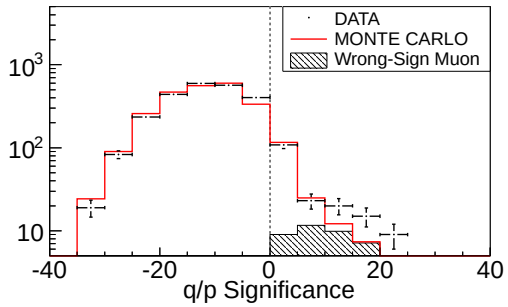

Figure 5.7: *Muon q/p Significance.* This spectrum shows the direction of muon curvature, positive or negative, as measure by the MINOS magnetic field.

cuts are satisfied (Fig. 5.7). Monte Carlo predicts that the for the majority of these positives, their curvature is close to undetermined and they are true μ^-. In any case, I require $q/p < 0$ as a sanity cut.[3]

The resulting spectra of muon, pion, and Michel particles are shown in Figures 5.8–5.9, following.

(In the following plots, I do not display the Q.E. category separately. The selection efficiency on Q.E. is very low, due to the Michel electron tag, so I lump this together with not-fiducial (N.F.) and wrong-sign muon (W.S.) into a catchall category. I show the categories 1π, $N\pi$ + strange, and Coherent, as defined in §4.2.)

[3]For plotting, the dimensionless ratio $\frac{q/p}{\sigma_{q/p}}$ is used as the x-axis variable, so that larger magnitude corresponds to greater certainty about the direction of curvature.

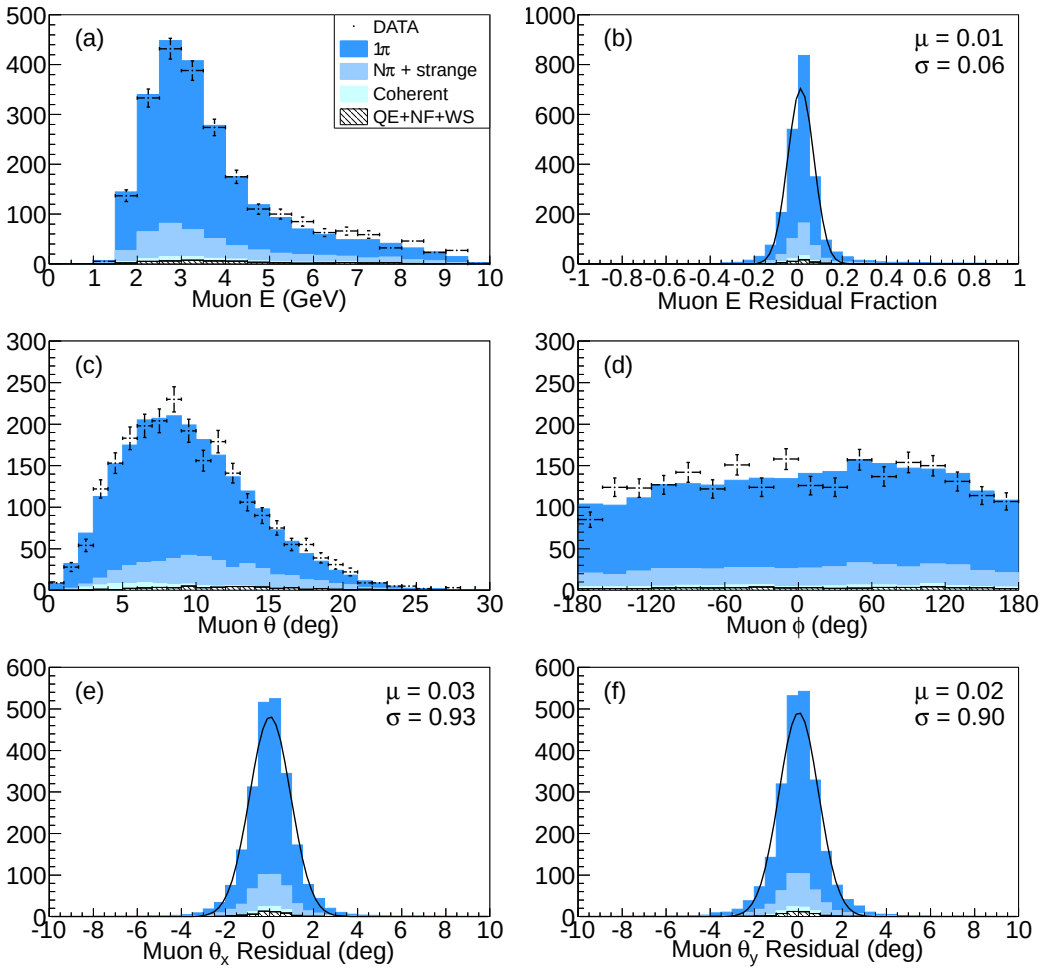

Figure 5.8: *Muon energy and angle.*

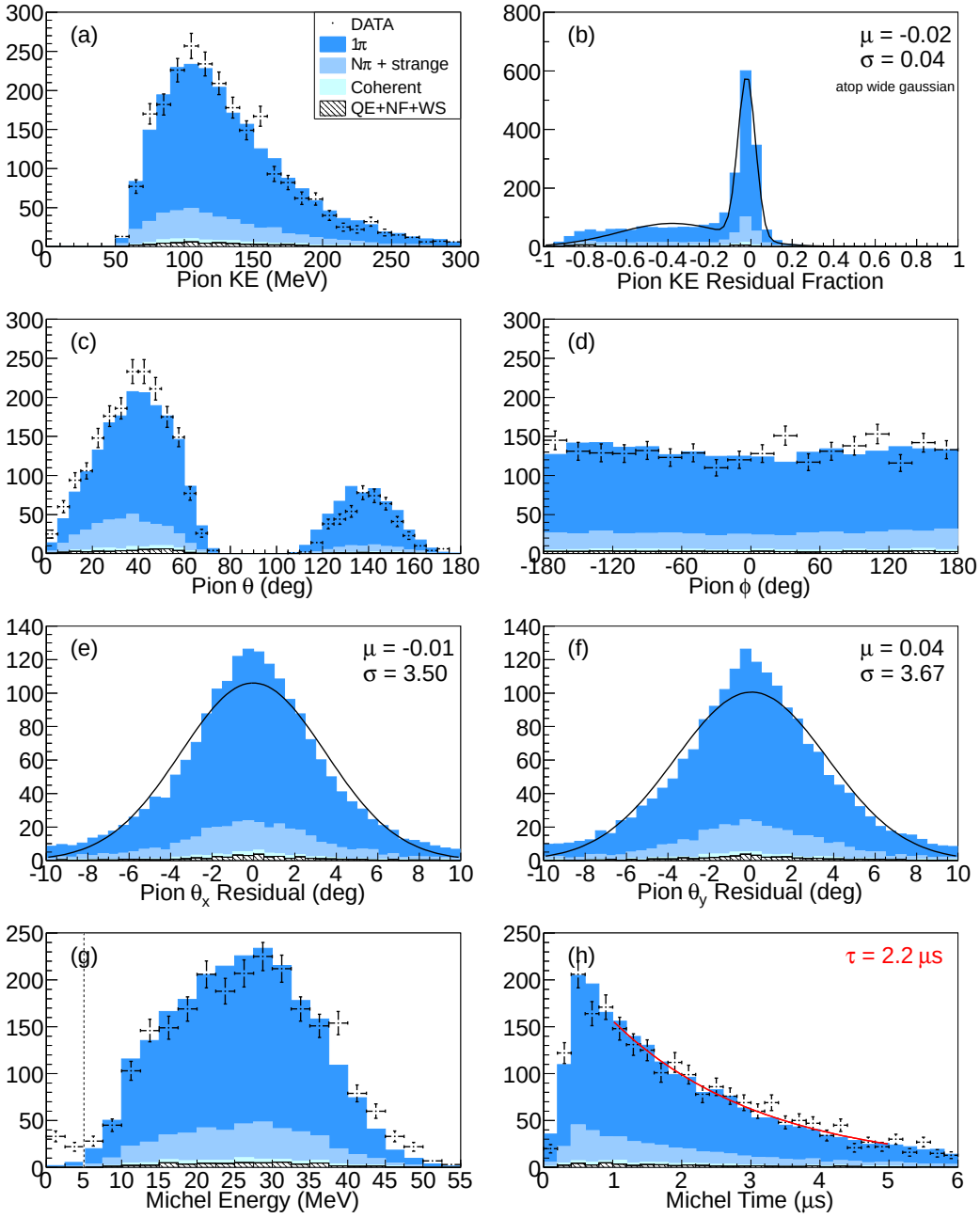

Figure 5.9: *Pion energy and angle, Michel electron energy and time.* The Michel decay constant (equal to the muon lifetime) comes from a simple exponential fit to the data in the range 1 μs to 5 μs.

Resolution		
	Muon	Pion
Energy (*1*)	6%	4% (*2*)
Direction x	0.93°	3.5°
Direction y	0.90°	3.7°

(*1*) Total for muon, Kinetic for pion. (*2*) Narrow component of double Gaussian fit.

Table 5.3: Energy and direction resolution.

5.4 Resolution of Reconstructed Particle Momenta

Fractional residuals for any quantity x are defined as $x_{\mathrm{Rec}}/x_{\mathrm{True}} - 1$. These fractionals have been shown for $x = E_\mu$, T_π and $\widetilde{W}$. For particle direction, I use the absolute residual in degrees.[4] The resolution is found by fitting the residual spectrum to a Gaussian. Table 5.3 summarizes the resolutions I have obtained for the two particles.

Finally, the bimodal residual (Fig. 5.9, second panel) alerts us to the presence of pion reinteractions. As a first step to understanding what is going on, we can look at the detector simulation results.

In Fig. 5.10, I have broken down the true 1π portion of the Monte Carlo into the pion activity categories defined in §4.3. The majority of reactions

[4]Two equivalent sets of coordinates were used in presenting the particle direction and direction residual. The polar coordinates (θ, ϕ) are defined with respect to the beam (not detector) z-axis. The projection angles θ_x and θ_y are defined according to

$$\tan\theta_x = v_x/v_z$$
$$\tan\theta_y = v_y/v_z$$

where $\vec{v} = (v_x, v_y, v_z)$ is the direction vector in the beam coordinate system. While I prefer the familiar polar coordinates (θ, ϕ) for direction, the projection angle pair is used for directional residuals, in order to get two-sided residuals.

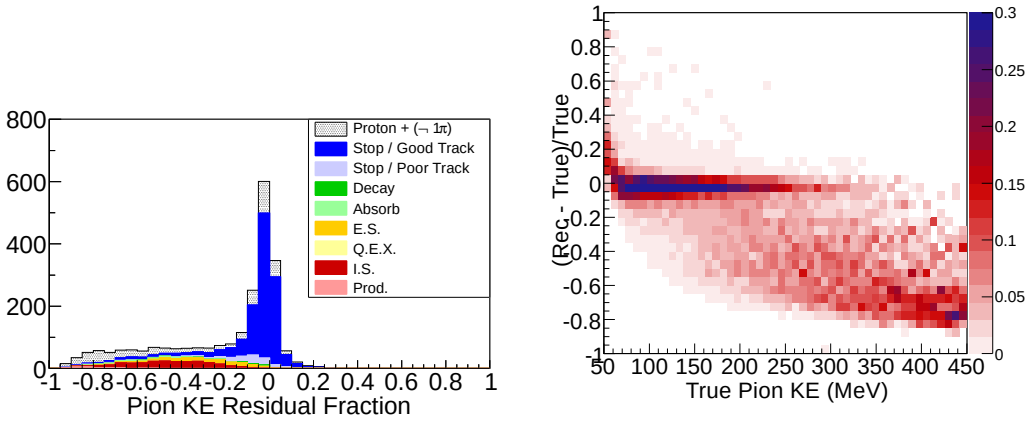

Figure 5.10: *Simulated reinteraction of pions.* Compare Fig. 1.7.

are elastic and inelastic rescattering, E.S. and I.S. Even for the categories of reaction that occur less frequently—A.I.F., Q.E.X., Absorption—the reaction causes the pion kinetic energy to be significantly underestimated. Essentially, the kinetic energy is only correct for Stop.

5.5 Acceptance, Efficiency

While I do not need to perform an efficiency correction on my data, nevertheless we must have some idea what the efficiency is. I estimate the acceptance × efficiency by taking the ratio of surviving Monte Carlo events to the number of events generated. The denominator in the ratio is the number of 1π events generated in the fiducial (equal to the dark blue area in Fig. 4.2). The numerator in the ratio is the number of these events surviving reconstruction and surviving cuts. Fig. 5.11 shows that this ratio is close to 2%. If we make it a function of the generated kinematics, it ranges between 1–2% in the most interesting kinematic regions (low Q^2, W near resonance)

and falls off gradually to zero outside these regions. There are no sharp turn-ons or turn-offs. Error bars on the figure represent the flux $\times$ cross-section uncertainty.

The shapes of Fig. 5.11 deserve some explanation. First, the turn-around in the first bin of Q^2 seems unexpected for an efficiency shape. The coherent rejector cut ($T_N > 40$ MeV) operates on events where only very small momentum is transfered to the nucleon, and is the cause of this mischief. As the dotted line in the figure proves, the turn-around would disappear if just this cut were turned off. This is mentioned in particular for readers who are interested in the low Q^2 suppression problem. Directly, my data and M.C. should not be compared to the usual graphs showing suppression at low Q^2 (e.g., Fig. 1.4), since mine are being convoluted in that region by a changing efficiency.

In order to proceed, we would like to have good reconstruction of the pion energy. For this reason we turn to the subject of stopped pion identification.

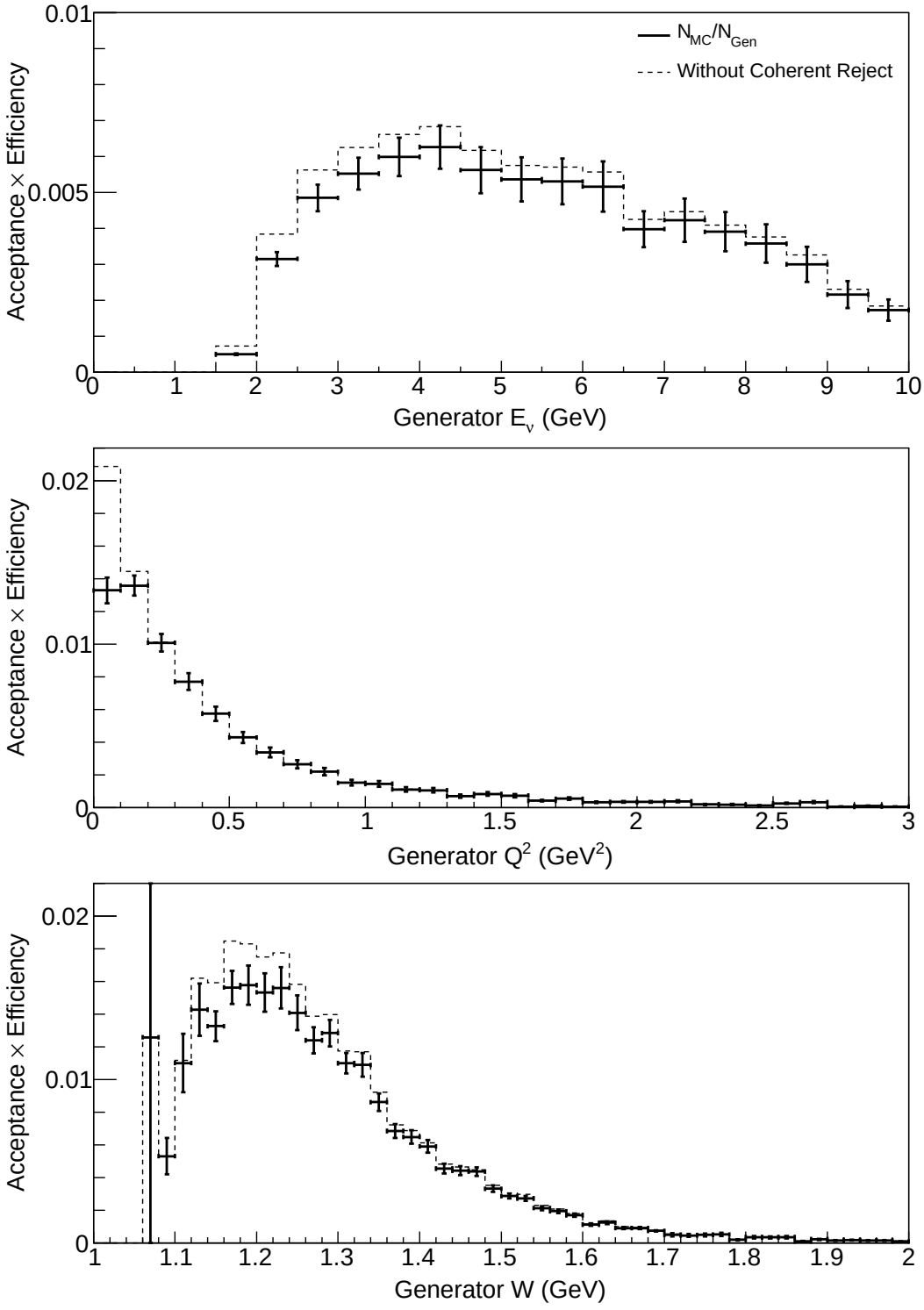

Figure 5.11: Acceptance times efficiency.

Chapter 6

Stopped Pion Identification

6.1 Overview of Signal/Background Separation

This chapter will describe the separation of the stopped pion events from other events. Hadron tracks of any other type besides stopped pions (including protons, and pions that rescatter instead of stop where the track appears to stop) are collectively called background.[1]

General considerations

Separation of a signal from a background is a general topic. The technique can be described without any reference to the hadronic physics that defines signal and background in this particular case. In general, what is desired is a function mapping events to real numbers. If a suitable function can be discovered, then the range of signal will be a disjoint interval from the range of background under that function. Then a cut will be placed at a value between the ranges. The signal will survive the cut, while the background will not.

The picture becomes more complicated if it events can be ambiguous. If there exist possible events which could be either signal or background, then

[1] It may be necessary to distinguish *reconstruction background* from *physics background.* The events to be rejected here as reconstruction background generally are events of the physics signal ($\nu N \to \mu^- \pi^+ N'$), where the reconstruction has found a false-positive Michel decay signal on a pion track ending in an inelastic scatter.

it is not possible to make the range of signal 100% disjoint from the range of background, no matter how cleverly one constructs a separation function. In a mild case, the tail of the signal distribution will overlap with the tail of the background distribution. The cut can then still be placed between the bulks of each distribution, with only small losses of efficiency and purity.

However, it is possible to continue even when there is no guarantee that the ambiguity will be "mild." (This is already to be expected by looking at the results of pion I.D. in previous scintillator-bar experiments, with SciBooNE serving as a typical example (Fig. 1.6). In SciBooNE's distribution of MIP confidence level, it is difficult to point to any obvious structure, such as a peak, which could correspond to pions which have stopped in the detector. This simple example illustrates the subtitles involved in selecting stopped pions in non-magnetized scintillator detectors.) In order to go further, the necessary thing is knowledge of and confidence about what *shape* the separation function attains on the signal part of the sample of data. This will be explained below.

It will be noted that already in the mild case we have had to make assumptions about the shapes of signal and background, e.g., that the signal must have a bulk and a tail. The background also must have a bulk and a tail, and the bulk part of it must at least be "somewhere else," far enough away so as to not interfere too much with the signal. To get away from the restriction of mild ambiguity, we just dispense entirely with assumptions about the background. The signal will have *this shape,* we say in effect, while the background will do whatever it wants.

The signal shape and the distribution of data together determine the background. For a (very contrived) illustration of how this works, suppose that a

Monte Carlo analysis of the physics of signal determines that the signal shape has two humps. If the data then has three humps, then it has been learned that the shape of the background is one hump. Or if the data has only one hump, then, provided our analysis about the signal shape has been correct, and the background level stays positive, it's been determined that the distribution of background has a valley where one of the peaks of signal was expected to be.

Benefits of the χ^2 shape

The capstone of this method, on which it all depends, is being as accurate as possible about the signal shape *before* looking at ambiguous data. My choice is to make the separation function a χ^2 because of the known shape properties of that type of function. The χ^2 distribution is typically used for its statistical properties. I am not interested (primarily) in the statistical interpretation here, but I will take advantage of the mathematical fact that the χ^2 distribution has a well-studied analytic shape. That shape is especially easy when the degrees of freedom (D.O.F.) is an even number. In the case of even D.O.F., the χ^2 distribution is a polynomial $\times$ exponential. The degree of the polynomial is $(\text{D.O.F.} - 2)/2$. The polynomial $\times$ exponential shape is easy to work with. The exact signal function used here will be given in Eq. (6.B).

General S/B separation by sideband

After the data is available, the signal scale and the background distribution will be determined. The last step of this S/B separation technique is to create a function that inputs data distributions, and outputs signal distributions. Since

we are allowing the possibility of ambiguous events, it we cannot tag individual events as either signal or background. (Events with very large χ^2, however, are unambiguously background. Later, this fact will help us determine the signal scale, by assuming continuity of the background at the point of transition between the tail of the signal and the all-background region.) However, it is always possible to estimate the number of signal and background events in any bin that is not too empty.

To create distributions of signal from distributions of data, my analysis will use a background sideband. I begin with the number of events at χ^2's large enough to be entirely background. Then I add to these an estimate of the number of background events at moderate and small χ^2, according to the background distribution as determined by all the data. The remaining number of events is signal (i.e., data minus background). This method is not unique, however, and an alternative will be considered in Chapter 8.

6.2 Definition of Energy Loss χ^2

A stopping particle can be told by its ionization profile near stopping. The shape of its energy loss is well-determined by the Bethe theory [36]. If the track ends at a point of scattering or destruction, its ionization shape is unlikely to look exactly the same as stopping.

By itself, the well-known Bethe equation predicts the rate $\left\langle \frac{dE}{dx} \right\rangle (E; m)$ of ionization, as a function of the particle energy E and mass m.[2] (The mass

[2]We assume throughout this chapter that the material charge density Z/A, mass density ρ, and mean excitation do not vary. We also assume that any particle considered has charge $z = \pm 1$.

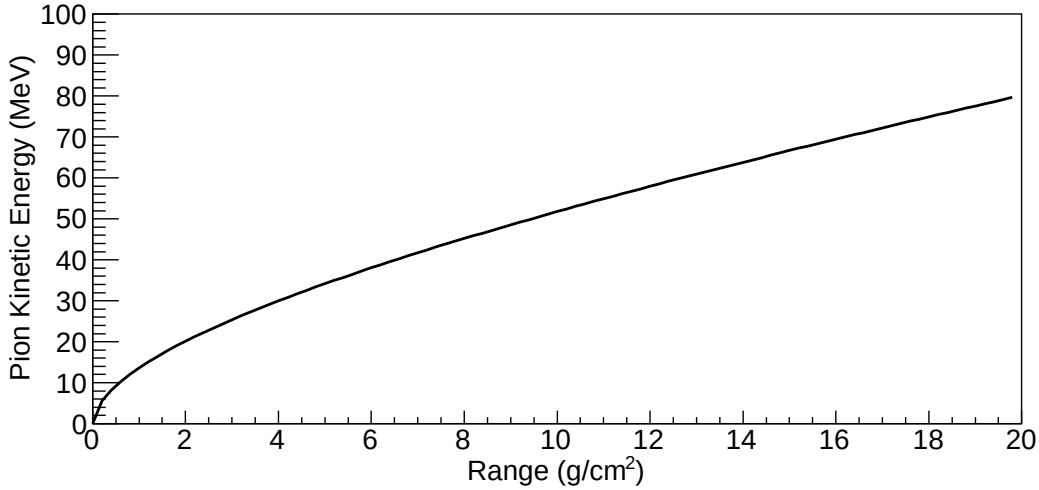

Figure 6.1: *T vs. x for pions near stopping.* The graphed function is a linear interpolating function, based upon the tabuled C.S.D.A. ranges for protons in polystyrene from Ref. [37]. The proton mass is changed to the pion mass by scaling.

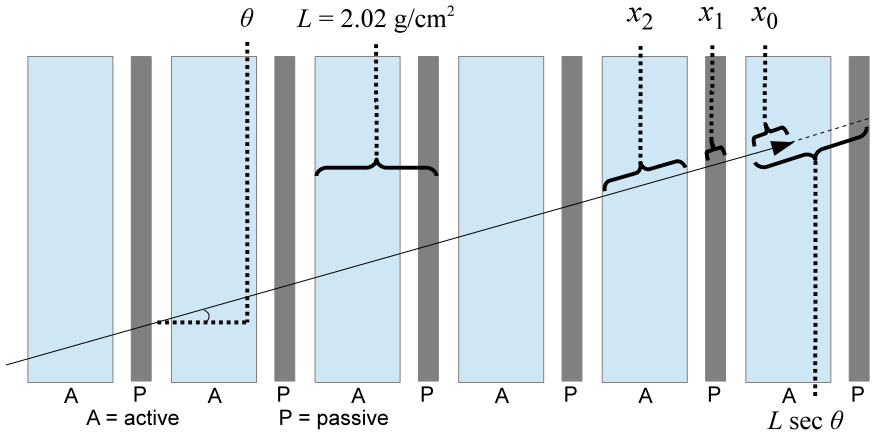

Figure 6.2: *Energy loss Monte Carlo.* The particle of mass m is started as position x_0, chosen uniformly between 0.05 g/cm^2 and $L \sec\theta$ penetration into the last plane. The particle is then propagated backward in steps of x_0, x_1 or x_2 until 6 planes are crossed. At each step an energy-loss fluctuation is chosen. From a large sample of simulations at a fixed θ, we take the mean hit $\epsilon_i(\theta; m)$ in each plane i, and their covariance matrix $V_{ij}(\theta; m)$.

can be $m = m_\pi$ or $m = m_\pi$ for the particles under present consideration). By integrating the Bethe equation, we can obtain the expected decrease in kinetic energy, as the particle travels any space interval in the material. This is sometimes known as continuous slowing-down approximation (C.S.D.A.).

C.S.D.A.'s have been tabulated for a variety of materials, and many of them can be found in Ref. [37]. For all of the work that follows, I have used a table of C.S.D.A. for protons in polystyrene. The tracker is approximated as 100% polystyrene, although this neglects the small amount of fiber, light-sealing bag and other materials in its makeup. To use the table for pions, I scale x by a factor of m_π/m_p. Positions between table entries are interpolated linearly. This same function is the function that has been used for calculating T_π during pion reconstruction (Fig. 5.9(a)). The near stopping region of the C.S.D.A. is graphed in Fig. 6.1.

The MINERvA experiment has used χ^2-based comparisons of tracks to the profiles of stopping particles [19, §10.2]. Prior to MINERvA, it appears this had never been done experimentally in scintillator-bar neutrino detectors. (The SciBar detector analyses, for example, did not attempt it. The choice, rather, was to score each pion hit as MIP-like or not, with no difference between the beginning, middle or end of the track. This has been described previously in my discussion of the SciBooNE pion analysis.) The function I construct here, is essentially a gutted-down version of the one described in Ref. [19].

The signature of a stopping particle is strongest at the end of a track. The final 6 plane energies will be labeled $E_1 \ldots E_6$. I define

$$\chi^2(E_1 \ldots E_6; \theta; m) = \sum_{i=1}^{6} \left(\frac{E_i - \bar{E}_i}{\sigma_i} \right)^2 \tag{6.A}$$

where $\bar{E}_1 \ldots \bar{E}_6$ are the expected energies, $\sigma_1 \ldots \sigma_6$ are the standard widths, θ is the track angle, and m is the particle mass. The entities on the right-hand side ($\bar{E}_i$, σ_i) are functions to be determined depending just on the material properties, θ, and m. Finally, χ^2 will be called χ^2_p when $m = m_p$ and χ^2_π when $m = m_\pi$. Six planes are sufficient to capture the rise in energy of a stopping pion in MINERvA.

In the section following, we will define $\bar{E}_i$ and σ_i so that the distribution of $\chi^2_{\pi,p}$ on stopped pion (proton) data is described by $f(\chi^2)$ with D.O.F. = 6. To be explicit, the function $f(\chi^2)$ for D.O.F. = 6 its integral are:

$$\begin{aligned} f(\chi^2) &= \frac{\chi^4}{16}\, e^{-\chi^2/2} \\ P(\chi^2) &= \int_{\chi^2}^{\infty} f(t)\, dt = \left(1 + \frac{\chi^2}{2} + \frac{\chi^4}{8}\right) e^{-\chi^2/2} \end{aligned} \tag{6.B}$$

6.3 Dependence of the 6$^{\text{th}}$ and 5$^{\text{th}}$ Planes

Let us begin by determining the expected energy $\bar{E}_6$ in the last plane. After this, we will similarly determine $\bar{E}_5$ for the second-to-last plane, and a pattern will be established to continue down to the first plane ($\bar{E}_4 \ldots \bar{E}_1$).

The energy E_6 deposited in plane 6 should increase with the track angle θ, and with the penetration depth x_0 (see Fig. 6.2). Since each tracker plane has 1.65 g/cm^2 active thickness (page 25), as x_0 increases, the deposited energy reaches a maximum when $x_0 \cos\theta = 1.65$ g/cm^2. As x_0 increases further, the pion stops in passive material and E_6 no longer increases. The maximum physical value of $x_0 \cos\theta$ is 2.02 g/cm^2, the full thickness of a tracker plane (active + passive).

For a reconstructed pion track, the track angle θ is known, but the penetration x_0 is unknown. Thus the best value for the expected energy $\bar{E}_6$ in plane 6 is determined by a Monte Carlo experiment which assumes that x_0 has a uniform distribution between 0 and $(2.02\ \mathrm{g/cm^2})\sec\theta$.

For plane 5, we see that E_5 increases with increasing θ but decreases with increasing x_0. As the depth of penetration increases, the steepest part of the energy loss shifts out of the 5^{th} plane and into the 6^{th}, thus E_5 decreases. In this case, unlike in the estimation of E_6, we have a clue from the data what the penetration is. The value of E_6 measures the penetration (to the resolution allowed by photo-statistical fluctuations).

Thus, the expectation $\bar{E}_5$ for plane 5 should contain a term $S_{56}E_6$, where S_{56} is a constant. The constant S_{56} with a negative value expresses the expected anticorrelation between E_5 and E_6: as E_6 increases, the expectation $\bar{E}_5$ for E_5 decreases. The next section will determine the precise meaning of this correlation.

6.4 Calculation of Means and Correlations

The 5-6 correlation actually cannot be neglected if our goal is to obtain Eq. (6.B) for the shape of the distribution of $\chi^2_{\pi,p}$ on stopped pion (proton) signal. The reason is that Eq. (6.A), as it stands, is only correct when its 6 degrees of freedom are *uncorrelated*. The constant S_{56}, introduced above, is meant to transform from the natural basis to an uncorrelated basis. In this section I will formalize what that means.

The constant S_{56}, whose intuitive meaning is clear from the argument in

§6.3, ought to be formally related to the covariance matrix. This is true, and can be revealed in a few short steps.

The expected energy $\bar{E}_5$ in plane 5 will now take this exact form,

$$\bar{E}_5 = \epsilon_5 + S_{56}(E_6 - \bar{E}_6) \tag{6.C}$$

where the meaning of the constant ϵ_5 is to be determined. The purpose of this form is that it allows a pattern to be continued for the remaining expectations $\bar{E}_1 \ldots \bar{E}_4$, as follows:

$$\begin{aligned}
\bar{E}_6 &= \epsilon_6 \\
\bar{E}_5 &= \epsilon_5 + S_{56}(E_6 - \bar{E}_6) \\
\bar{E}_4 &= \epsilon_4 + S_{45}(E_5 - \bar{E}_5) + S_{46}(E_6 - \bar{E}_6) \\
&\vdots \\
\bar{E}_1 &= \epsilon_1 + \sum_{j=2}^{6} S_{1j}(E_j - \bar{E}_j)
\end{aligned} \tag{6.C$*$}$$

This is the most general possible extension of the argument in §6.3.

We will now see that the constants S_{ij} relate simply to the covariance matrix. To use compact notation, I will now define

$$S_{ii} = 1$$

$$S_{ij} = 0 \quad (j < i)$$

and produce (after a little rearrangement)

$$E_i - \epsilon_i = \sum_{j=1}^{6} S_{ij}(E_j - \bar{E}_j) \qquad (6.C**)$$

so that S is the matrix that converts the vector of $E - \bar{E}$ into the vector of $E - \epsilon$. If I now *define* the matrix V by,

$$V = S\,\mathrm{diag}({\sigma_1}^2 \ldots {\sigma_6}^2)\,S^T \qquad (6.D)$$

$$S^T V^{-1} S = \mathrm{diag}(\frac{1}{{\sigma_1}^2} \ldots \frac{1}{{\sigma_6}^2}) \qquad (6.D*)$$

we see that V is manifestly symmetric, is diagonal if and only if the off-diagonals of S are zero, and its positive-definiteness is equivalent to the positiveness of ${\sigma_1}^2 \ldots {\sigma_6}^2$ (or the realness of $\sigma_1 \ldots \sigma_6$).

We see that V has all the properties of a covariance matrix. To prove that it is, we will determine its relationship to χ^2 (Eq. 6.A). By substituting Eq. (6.D$*$) into Eq. (6.A), and allowing S and S^T to act on $E - \bar{E}$ through two invocations of Eq. (6.C$**$), we obtain

$$\chi^2 = \sum_{i,j} \{V^{-1}\}_{ij}(E_i - \epsilon_i)(E_j - \epsilon_j)$$

which is the form of χ^2 when V is a covariance matrix.

From the derivation above, we finally obtain the interpretation of each element of Eq. (6.C) for the expected energy:

- ϵ_i is the mean energy in plane i.
- S_{ij} and σ are the covariance matrix $V = S\,\mathrm{diag}(\sigma)\,S^T$.

- $\bar{E}_i$ is the mean energy in plane i after diagonalizing the covariance.

We may now employ this set of quantities to calculate χ^2. When six plane energies $E_1 \ldots E_6$ and a track angle are given, χ^2 is calculated by the following method:

- Using the constants $S_{ij}(\theta; m)$ and $\epsilon_i(\theta; m)$, calculate the six expectations $\bar{E}_i$ through Eq. (6.C$*$).
- Calculate the six differences $E_i - \bar{E}_i$.
- Using the constants $\sigma_i(\theta; m)$, calculate χ^2 by Eq. (6.A).

The χ^2 calculated in this manner is guaranteed to have the shape of Eq. (6.B), provided S_{ij} and σ_i faithfully reproduce the covariance.

To produce V (from which S and σ are obtained, see Appendix B) and ϵ, we need to simulate the detector materials and photo-statistics. I do not use the full-featured GEANT4-based Monte Carlo to perform this task, since it can be done more efficiently by a stand-alone program. Fig. 6.2 shows how the simulation works. The material is divided into *active* and *passive* sections. The total plane thickness, active plus passive, is $L = 2.02$ g/cm^2. In order to keep my stand-alone simulation in agreement with the GEANT4 based detector simulator, I found that 1.60 g/cm^2 should be used for the active thickness, rather than the nominal 1.65.

A stopped-particle simulator does not need to care about the particle's initial momentum. It may begin at the stop point and work backward. The total energy is initialized to the particle mass m. The stop point x_0 is chosen uniformly. Now, the particle is propagated backward through 11 (12) slices if

it stops in the last active (passive) slice. Each propagation step performs the following four actions:

1. *Convert the current energy E to a nominal range X_0*, using the C.S.D.A. (Figure 6.1). Note, this is equal to the particle's present spatial position only when fluctuations are not present.

2. *Step to the upstream edge of the current slice.* The step distance x_{step} will be assigned. This is a distance of $x_{\text{step}} = x_1$ (x_2) for passive (active) slices, except for the first step, which is $x_{\text{step}} = x_0 - x_1$ (x_0) if the first slice is passive (active).

3. *Choose a new total energy $E' = E(X_0 + x_{\text{step}}) + \eta$*, where η represents fluctuations. The fluctuation η is chosen by a random Gaussian.

   The full width w at half-maximum of the energy loss fluctuation is given in reference [36, §30.2.7] by

   $$w = \frac{2KZx_{\text{step}}}{A\beta^2}.$$

   The full width at half-maximum of a Gaussian is used, i.e., $w/\sigma = 2(2\log 2)^{1/2}$. The particle speed β^2 is evaluated at $E(X_0 + x_{\text{step}})$. (The material constant KZ/A is calculated to be 0.228 MeV cm^2/g, using the atomic fractions in Table 2.1 and a standard table of atomic weights.)

   If the current slice is active, then E' minus the initial energy is the unsmeared hit value. If E' is less than the initial E, then a different η is chosen from the same distribution until $E' > E$.

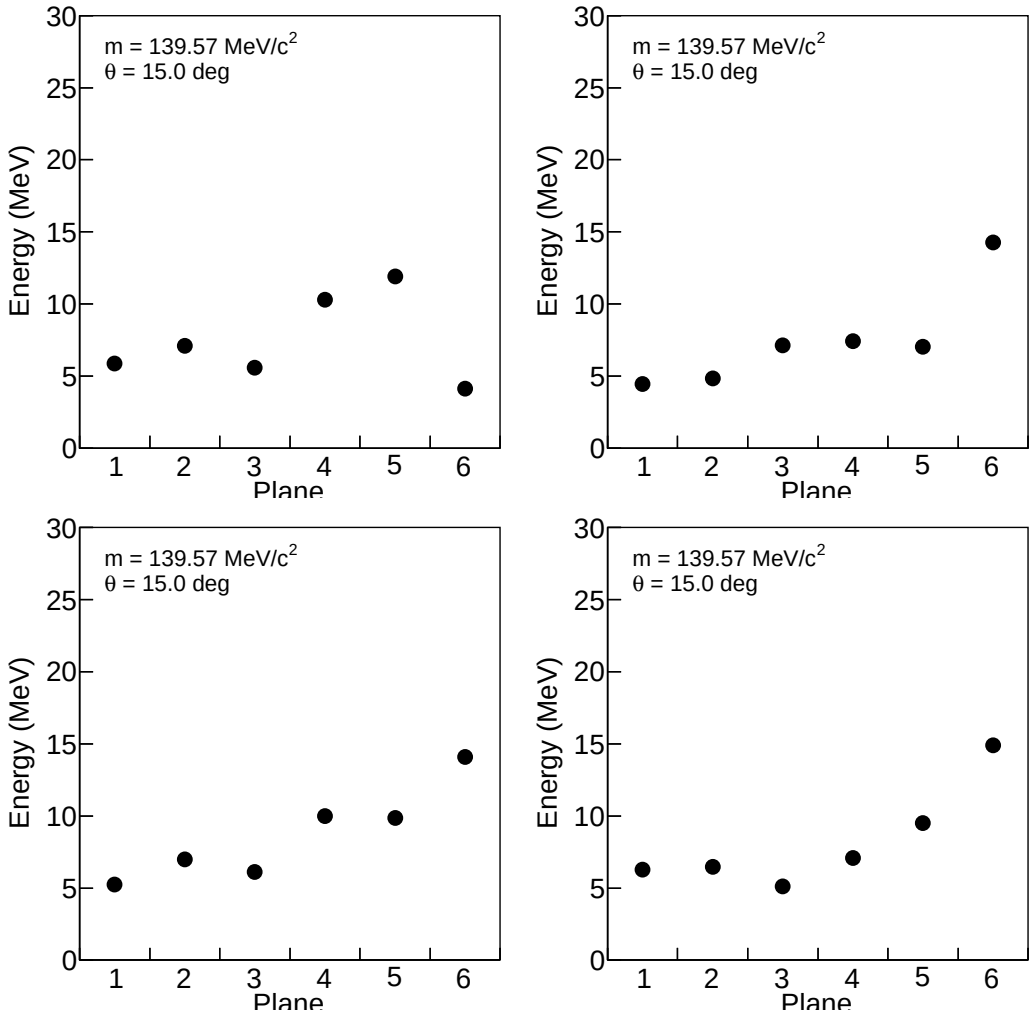

Figure 6.3: *Simulated tracks at* $\theta = 15°$. Four events from the stand-alone Monte Carlo are shown.

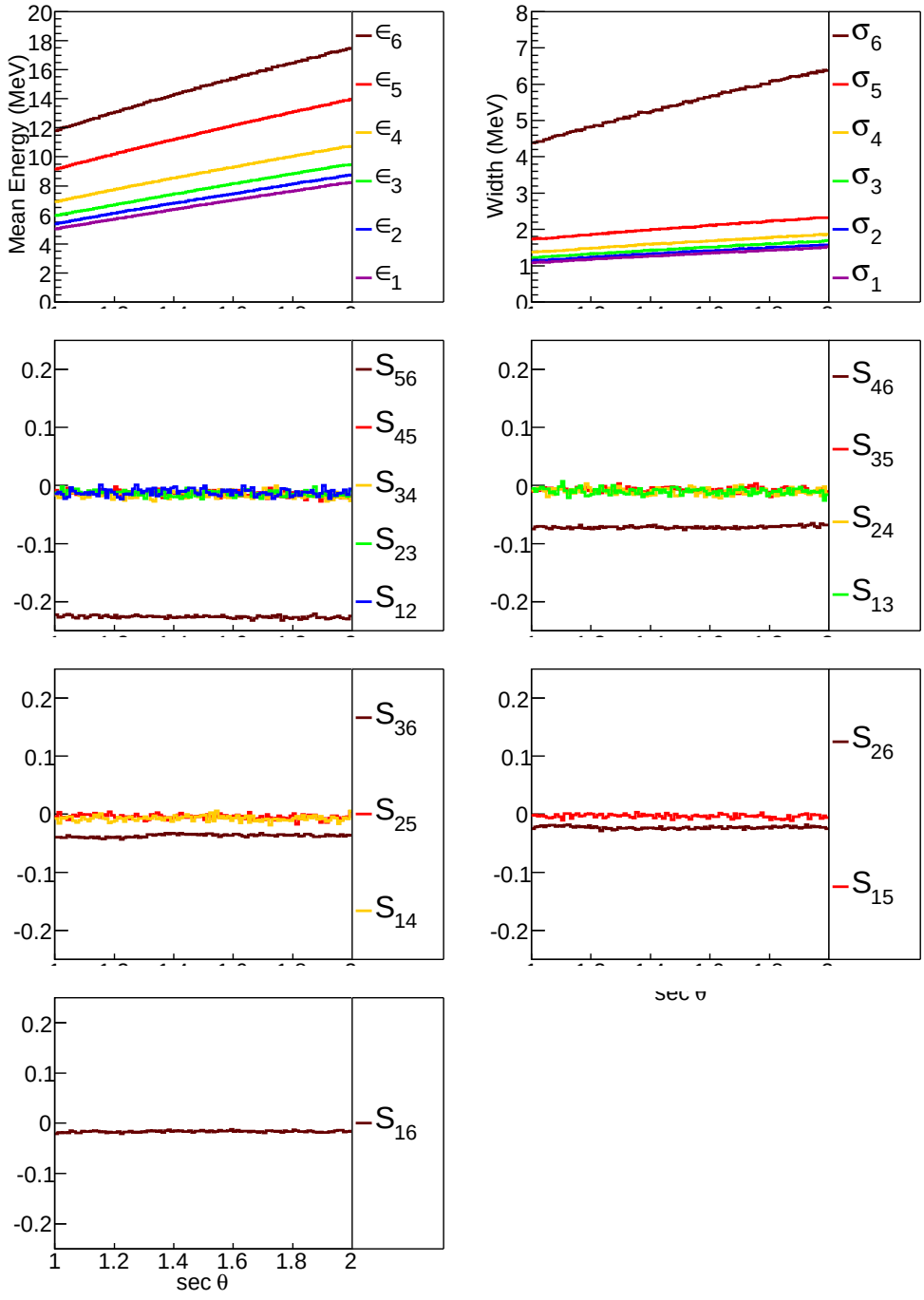

Figure 6.4: *Stopping pion parameters.* Displayed here are the results for $m = m_\pi$ and $0 < \theta < 60°$ from the stand-alone Monte Carlo.

4. *If the current slice is active,* then the hit is returned with photo-statistical smearing. To apply smearing, we simulate the sharing of the charge in two triangles (see Figure 3.2). The numbers n_1 and n_2 represent the number of p.e. in each channel respectively. The parameter $\xi = n_1/(n_1+n_2)$ is chosen from a uniform distribution to represent the sharing fraction. Then n_1 and n_2 are assigned, using the constraint that their sum converted to MeV must be equal to the plane energy. Then to each n_i, a number from a random Gaussian with width $\sqrt{n_i}$ is added. The sum n_1+n_2 is is converted back to MeV. The value 0.15 MeV/p.e. is used for conversion between p.e. and MeV.

Using the above Monte Carlo, I simulate 30,000 tracks at each fixed angle θ for 100 angles between 0 and 60°. From this sample we obtain $\epsilon_i = \langle\, E_i \,\rangle$ and $V_{ij} = \langle\, (E_i - \epsilon_i)(E_j - \epsilon_j) \,\rangle$ as functions of θ. From V_{ij}, we obtain S_{ij} and σ_i (Appendix B).

From the results in Fig. 6.4, a simple angular dependence is suggested. The entire result can be expressed in just 29 numbers, using

$$\begin{aligned}
\epsilon_i(\theta; m) &= a_i(m) + b_i(m)(\sec\theta - 1) \\
\sigma_i(\theta; m) &= c_i(m) + d_i(m)(\sec\theta - 1) \\
S_{i6}(\theta; m) &= S_{i6}(m) \\
S_{ij}(\theta; m) &= 0 \quad (j \neq 6)
\end{aligned}$$

Thus the numbers $a_i(m),\ b_i(m),\ c_i(m),\ d_i(m),$ and $S_{i6}(m)$ are sufficient to describe the stopping particle of mass m at all angles θ.

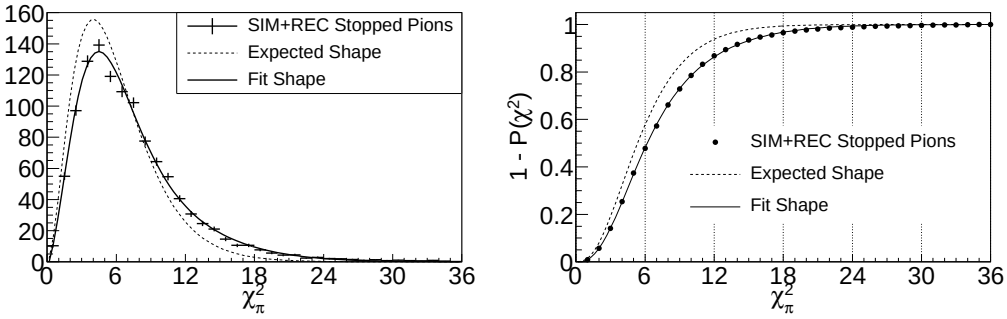

Figure 6.5: *Corrections to the signal shape.*

6.5 Corrections to the Signal Shape from Full-Featured Monte Carlo

Now we return to the full Monte Carlo, using events simulated and reconstructed in the detector. Using the categories defined in §4.3, I select stopped pions. I take the 6 plane energies from their reconstructed tracks. Finally I evaluate χ^2_π using Eq. (6.A). The result is shown in Fig. 6.5.

The distribution of χ^2_π is slightly wider than a true χ^2 distribution. The shape can be expressed by a small perturbation. Recall from Eq. (6.B) that

Degree	Expected	Fit
Constant	1	1 ± 0 (*fixed*)
Linear	1/2	0.51 ± 0.01
Quadratic	1/8	0.11 ± 0.02
Cubic	0	0.014 ± 0.007
4^{th}	0	-0.001 ± 0.001
5^{th}	0	0.00015 ± 0.00005

Table 6.1: Adjustment to $P(\chi^2)$ for the signal.

the probability integral P is given by

$$P(\chi^2) = \left(1 + \chi^2/2 + \chi^4/8\right) \exp(-\chi^2/2).$$

We notice that the functional form is polynomial(x) $\times$ exp($-x/2$). To vary the shape, I let the factor of exp($-x/2$) become an arbitrary polynomial with constant term 1. The constant term 1 in the expression for $P(\chi^2)$ conserves probability. By fixing only the constant term, normalization is preserved while the fitter may modify the other terms arbitrarily.

Table 6.1 shows the result of a fit allowing terms up to quintic. The linear and quadratic terms agree with the true formula. The quartic term is consistent with zero. However, the fit wants to add small cubic and quintic terms.

6.6 Signal/Background Separation

Figs. 6.6 and 6.7 show the distributions of $\chi_p^2 i$ and χ_p^2 for all events passing the cuts in Chapter 5. These plots require extra Monte Carlo truth information to be interpreted properly. The plot colors are as before as long as the found track is a pion in the Stop category (§4.3). I change the color in the histogram for other cases: to green if it is a pion, but not in the Stop category; to gold if it is a proton; and to white hatched if it is anything besides.

The linear scale panel of Fig. 6.6 also shows a data-driven background prediction with errors. The prediction is obtained in the following manner.

We assume that the signal has the shape described in Table 6.1. The S/B

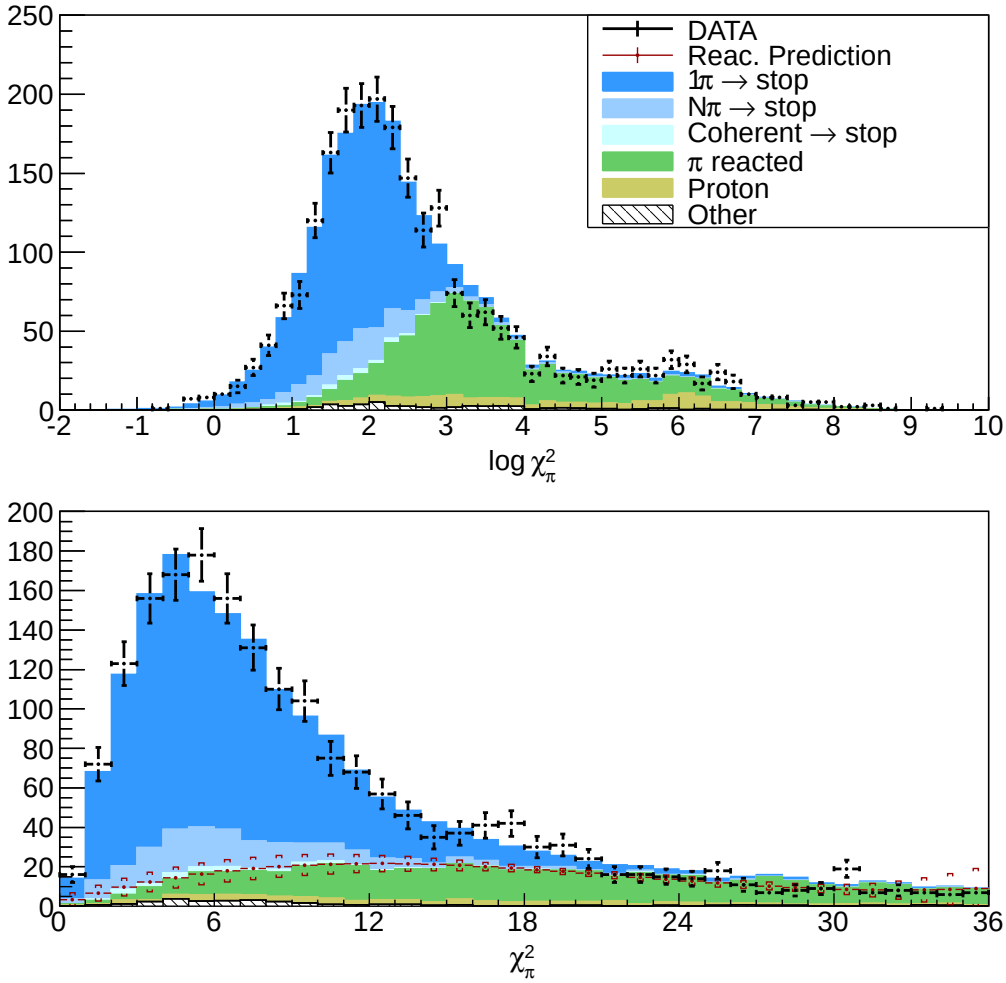

Figure 6.6: *Distribution of* χ^2_π, linear and log.

separation comes from a fit to data, in this form:

$$\text{data}(\chi^2_\pi) = A\tilde{f}(\chi^2_\pi) + \text{background}(\chi^2_\pi) \tag{6.E}$$

where A is a parameter representing the signal scale, $\tilde{f}(\chi^2_\pi)$ is the perturbed χ^2 distribution, and background(χ^2_π) is an arbitrary function with a finite number of parameters.

The range of the fit is $0 < \chi^2_\pi < 36$. Data at larger values of χ^2_π is assumed

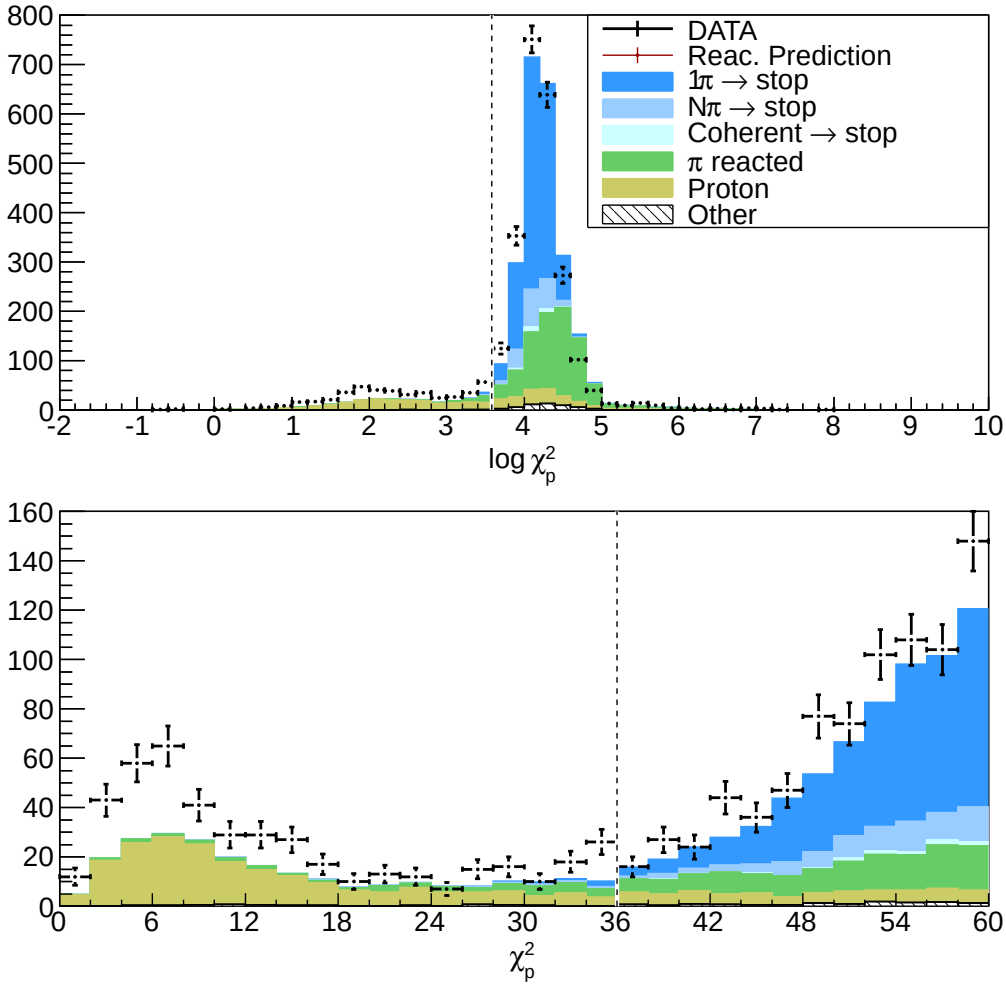

Figure 6.7: *Distribution of* χ^2_p, linear and log. The proton rejector cut $\chi^2_p > 36$ is shown.

to be all background.

A theorem from real analysis (see Ref. [39]) states that polynomials are good approximators of arbitrary continuous functions on a finite domain $[x_1, x_2]$ (where here, $x_1 = 0$ and $x_2 = 36$). As the degree of the polynomial increases, the approximation gets better inside the domain, and worse outside. A polynomial of high degree tends toward ∞ very quickly for $x < x_1$ or $x > x_2$, regardless what the approximated function is doing in those regions. Inside

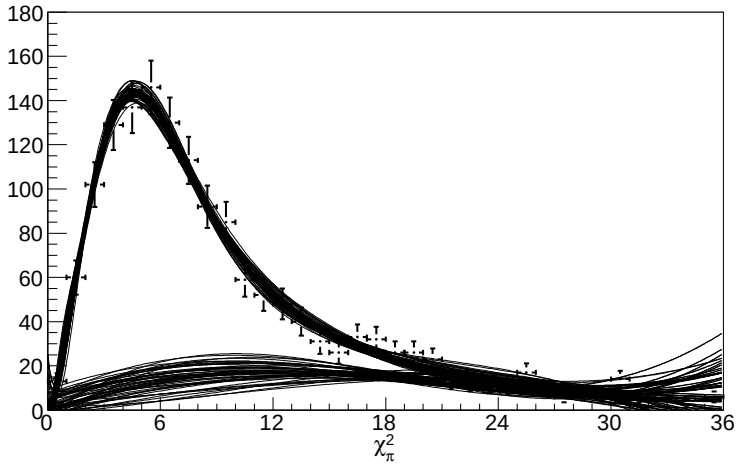

Figure 6.8: *Uncertainty of the background result.* 100 perturbations of fit (6.E) are shown. The upper family of curves is signal plus background; the lower family of curves is background alone. The background error band in Fig. 6.6 is calculated by the spread of the family of background curves in each bin.

the defined domain, however, its flexibility to mimic the approximated function improves as its degree increases.

If a polynomial form of the background is chosen then the main question is what degree. By experimenting with different degree polynomials, I find that the degree cannot be greater than cubic without some further constraint being imposed or some fit-guiding action being taken by the user. A quartic (or higher) polynomial naturally makes a "Bactrian Camel" shape, i.e., with two humps. The problem with this is that by the design of the S/B separation, the background is expected not to be able to produce the characteristic peak of the χ^2 distribution at $\chi^2_\pi = 4$. A quartic polynomial could let one of its humps look like this signal. But by having degree no higher degree than cubic, the background cannot mimic the signal peak, and the fit is guaranteed to make sense the first time.

With the degree of the background polynomial settled at cubic (four free parameters), the dimension of the fit becomes five. The fifth parameter is signal scale A in Eq. (6.E).

After the fit is performed, its uncertainty must be evaluated. This is done by taking the spread of 1000 random perturbations around the best fit result. 100 of these perturbations are shown in Fig. 6.8. Each perturbation has been produced by the method in Appendix C. Both the signal shape fit (5 parameters, perturbed around the values given in Table 6.1) and fit (6.E) (5 parameters) are perturbed—a total of 10 parameters to be randomly changed—for each curve in Fig. 6.8.

6.7 Closure Test

From Fig. 6.6, it can be seen that the reacted-pions prediction (red points) follows the green part of the Monte Carlo, similarly as the data points follow the total Monte Carlo. To test the robustness of the S/B separation result, I have performed the fit (6.E) using Monte Carlo as data, while biasing the weight of reacted pion events (Fig. 6.9). The reacted pions prediction follows along with the green histogram in each case, demonstrating the robustness of the background prediction.

6.8 Utilization of Sideband

The most important part of S/B separation is being able to perform that separation on any histogram—not just on the histogram of χ^2_π, as shown previously.

I will make the fundamental assumption that the distribution of χ^2_π (Fig.

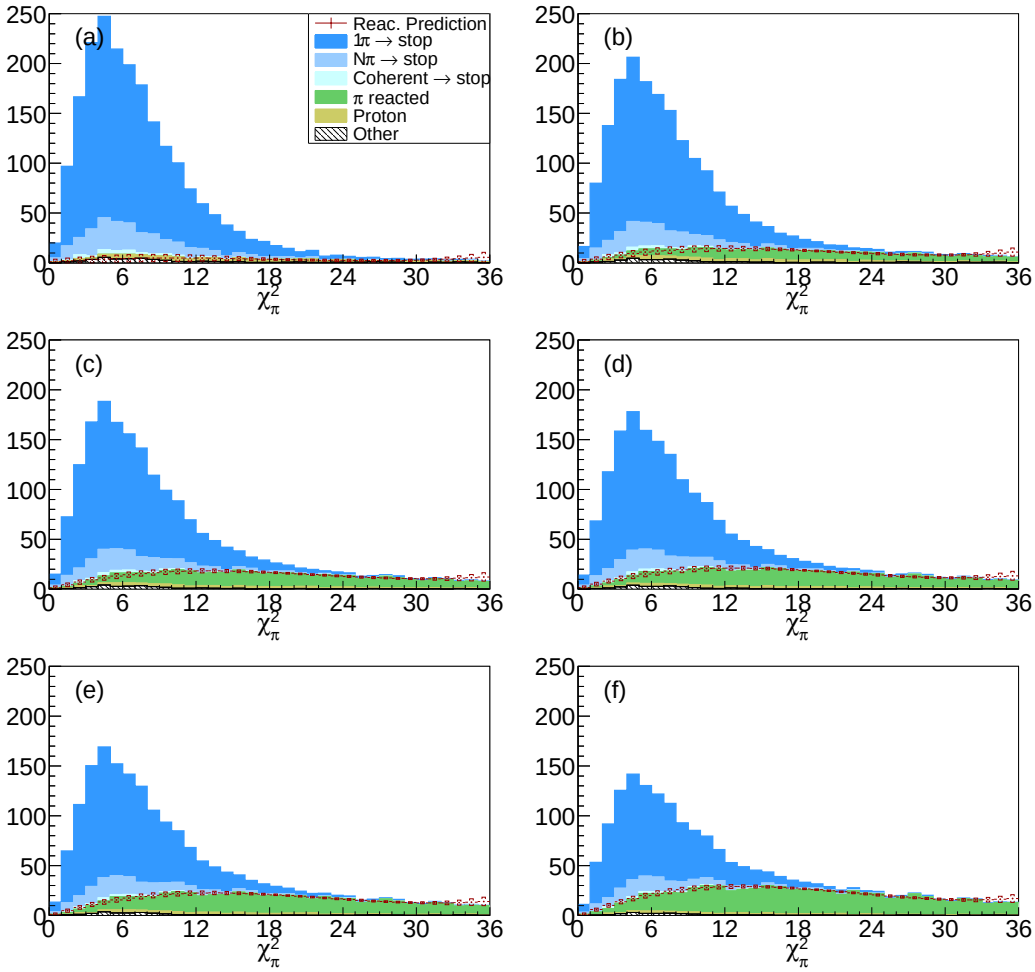

Figure 6.9: *Closure test for signal/background separation.* The reac. prediction is taken from Monte Carlo as data. Change in the reaction cross-section is simulated by reweighting the "green" events in each panel. The weights are (left to right, from top): 0, 0.5, 0.8, 1.0, 1.2, 2.0. (Since the plots are area-normalized, blue area decreases with increasing green.)

6.6) is unchanged when restricted to a bin (say, 100 MeV $< T_\pi <$ 110 MeV or 0.1 GeV^2 $< Q^2 <$ 0.2 GeV^2). Let us define the ratio $R = N_{\text{background}}(\chi^2_\pi < 18)/N(\chi^2_\pi > 18)$. The numerator comes from the fit, and the denominator comes from data. Then the reacted pion contribution in any bin can be found by $(1 + R)$ times the sideband in that bin. (The assumption here is that the sideband at $\chi^2_\pi > 18$ is virtually all background.) Finally, the error on R is propagated into the total error on the histogram's background prediction.

Fig. 6.11 shows the result of background prediction using Monte Carlo. It is seen that the red, predicted background generally follows the green true background. Finally, Fig. 6.12 shows the background prediction on data.

When background is subtracted, the pion kinetic energy residual becomes narrow (Figs. 6.11(b), 6.13). On Fig. 6.13, each vertical slice is normalized to all the others. Fig. 6.10 shows there are vanishingly few pions in the off-center region at $T_\pi > 300$ MeV.

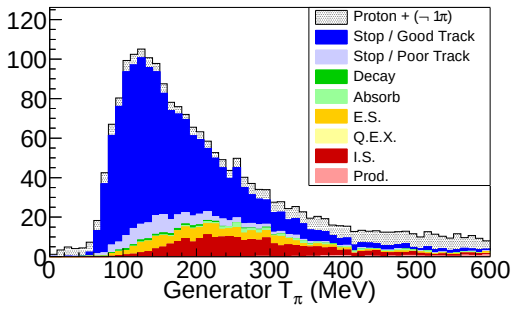

Figure 6.10: *True pion kinetic energy.*

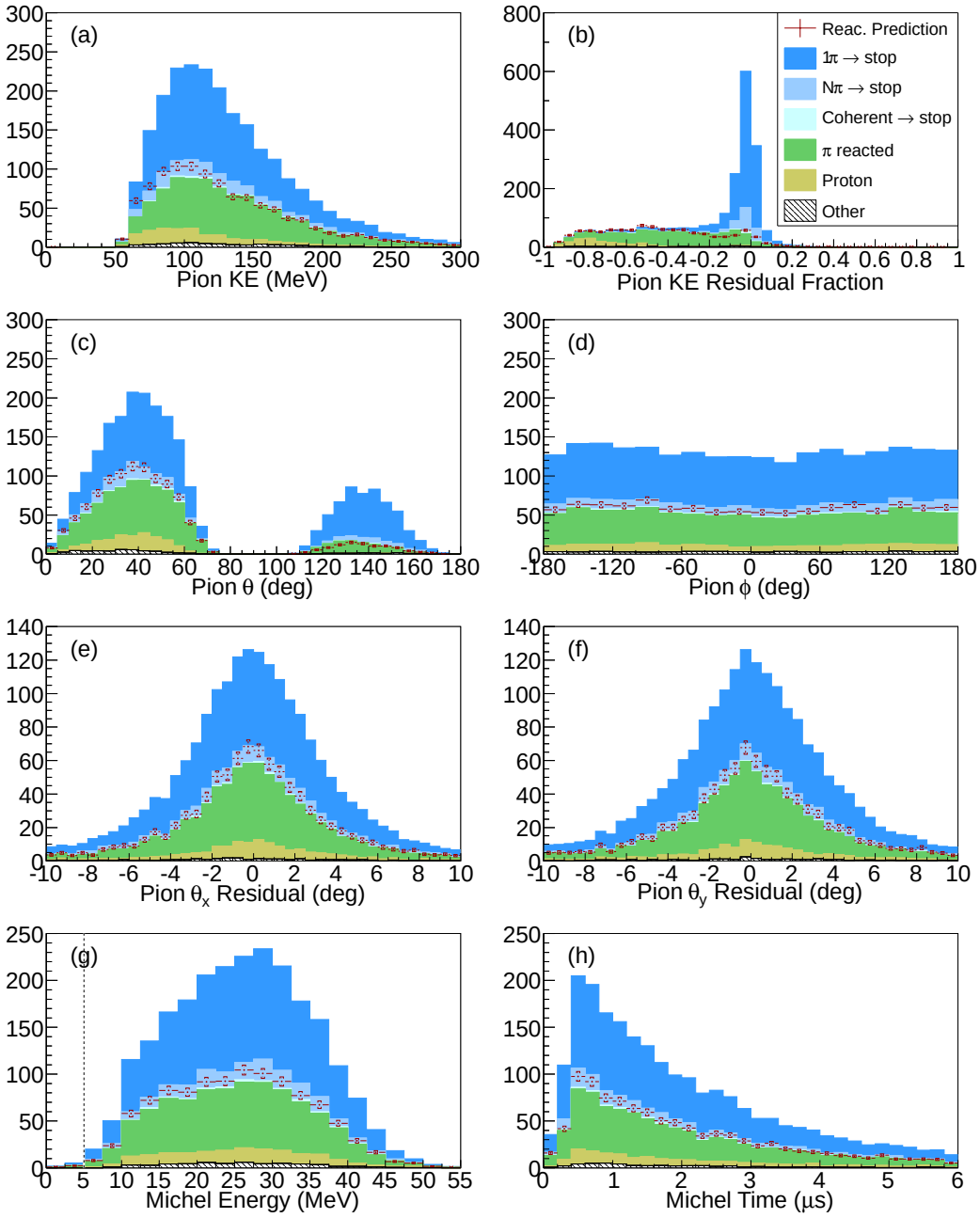

Figure 6.11: *Reaction predictions from Monte Carlo.*

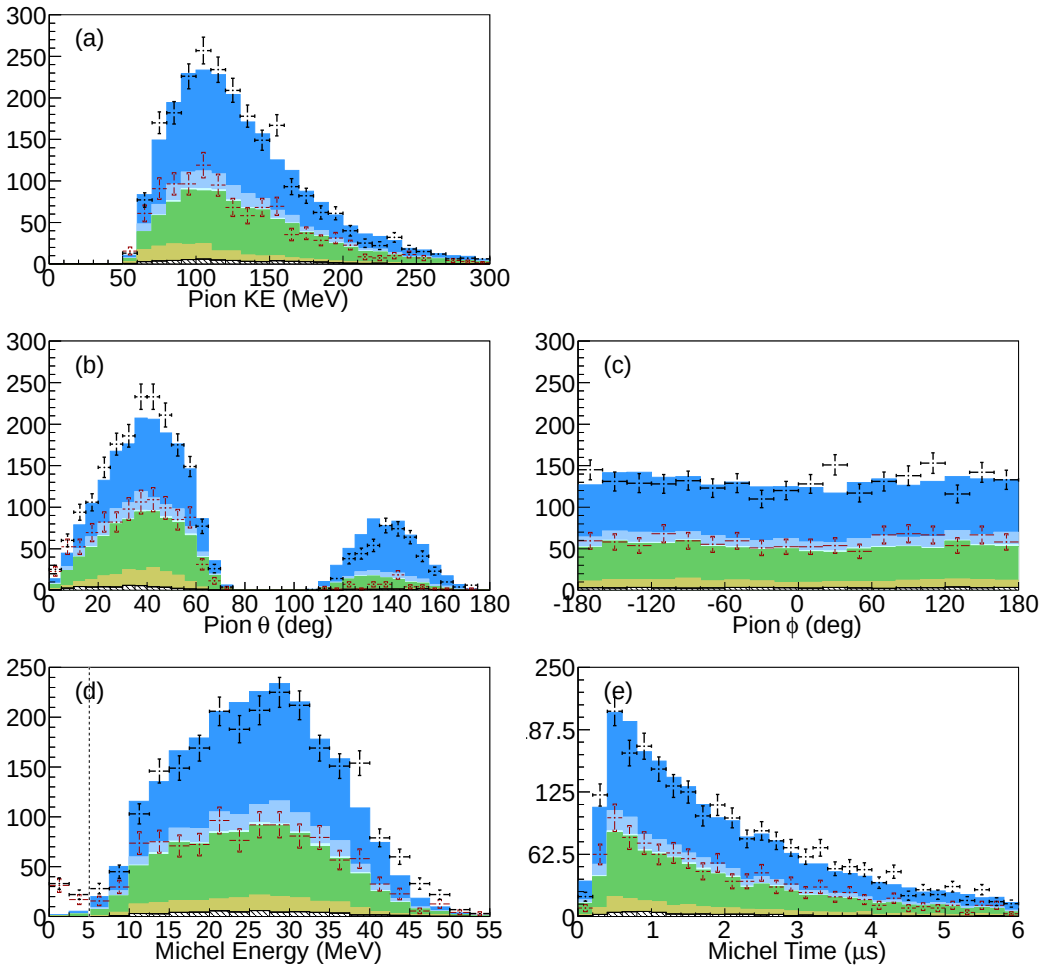

Figure 6.12: *Reaction predictions from data.*

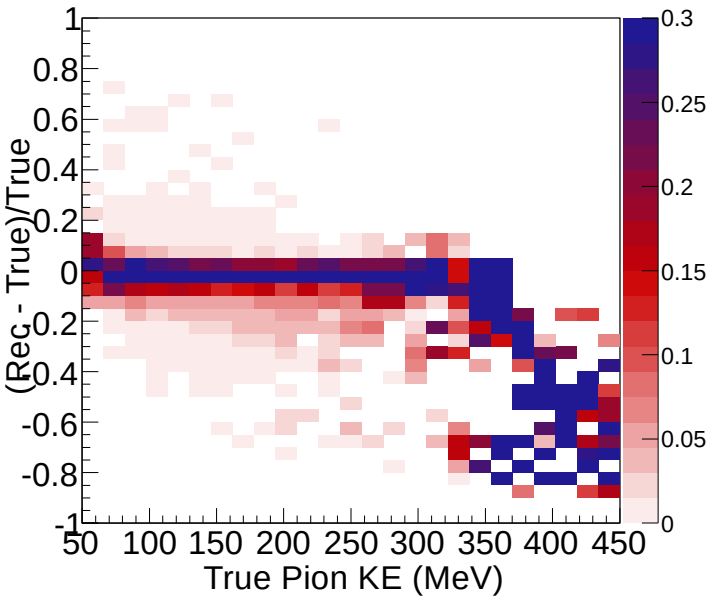

Figure 6.13: *Pion kinetic energy residual, with subtraction.* Compare Figs. 1.7 and 5.10.

Chapter 7

Sensitivity to the Axial Mass

7.1 Event Reconstruction using the Single-π Hypothesis

Where we left off, the event energy $\widetilde{E_\nu}$ has been measured by the calorimetric response of every channel in the MINERvA detector. But we want to do better. On single pion events, where the muon and pion vectors have been measured, it is possible to compute E_ν from the vectors, rather than from the total calorimetric energy in the detector, and this turns out yield much smaller errors on the hadroinc mass W, although a noticable difference has not been achieved on either E_ν or Q^2. I will begin with a review of the relativistic kinematics.

Although most readers are familiar with relativistic 2-body scattering, our channel $\nu\, N \to \mu\, \pi\, N'$ has a 3-body final state, and a massless particle of unknown energy in the initial state; these features make the algebra less familiar. Recall also that only two of the three final-state particles will be measured—the recoiling nucleon N' is not measured. This will lead us to a formula for the unknown energy E_ν involving the vectors of only two final particles, in this case the muon and the pion.

The E_ν formula I refer to is stated in some previous references (see, for example, [17, Equation 2]). However, I was not able to locate a published derivation of the formula. For this reason, I will begin this chapter with a

derivation.

The following lemma is useful: for any relativistic particle with mass m, the kinetic energy $T = E - m$ is given by

$$E - m = \frac{1}{2}\frac{\{m - (E - p_z)\}^2 + {p_T}^2}{E - p_z}. \tag{7.A}$$

The proof is in cross-multipyling and expanding all products, with the result that the mass-energy relationship for relativistic particles, $m^2 = E^2 - p^2$, is recovered. Suppose we only know two quantities x and y, where $x = p_T = \sqrt{{p_x}^2 + {p_y}^2}$ and $y = E - p_z$. We would like to get the particle's kinetic energy T using just x and y. This puzzle is not merely an exercise: we will use it for real in the next step.

With (7.A) in hand, we will now solve the collision $\nu N \to \mu \pi N'$ completely. Conservation in all four dimensions—energy, p_x, p_y, and p_z—will be used. The neutrino direction defines the z-axis. From conservation of energy and p_z we state,

$$E_\nu + m_N = E_\mu + E_\pi + E_N \tag{7.B}$$

$$E_\nu = p_{z(\mu)} + p_{z(\pi)} + p_{z(N)}. \tag{7.C}$$

Now subtracting (7.C) from (7.B), the neutrino energy cancels and we obtain this "unitarity" rule,

$$m_N = \sum_{\mu,\,\pi,\,N} (E - p_z) \tag{7.D}$$

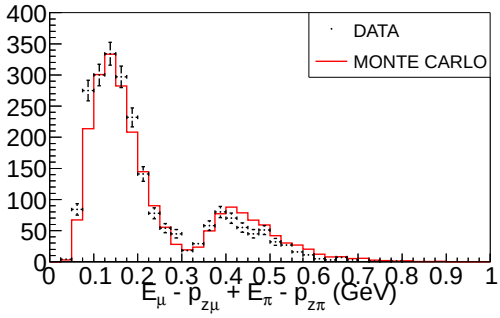

Figure 7.1: $\sum_{\mu,\pi}(E - p_z)$

involving the three final particles.[1] The quantity $E - p_z$ has been measured for two of the final particles, the muon and the pion (Fig. 7.1). For the remaining particle, the recoil nucleon, Eq. (7.D) tells us what $E - p_z$ is.

The key now is to apply the lemma, Eq. (7.A), to the recoiling nucleon whose $E - p_z$ has become known. We also need the nucleon's transverse momentum p_T, but this is supplied by the two remaining conservations: the sum of the transverse momentum vectors of the muon and pion must be equal and opposite to the transverse momentum vector of the recoiling nucleon. Now, with $E - p_z$ and p_T known for the nucleon, its kinetic energy is calculated. The neutrino energy E_ν is found as $E_\nu = E_\mu + E_\pi + T_N$.

For efficient computation, T_N is calculated by considering an off-shell pseudoparticle "$\mu\pi$" whose 4-momentum is equal to muon plus pion. The pseudoparticle also helps us compare our result to the quasi-elastic scattering result. If $E_\pi \to 0$ and $\vec{p}_\pi \to \vec{0}$, the pseudoparticle becomes on-shell with mass m_μ and the solution for quasi-elastic scattering is recovered. (Compare, for example, Eq. (4.10) of reference [18].)

Finally, the other kinematic variables Q^2 and W come from their usual

[1] Comparing Eq. (7.D) to Equation 2 of reference [17], it appears that [17]'s formula for E_ν is stated as a ratio of two negatives.

definitions, as below (compare Eq. 5.B):

$$
\begin{aligned}
&E_\nu = E_\mu + E_\pi \\
&+\frac{1}{2}\frac{(E_\mu - p_{z(\mu)} + E_\pi - p_{z(\pi)})^2 + (p_{x(\mu)} + p_{x(\pi)})^2 + (p_{y(\mu)} + p_{y(\pi)})^2}{m_N - (E_\mu - p_{z(\mu)} + E_\pi - p_{z(\pi)})} \\
&Q^2 = 2E_\nu(E_\mu - p_{z(\mu)}) - m_\mu^2 \\
&W = \sqrt{\max(0, m_N^2 + 2m_N(E_\pi + T_N) - Q^2)}
\end{aligned}
\tag{7.E}
$$

It should be emphasized that Eq. (7.E) introduces feeddown from higher resonance and D.I.S. events. The derivation is valid in the 1π case, because the sum (7.D) contains no more than one particle that is not measured. For the $N\pi$ case, the derivation breaks down at the step when Lemma (7.A) is applied. Three things have been supposed at this step: that there was one unmeasured particle, that the unmeasured particle was on-shell, and that its mass was m_N. None of these hold when both a recoiling nucleon and one (or more than one) pion are not measured. This means in particular that it is invalid for $N\pi$ ($N > 1$) events. If another pion were produced and not detected—and this is the case for all of the $N\pi$ background that has survived—then W is highly underestimated, by the mass-energy of the unmeasured pion(s) not being accounted for. From Monte Carlo it appears that this W feed-down lands in the middle of the Δ resonance region in the worst way possible (Fig. 7.8(g)).

We have relied on the calorimetry to cut as much of the $N\pi$ background as possible. When Eq. (7.E) is applied on safe one-pion events, and the prediction for reacted pions is subtracted, narrower residuals can be achieved compared to

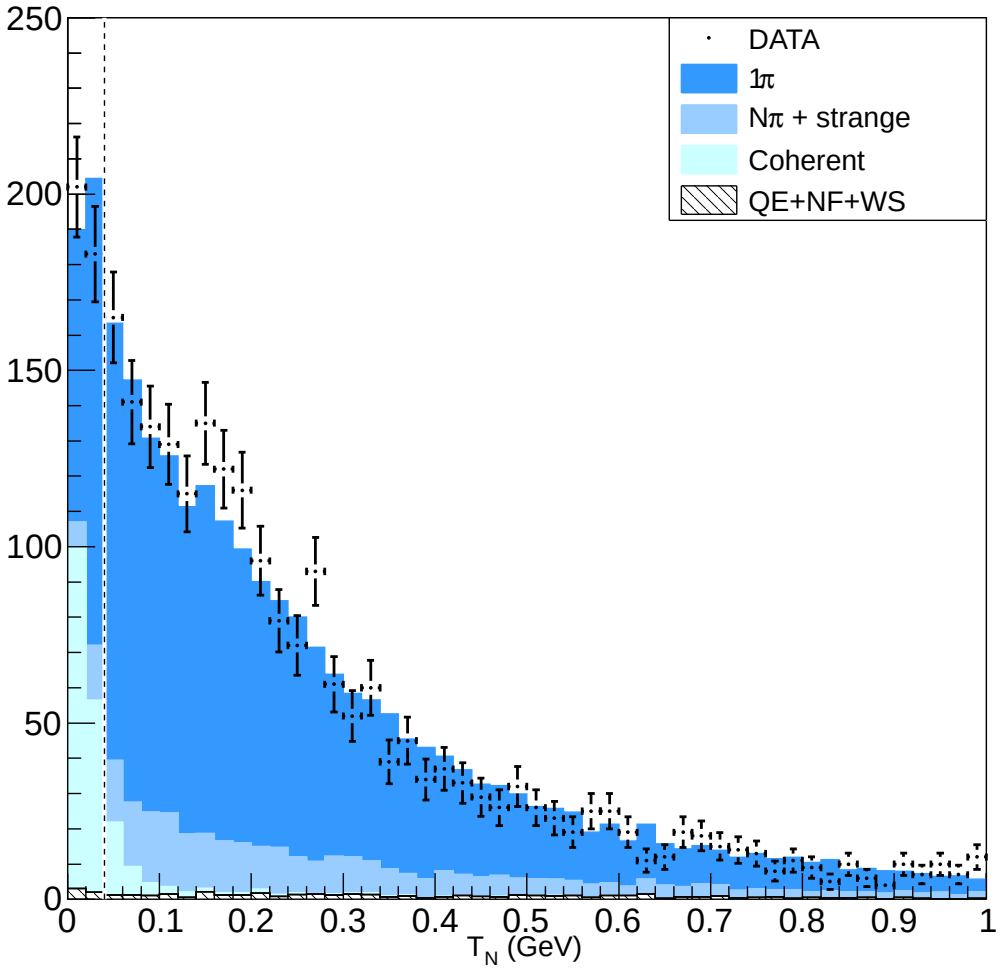

Figure 7.2: *Recoil of the nucleon,* as calculated by the long fraction bar in (7.E). The cut $T_N > 40$ MeV removes coherent pion production events from the sample.

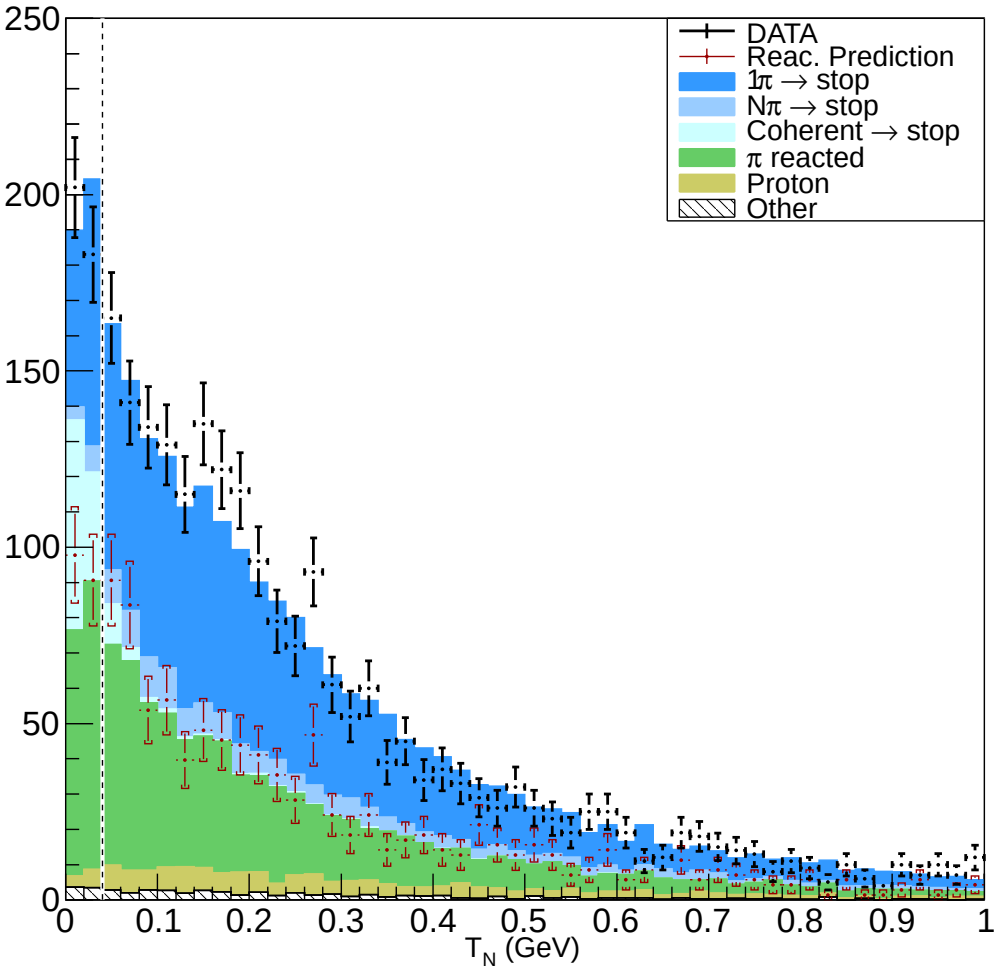

Figure 7.3: *Recoil of the nucleon, with bkg. prediction.*

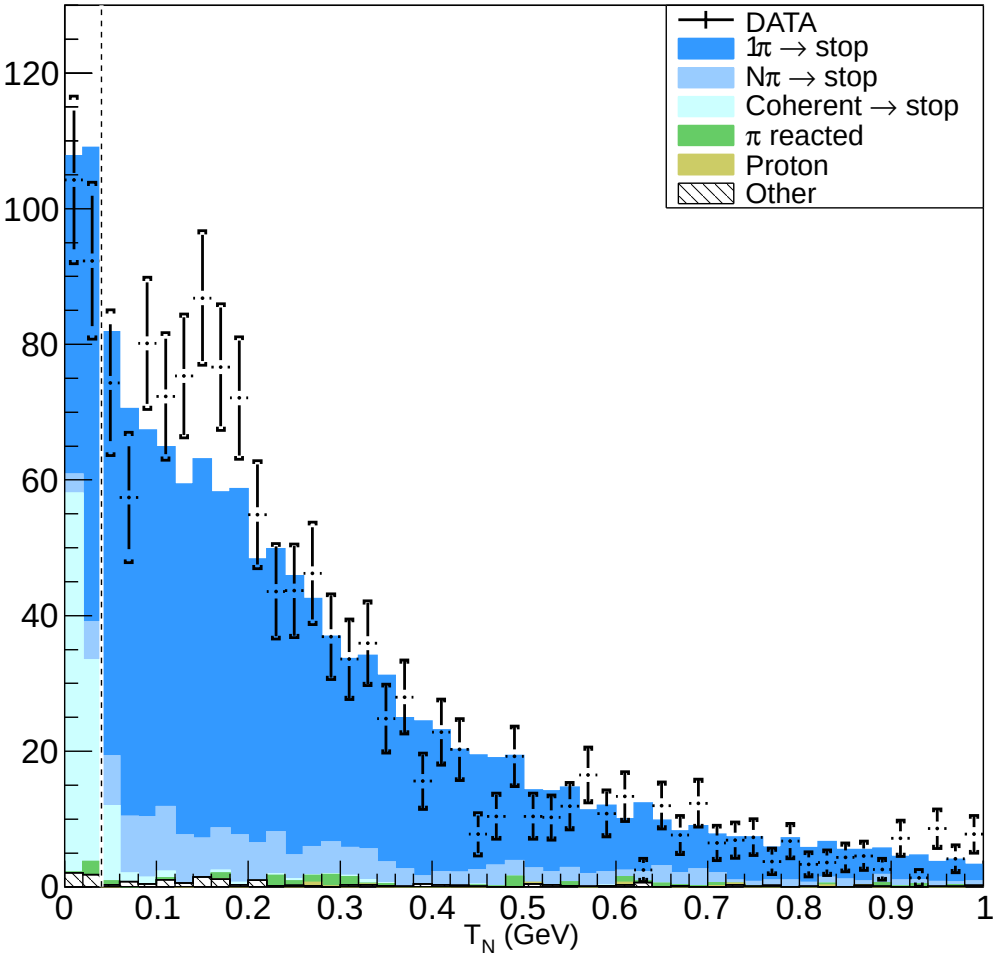

Figure 7.4: *Recoil of the nucleon, subtracted.*

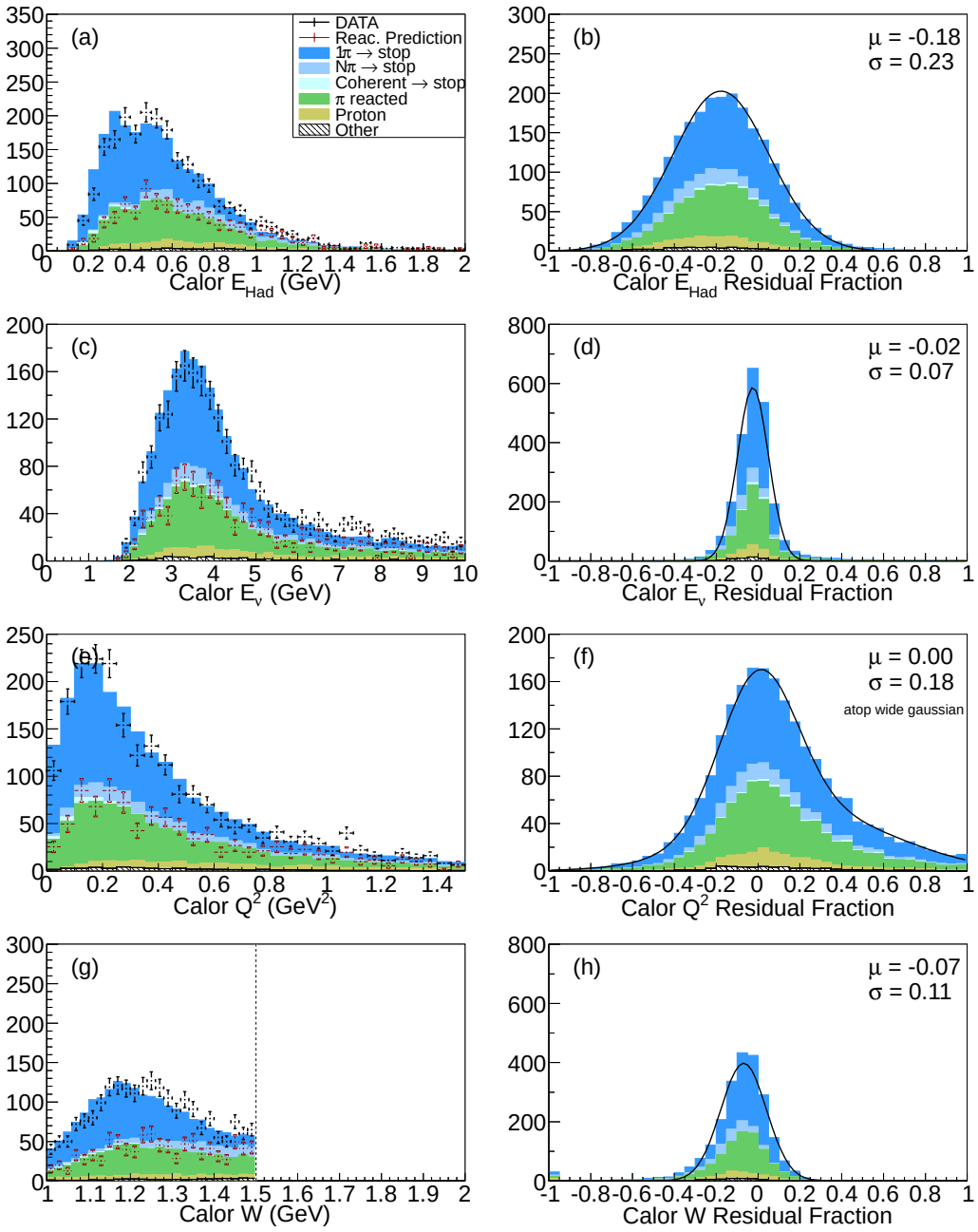

Figure 7.5: *Results of Eq. 5.B.* For $\widetilde{W}$, see also Figure 5.4.

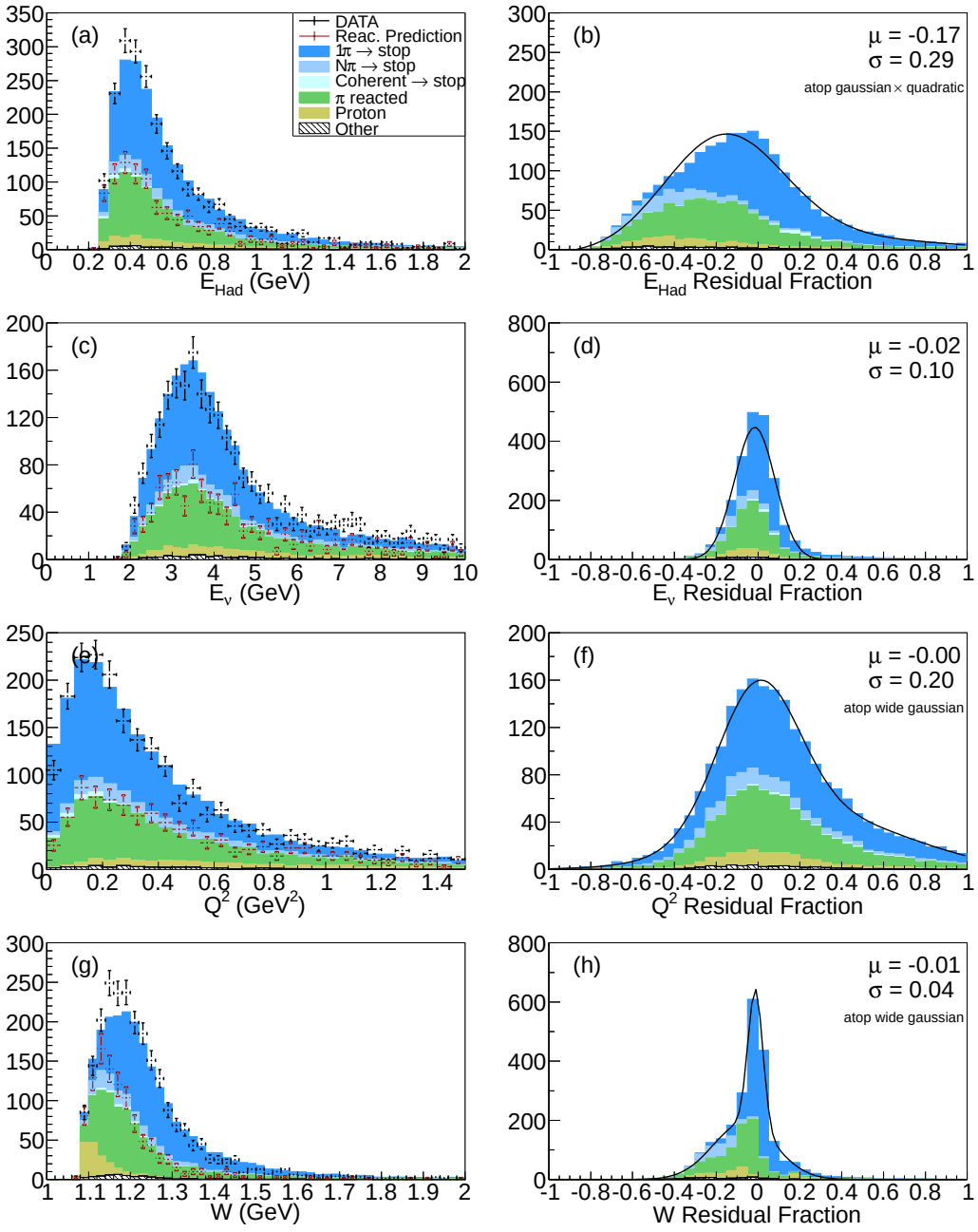

Figure 7.6: *Results of Eq. (7.E).*

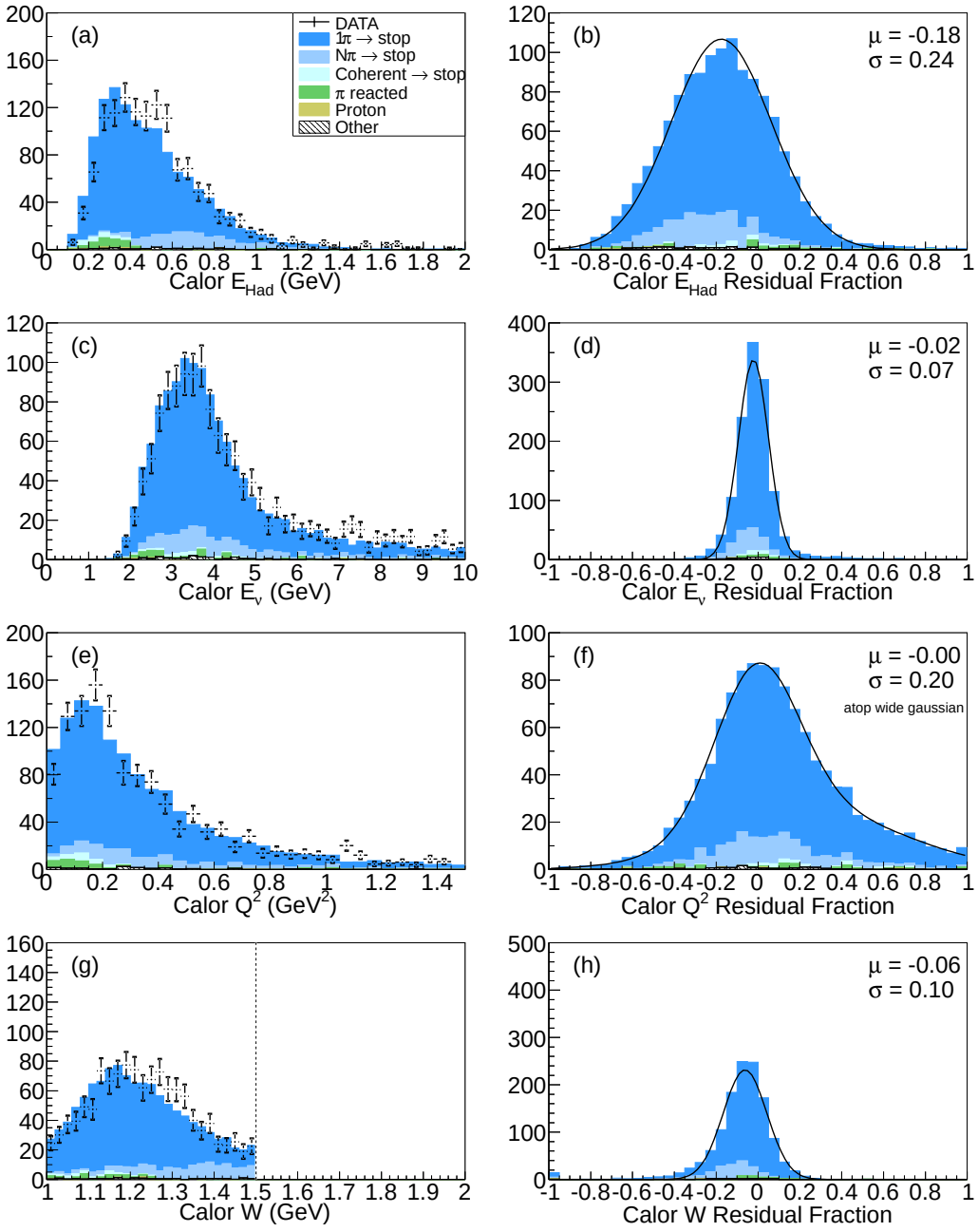

Figure 7.7: *Results of Eq. (5.B), subtracted.*

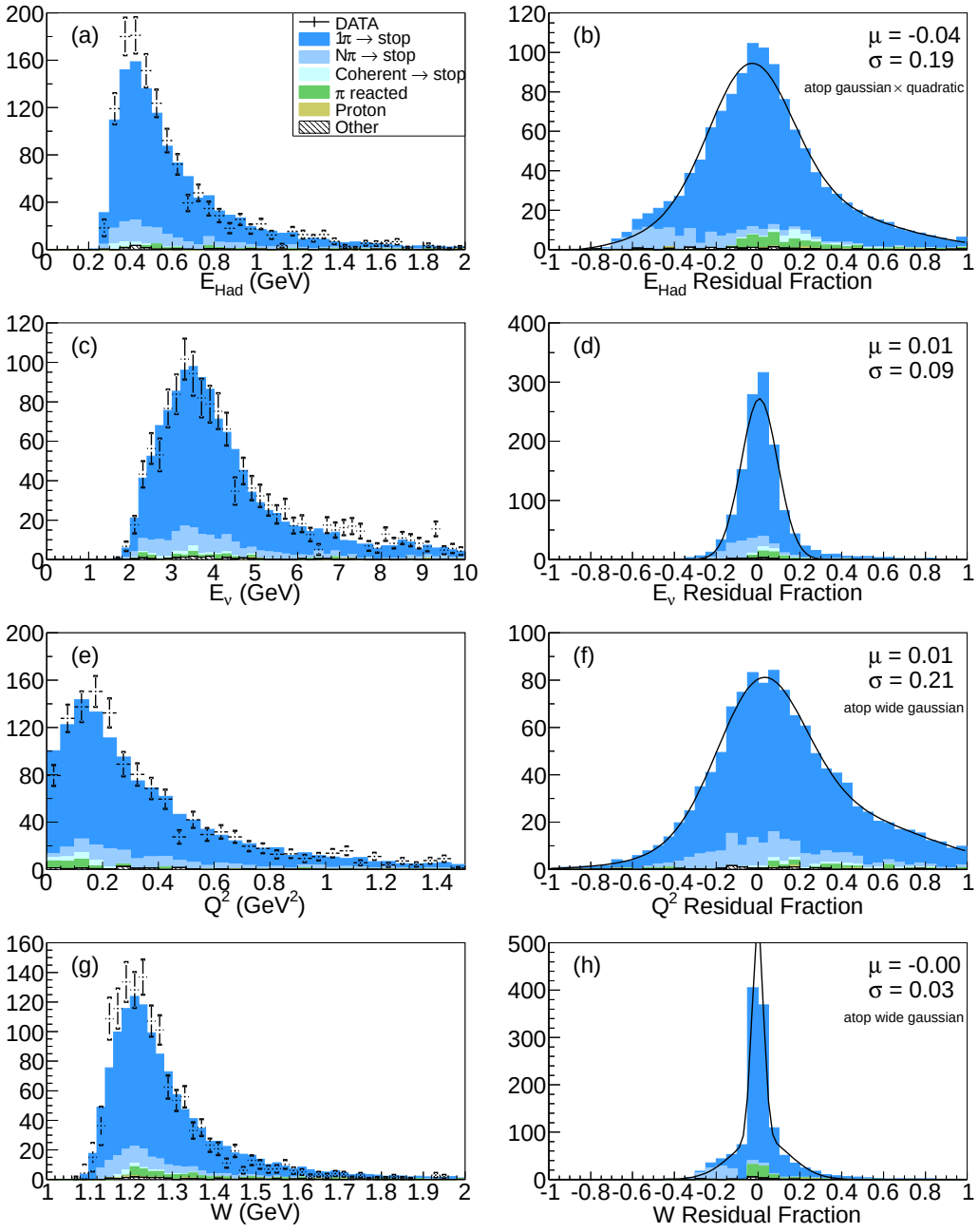

Figure 7.8: *Results of Eq. (7.E), subtracted.*

what Eq. (5.B) had told us earlier (Figs. 7.5–7.8). It is regrettable though that this improvement does not extend to E_ν or Q^2. Even perfect reconstruction of the hadroinc system could not help with either E_ν or Q^2. The muon energy E_μ is the dominant source of error in E_ν, and the muon energy squared ${E_\mu}^2$ is the dominant source of error in Q^2.

7.2 Production of the Q^2 Spectrum

Figs. 7.6 and 7.8 show the results of the event reconstruction equations (7.E). I will use the data and Monte Carlo from Fig. 7.8(e) to extract the axial mass. The data in Fig. 7.8(e) has few events per bin, with only ≈ 140 events in the largest bin. Since this implies fairly large statistical fluctuations (> 10 % in each bin), I will double the bin size for the M_A^Δ extraction.

Figs. 7.9(a) and (b) show the rebinned versions of Figs. 7.6(e) and 7.8(e), respectively. Fig. 7.9(b) will be the basis for the axial mass extraction.

Producing the Monte Carlo here is as important as producing the data. It is important at this point to use all the systematic errors available on the Monte Carlo. Table 4.1 gives the list of flux, cross-section, and background scale systematics that have been considered. The total of these errors and the Monte Carlo statistical error is plotted in Fig. 7.9 as a solid band around the Monte Carlo.

A word should be said about how the M.C. error is made. For each of a thousand so-called "universes," the vector of parameters in Table 4.1 is perturbed by a vector of random Gaussians. The parameter adjustments are accomplished by reweighting of events. In each universe, after parameters

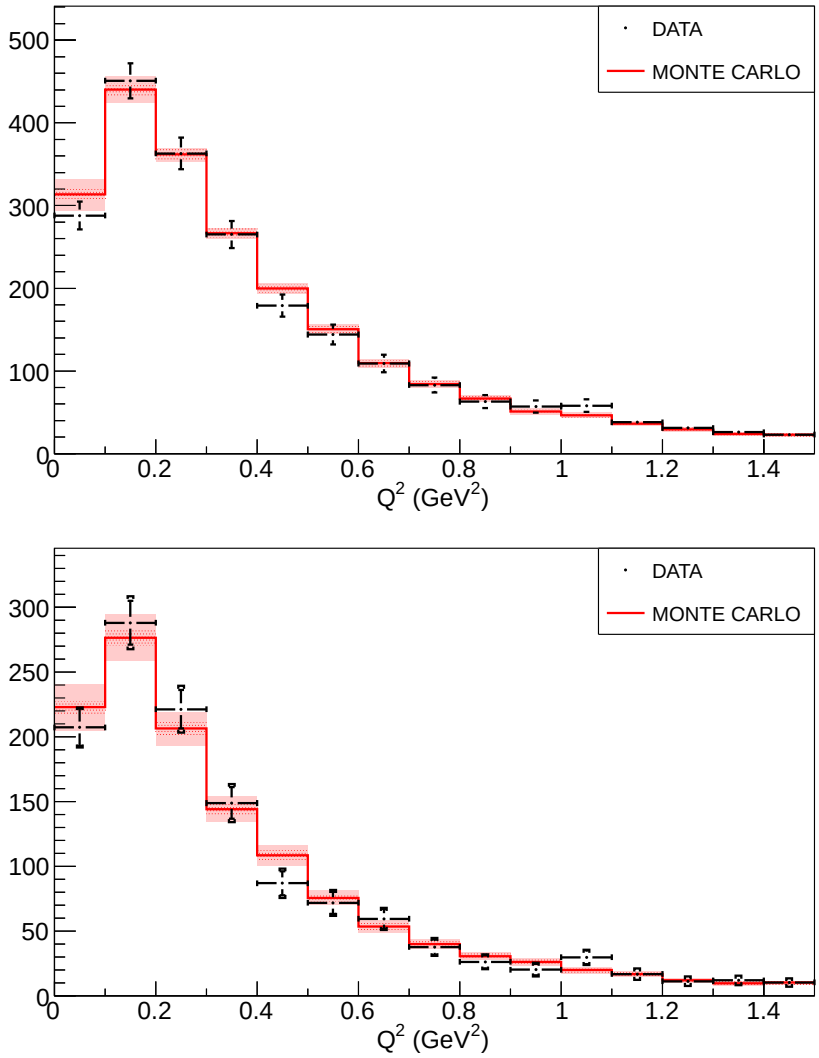

Figure 7.9: Q^2 *with full errors.* The Monte Carlo bands use dotted area to show the statistical error, and solid area to shown the total (statistical plus correlated) error. Top: without subtraction, equal to Fig. 7.6(e) with rebinning. Bottom: with subtraction, equal to Fig. 7.8(e) with rebinning.

are decided, the universe creates its own histogram of the Monte Carlo part of Fig. 7.9. At the end, the spread of the thousand M.C. histograms is computed, and this is the source of the M.C. error band in Fig. 7.9. For data, the same thousand-universes method is followed, but the only parameter varied is the background scale.

After all errors are computed, the magnitude of the Monte Carlo error is rougly equal to the magnitude of the data error. Despite their coincidental similarity in magnitude, the errors mean different things. The largest contributor to the Monte Carlo error is cross-section uncertainty. From this and other sources of error, the M.C. error is fully correlated. The data includes a background scale error, which is correlated, but the statistical (uncorrelated) error dominates, so the data total error is virtually uncorrelated.

7.3 Production of Confidence Intervals

The axial mass M_A^Δ itself has not been varied as a systematic error. But since this parameter can be altered by event reweighting, the same as the parameters in Table 4.1, it is convenient to use this technique to set arbitrary values of the axial mass in the Monte Carlo.

The default setting is $M_A^\Delta = 1.12$ GeV. I vary this in increments of 20%, from 0.45 GeVto 1.79 GeV. Figures 7.10–7.11 show the Monte Carlo with these seven points of M_A^Δ. The data has been overlaid on each panel and does not vary from panel to panel.

We define the χ^2 comparison of data to Monte Carlo. The data-M.C. difference, $\delta_i^k = N_{\text{data}}^k - N_{\text{M.C.}}^k$, where the index $i = 1 \ldots 15$ runs over the fifteen

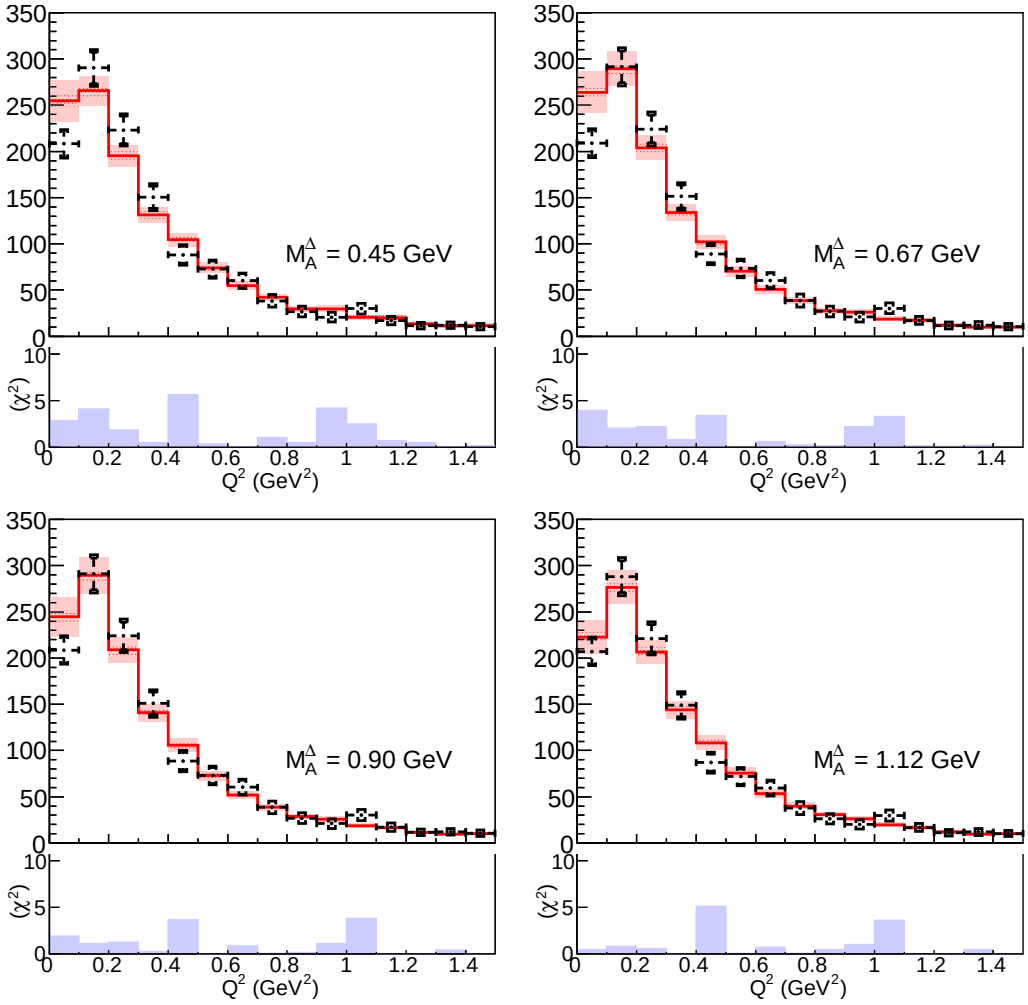

Figure 7.10: *Varied M_A^Δ (1).*

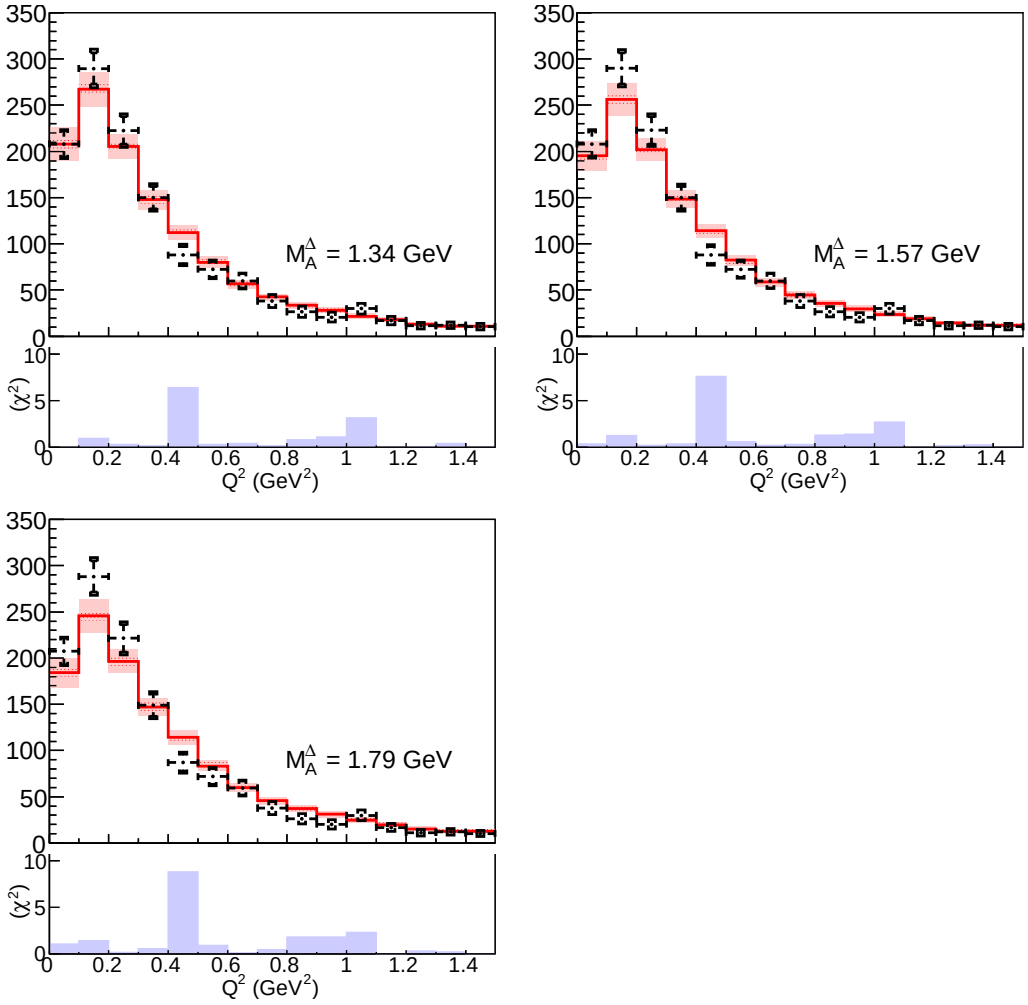

Figure 7.11: *Varied M_A^Δ (2).*

bins of Q^2 and the index $k = 1 \ldots 1000$ runs over the parameter universes, is turned into a covariance matrix V_{ij} by $V_{ij} = \left\langle \delta_i^k \delta_j^k \right\rangle_{(k)} - \left\langle \delta_i^k \right\rangle_{(k)} \left\langle \delta_j^k \right\rangle_{(k)}$. The averages are taken over the thousand parameter universes. Then χ^2 is computed as $\chi^2 = \sum_{i,j} \{V^{-1}\}_{ij} \delta_i^0 \delta_j^0$ (where δ with superscript 0 represents no perturbation of parameters).

In Figs. 7.10–7.11, the contribution to χ^2 from each bin is shown in the small histogram below each panel. The deviations are evenly distributed across the range of Q^2, despite the widely varying magnitude (of both counts and error) over that range, although the bin centered at $Q^2 = 0.45$ GeV^2 seems to be a severe outlier. The summary of χ^2 versus M_A^Δ is plotted in Fig. 7.12.

If the model is good, then we recall from formal statistics that the most probable value for $\chi^2_{\rm min}$ is D.O.F. $- 2$. The number of D.O.F. in our case is 15, since the 15 bins from $Q^2 = 0$ to $Q^2 = 1.5$ GeV^2 are completely independent. (Area normalization is enforced, but this only constrains the value of the overflow bin with respect to the 15 indepedent bins.) Thus, we expect $\chi^2_{\rm min} = 13$.

To extract $\chi^2_{\rm min}$, I interpolate the seven points with a quartic polynomial. From the minimum of the interpolation function, we find $M_A^\Delta = 1.15$ GeV (best value) with $\chi^2_{\rm min} = 13.1$. To produce the 68% (90%, 95%) confidence band, I find the intersections of the interpolation function with $y = \chi^2_{\rm min} + \Delta\chi^2$ where $\Delta\chi^2 = 1.00$ (2.70, 4.00). The results are summarized in Table 7.1.

The lowest bins of Q^2 are the most informative. To demonstrate this (Fig. 7.13), I plot χ^2 vs. M_A^Δ for different ranges of Q^2. The top, blue curve is with no changes and is equal to Fig. 7.12. For the red curve, the tail end of the Q^2 spectrum has been masked ($Q^2 < 1.0$ GeV^2). In this scenario, $\chi^2_{\rm min}$ changes

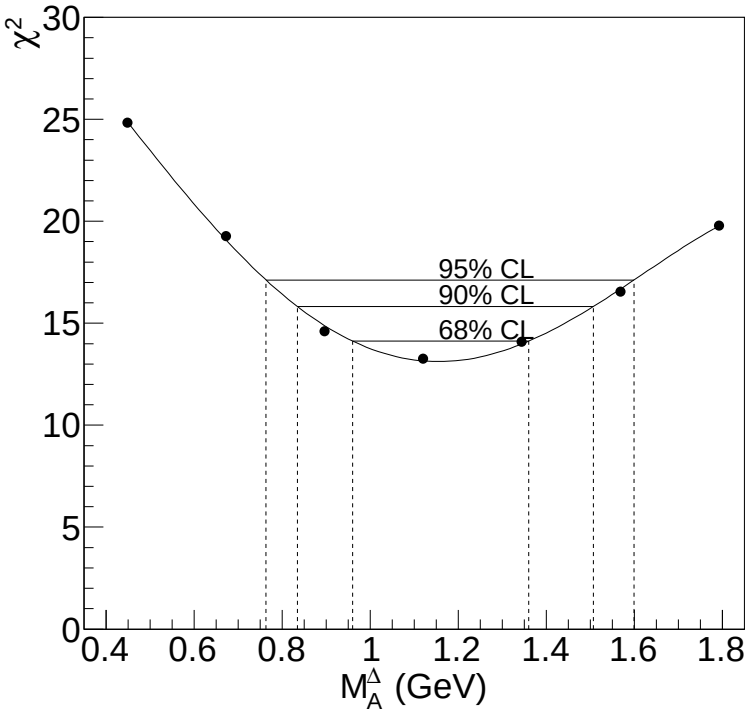

Figure 7.12: *Confidence intervals of* M_A^Δ, from 7 trial points. The points are interpolated by a quartic polynomial.

$\Delta\chi^2$	C.L. (approx.)	Interval (GeV)
1.00	68%	0.96–1.36
2.70	90%	0.83–1.51
4.00	95%	0.76–1.60

Table 7.1: Confidence intervals of M_A^Δ.

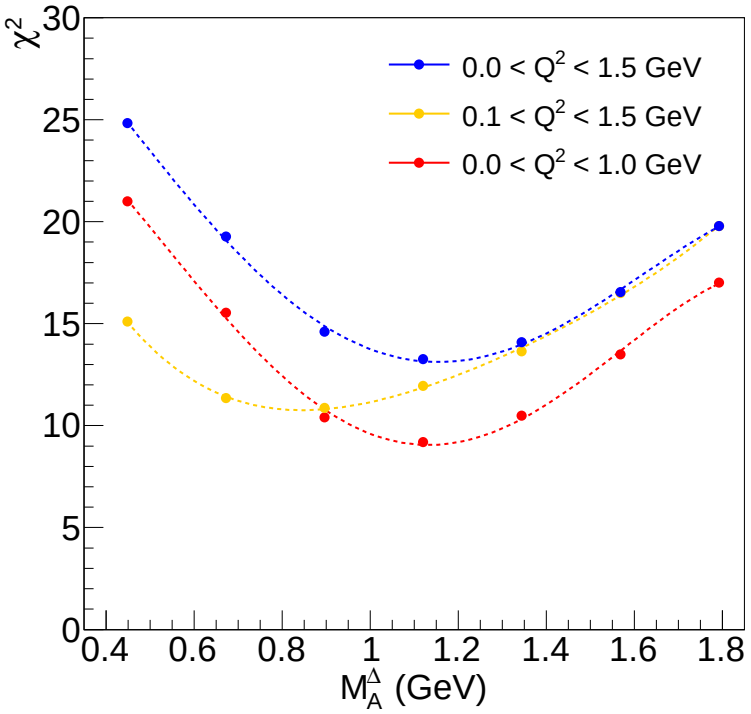

Figure 7.13: χ^2 *vs.* M_A^Δ *for alternate ranges of* Q^2.

because there are now five fewer degrees of freedom (D.O.F.). However, the shape of the curve, and the confidence intervals, change very little.

On the other hand, if I remove only the first bin (yellow curve, $Q^2 > 0.1$ GeV^2), the result changes dramatically and χ^2_{min} sinks to just above 10. The reduction of χ^2_{min} is greater than 2, but D.O.F. is only one fewer. This anomoly suggests that the data does not make sense without the first bin.

In the scenario with the first bin masked, the unusual best value of $M_A^\Delta \approx 0.8$ GeV might be explained by the vector mass $M_V = 0.84$ GeV. It is suggested by Figure 1.1 that the $(C_5^A)^2$ term is the dominant term in the cross-section at $Q^2 < 0.1$ GeV^2, but this term decreases dramatically as Q^2 increases, and it is overtaken by the cross-term $C_3^V C_5^A$. The cross-term is similar in shape to the pure vector term $(C_3^V)^2$. It seems impossible to distinguish vector from axial-vector unless the limit as $Q^2 \to 0$ is probed.

Chapter 8 Future Prospects

This chapter contains notes on possible continuations of the analysis.

- *Statistics.* Since the MINERvA experiment will continue running in different beam configurations, the statistical part of the M_A^{Δ} uncertainty can be reduced, even if no other changes to this analysis are made. Further running will take the measurement into a systematics-limited mode, since the statistical error is comparable to the systematic at the present time.

- *Introduction of alternate models.* The Rein-Sehgal model [7] has been used because of a technical limitation in the available version of the GENIE [31] event generator. The measurement itself does not make reference to Rein-Sehgal. Other models can be applied by implementing them in the generator.

- *Negative pion (π^-) mode.* I relied on the Michel electron tag during development in order to obtain a relatively clean input stream for stopping particle I.D. Depending on the robustness of the I.D. and subtraction algorithms, it is conceptually possible to remove the requirement of the Michel electron tag, and identify pions (over a large proton background) by energy loss alone. If this were successful then first, the efficiency would increase by about 20% (this is referring to the 81% efficiency of the Michel electron finding algorithm by itself).

  More interestingly, however, it would allow a parallel analysis of MINERvA

antineutrino data, in the channel $\bar{\nu}\,N \rightarrow \mu^+\,\pi^-\,N'$. This data comes from periods of running in which the horn and MINOS N.D. magnetic fields had been set up in the other direction than usual, for π^- neutrino parent and μ^+ product focusing, respectively. The π^- has the same energy loss profile as the π^+, so the stopping particle I.D. would require no modification. However, the stopped π^- is typically destroyed by nuclear capture, leaving no signal. This final behavior makes it unlike the stopped π^+, which decays at rest and leaves the delayed e^- signal that is required by the analysis in its present form.

- *Subtraction of 2π background.* The cut on hadronic mass $\widetilde{W}$ cannot produce a 1π sample with more than about 70% purity, because the hadronic mass calorimetrically is subject to a 20% uncertainty (Fig. 5.4). On the other hand it is conceptually possible to subtract this background. B. Eberly [35] has done this subtraction in a similar analysis. This analysis could be improved by copying the method developed there.

- *Recovery of a fraction of resonant events at small T_N.* A moderate increase in efficiency could be achieved by making the coherent rejection cut more sophisticated. Within the sample at $T_N < 40$ MeV, the Monte Carlo prediction is that about half the events are resonant, and half coherent. (Of course, this prediction relies on the Monte Carlo cross-section for coherent production, which may not be correct). Very few coherent events fail the T_N cut.

  To rescue some of the lost resonant events at low T_N, it is conceivable to use the inverse of a coherent signal cut, borrowed directly from a coherent

analysis. The nuclear transfer $t = |q - p_\pi|$ (where q is the leptonic four-momentum transfer) is traditionally used in coherent signal analyses. For completion of the resonant analysis, it needs to be studied how t can be used with T_N to carve out a more powerful inverse selection of coherent events.

- *Proton track analysis.* 15% of the selected events have three reconstructed tracks. If the third track is presumed to be a proton, then it should correspond in direction and energy to the prediction of the recoiling nucleon from two-particle ($\mu\pi$) reconstruction. Verifying this correspondence would seem to be the first step to making use of the 3-track sample. Additionally, if the track had a stopping proton I.D. and the sample can be made large enough, 3-track analysis could be performed on the 3-track sample.

- *Alternate background removal.* The analysis as presented here used a sideband scaled by a ratio $1 + R$ to predict the background. A single R was used for the entire sample, although this assumption could stand to be nuanced. At small reconstructed energy ($T_\pi < 100$ MeV) the predicted background deviates from Monte Carlo (Fig. 6.11(a)), suggesting the background shape is different in this region.

  The sideband is also not the only way to measure background. In the limit of large numbers of events, the same result should be achieved by assigning each data event a weight of $w = N_{\text{signal}}(\chi^2_\pi)/N(\chi^2_\pi)$ (where N_{signal} and N come from the fit of signal shape plus background function to the measured distribution of χ^2_π). This cross-check should be

performed to give confidence to the signal-background separation.

- *Use of kinked pion tracks.* Only few pion tracks had more than one trackable segment (Fig. 5.5). Supposing that tracking efficiency for secondaries could be improved, it might become worthwhile to reconstruct kinked pions. This would entail making the energy reconstruction more sophisticated. Instead of relying on range alone, energy of scattering would be added back in at the scatter point(s).

- *Collection of reinteracted pion energy.* Most of the events currently subtracted as reacted pion background are inelastic scatters. If the energy of the pion post-scatter could be collected calorimetrically and added back in, this would produce a new (large) sample of events with a well-known pion energy. Direct comparison of the stopping sample to this sample would become possible. This would also boost statistics for the axial mass measurement.

Bibliography

[1] D. H. Perkins, "Nuclear Disintegration by Meson Capture," *Nature* **159** *126–127*, and G. P. S. Occhialini & C. F. Powell, "Nuclear Disintegration Produced by Slow Charged Particles of Small Mass," *Nature* **159** *186–190* (1947).

[2] D. Ashery *et. al.*, "True Absorption and Scattering of Pions on Nuclei," *Physical Review* **C23** *2173-2185* (1981).

[3] C. H. Llewellyn Smith, "Neutrino Reactions at Accelerator Energies," *Physics Reports* **3** *261–379* (1972).

[4] A. J. Dufner & Y. S. Tsai, "Phenomenological Analysis of the γNN^* Form Factors," *Physical Review* **168** *1801-1809* (1968).

[5] R. H. Capps & G. Takeda, "Dispersion Relations for Finite Momentum-Transfer Pion-Nucleon Scattering," *Physical Review* **103** *1877–1896* (1956).

[6] S. L. Adler, "Photo-, Electro-, and Weak Single-Pion Production in the $(3, 3)$ Resonance Region," *Annals of Physics* **50** *189–311* (1968).

[7] D. Rein & L. M. Sehgal, "Neutrino-Excitation of Baryon Resonances and Single Pion Production," *Annals of Physics* **133** *79–153* (1980).

[8] K. S. Kuzmin, V. L. Lyubushkin & V. A. Naumov, "Axial Masses in Quasielastic Neutrino Scattering and Single-Pion Neutrinoproduction on Nucleons and Nuclei," *Acta Physica Polonica* **B37** *2337–2348* (2006).

[9] E. A. Pascos, M. Sakuda & J. Y. Yu, "Neutrino Production of Resonances," *Physical Review* **D69** 014013 (2004).

[10] O. Lalakulich & E. A. Pascos, "Resonance Production by Neutrinos: I. $J = 3/2$ Resonances," *Physical Review* **D71** 074003 (2005).

[11] O. Lalakulich, E. A. Pascos & G. Piranishvili, "Resonance Production by Neutrinos: The second resonance region," *Physical Review* **D74** 014009 (2006).

[12] J. Bell *et. al.* (FNAL 15′ bubble chamber), *Physical Review Letters* **41** *1008–1011*, and J. Bell *et. al.*, *Physical Review Letters* **41** *1012–1015* (1978).

[13] P. Allen *et. al.* (CERN B.E.B.C. bubble chamber), *Nuclear Physics* **B176** *269–284* (1980).

[14] G. M. Radecky *et. al.* (Argonne bubble chamber), *Physical Review* **D25** *1161–1173* (1982).

[15] T. Kitagaki *et. al.* (Brookhaven bubble chamber), *Physical Review* **D34** *2554–2565* (1986) and T. Kitagaki *et. al.*, *Physical Review* **D42** *1331–1338* (1990).

[16] K. Hiraide *et. al.* (The SciBooNE Collaboraton), "Search for Charged Current Coherent Pion Production on Carbon in a Few-GeV Neutrino Beam," *Physical Review* **D78** 112004 (2008).

[17] A. A. Aguilar-Arevalo *et. al.* (The MiniBooNE Collaboration), "Measurement of Neutrino-Induced Charged-Current Charged Pion Production Cross-Sections on Mineral Oil at $E_\nu \sim 1$ GeV," *Physical Review* **D83** 052007, and http://www-boone.fnal.gov/for_physicists/data_release/ccpip/ (2011).

[18] J. Chvojka, "Anti-Neutrino Charged Current Quasi-Elastic Scattering in MINERvA" (Ph.D. dissertation), University of Rochester (2012).

[19] L. Aliaga *et. al.* (The MINERvA Collaboration), "Design, Calibration, and Performance of the MINERvA Detector," *Nuclear Instruments and Methods* **A743** *130–159* (2014).

[20] G. N. Perdue, conference talk at *Rencontres de Moriond* (2011).

[21] S. Kopp, "Accelerator neutrino beams," *Physics Reports* **439** *101–159* (2007).

[22] "NuMI Technical Design Report." Table 4.2-1 for Horn 2 Insertion Point, and Table 4.2-7 for Horn 2 shape equation. http://www-numi.fnal.gov/numwork/tdh/tdh_index.html (2004, only online).

[23] L. J. Loiacono, "Measurement of the Muon Neutrino Inclusive Charged Current Cross Section on Iron Using the MINOS Detector" (Ph.D. dissertation), Univerity of Texas at Austin (2010).

[24] Ž. Pavlović, "Observation of Disappearance of Muon Neutrinos in the NuMI Beam" (Ph.D. dissertation), University of Texas at Austin (2008).

[25] B. P. Ziemer, "A Measurement of the Two-track Charged Current Quasi-elastic Cross Section with the MINERvA Detector" (Ph.D. dissertation), University of California, Irvine (2012).

[26] C. M. Marshall, "The MINERvA Strip-To-Strip Calibration," MINERvA Technical Note No. 013, unpublished (2012).

[27] http://www.geant4.org/.

[28] D. S. Barton *et. al.* (E118 Collaboration), "Experimental Study of the *A*-Dependence of Inclusive Hadron Fragmentation," *Physical Review* **D27** *2580–2616* (1983).

[29] C. Alt *et. al.* (NA49 Collaboration), "Inclusive Production of Charged Pions in $p + C$ Collisions at 158 GeV/c Beam Momentum," *The European Physics Journal* **C49** *897–917* (2007).

[30] M. Kordosky, M. Jerkins & L. Aliaga, MINERvA DocDB 7403, unpublished (2012).

[31] C. Andreopoulos *et. al.*, "The GENIE Neutrino Monte Carlo Generator," *Nuclear Instruments and Methods* **A614** *87–104* (2010), "GENIE Physics and User Manual" (http://genie.hepforge.org/manuals/GENIE_PhysicsAndUserManual_20130615.pdf) (2013), and http://www.genie-mc.org/.

[32] H. Gallagher, "Summary Table of GENIE Uncertainties," MINERvA DocDB 7451, unpublished (2012).

[33] D. Zhang, Ph.D. dissertation, College of William and Mary (forthcoming).

[34] D. Zhang, MINERvA DocDB 9945, p. 27, Data efficiency of identifying rock muon tracks (v1.31); unpublished (2014).

[35] B. Eberly, talk at Fermilab Joint Experimental-Theoretical Seminar, 7 February, 2014, and Ph.D. dissertation, Pittsburgh University (2014).

[36] H. A. Bethe, "Zur Theorie des Durchgangs schneller Korpuskularstrahlen durch Materie" (Theory of the passage of fast corpuscular rays through matter), *Annalen der Physik* **5** *325–400* (1930), and J. Beringer *et. al.* (Particle Data Group), "Review of Particle Physics" §30 Passage of particles through matter, *Physical Review* **D86** 010001 (2012).

[37] M. J. Berger *et. al.* (National Institute of Standards and Technology), "PSTAR," Version 1.2.3, http://physics.nist.gov/star/ (2005, only online).

[38] W. H. Press *et. al.*, "Numerical Recipies in C," 2nd Edition, §2.9 Cholesky Decomposition (1992).

[39] W. Rudin, "Principles of Mathematical Analysis," 3rd Edition, §7.26 The Stone-Weierstrass Theorem (McGraw-Hill, 1976).

[40] N. Tagg *et. al.* (The MINERvA Collaboration), "Arachne—A Web-based Event Viewer for MINERvA,"
Nuclear Instruments and Methods **A676** *44-49* (2012).

[41] M. Berglund & M. E. Wieser, "Isotopic Compositions of the Elements 2009," *Pure and Applied Chemistry* **83** *397–410* (2011).

Appendix A
Monte Carlo Truth Persistence

In the course of development, the list of pion reinteractions from the detector simulation was needed. It was found that this information was not typically persisted, and no data structure for it existed already.

The following solution is worked out using GEANT4 [27] as the detsim software. In our scheme, the creation points and ending points of hadrons are saved at all generations down to a 5 MeV threshold of kinetic energy. This already takes care of all the *inelastic* pion scatters because GEANT4 actually destroys the inelastically scattering pion, and creates the scattered pion as a numerically distinct particle. However, this solution does not work for *elastic* pion scatters.

In the elastic case it becomes necessary to look at deeper information. Every particle in GEANT4 proceeds in *steps*. A typical step advances a particle a fraction of an interaction length. We found that a *process name* is associated with each particle step. The process name is a string that is available at each stepping action, to tell which physical process is occurring at that step.

At a step where the process name is the string Transport, this is a straight step or a small angle scatter and can be ignored. Other process names that sometimes occur have names like PionPlusInelastic (there is an "Inelastic" module for each hadron type). However, since inelastic processes occur only at destruction points for the reason explained above, they have already been

taken care of. The only process to be concerned about, it turns out, is the one with the name string hElastic. This process does elastic scattering for hadrons. We determined that hElastic points should be saved. The saving of hElastic points can be done for all hadrons at all energies, with the exception of neutrons below 5 MeV.

To present the data in a structure, each persisted particle will have a polyline associated with it, with a variable number of points. The minimum content of the polyline is the creation point and the ending point. If the number of points is greater than two, the intermediate points are the points where a hElastic process has occurred. The data stored for each point are position, time, momentum, and energy.

After running a simulation, it is confirmed that the the direct mother-daughter relationship organizes the hadrons into a tree, where the nodes of the tree are points from the set of polylines in the event. Further, it is confirmed that 3-momentum is conserved at each node, including hElastic points. An exception to 3-momentum conservation can occur when a product particle is below 5 MeV kinetic energy and is not persisted.

Appendix B

Inversion of Eq. (6.D)

Monte Carlo simulation has supplied us with a covariance matrix V. We will solve the matrix equation $V = S\,\mathrm{diag}({\sigma_1}^2 \ldots {\sigma_6}^2)\,S^T$ (Eq. 6.D) for six uncorrelated standard errors σ_i and the unit-diagnoal, upper triangular matrix S representing correlations.

This variant of a Cholesky decomposition solves the equation. An algorithm acting in-place on a 6-by-6 squary array is initialized with the elements of V. The elements are successively altered to become ${\sigma_i}^2$ on the diagonal and S_{ij} above or below the diagonal, as follows:

$$\begin{bmatrix} V_{11} & V_{12} & V_{13} & \cdots & V_{16} \\ & V_{22} & V_{23} & & \\ & & \ddots & & \vdots \\ & & & & V_{66} \end{bmatrix} \longrightarrow \begin{bmatrix} {\sigma_1}^2 & S_{12} & S_{13} & \cdots & S_{16} \\ & {\sigma_2}^2 & S_{23} & & \\ & & \ddots & & \vdots \\ & & & & {\sigma_6}^2 \end{bmatrix}$$

The diagonal elements S_{ii} are not stored since they are assumed to be 1.

The algorithm which performs this transformation is $O(n^3)$. In my implementation, pesudocoded below, I let the rows and columns be stored in 6-to-1 order, so that (e.g.) the $(0,0)$ element of the square array is V_{66}.

```
for (int i = 0; i < 6; ++i) {
  for (int j = 0; j < i; ++j) {
```

```
      for (int k = 0; k < j; ++k) {
        M(i,j) -= M(i,k)*M(j,k)*M(k,k);
      }
      M(i,j) /= M(j,j);
      M(i,i) -= M(i,j)*M(i,j)*M(j,j);
    }
  }
```

This implementation acts only on the upper triangle. Since V is symmetric and S is upper-triangular, the lower-triangular elements do not ever need to be accessed.

These properties of the algorithm are easy to verify. If V is diagnoal, the algorithm leaves the array invariant and $V_{ii} = {\sigma_i}^2$. Otherwise the algorithm decreases each diagonal element of the array. (The quantity subtracted from the diagonal element is strictly positive.) Physically, this means that the resolution σ_i gets better, not worse, by accounting for correlations.

Appendix C

Perturbation of a Fit Result

In §6.6, I suggest that a fit result should be perturbed around its minimum. This is done using the covariance matrix returned by the fit.

In the diagonal case, the covariance matrix element is $V_{ii} = {\sigma_i}^2$. To produce a perturbation, one simply chooses vector of a independent random Gaussians with standard deviations σ_i, and adds this random vector to the vector of best fit parameters.

We may extend this to take account of correlations. If $\vec{x}$ is a vector of random independent Gaussians with standard deviation of 1, and M is any matrix, then the covariance matrix of the quantities $M\vec{x}$ is $M^T M$. Thus, we have to solve $M^T M = V$ for the matrix M given the fit result covariance matrix V.

This is accomplished by the Cholesky decomposition. This algorithm is similar in structure to the one presented in Appendix B. It operates on the lower triangle of a square array and successively changes the elements of V into the elements of M. The upper-triangluar elements of M are assumed to be zero. It can be seen that in diagonal case, it simply takes the square root of each diagonal and returns the standard deviations $\sigma_i = \sqrt{V_{ii}}$.

```
for (int i = 0; i < N; ++i) {
  for (int j = 0; j < i; ++j) {
    for (int k = 0; k < j; ++k) {
```

```
            M(i,j) -= M(i,k)*M(j,k);
        }
        M(i,j) /= M(j,j);
        M(i,i) -= M(i,j)*M(i,j);
    }
    M(i,i) = sqrt(M(i,i));
}
```

After M has been found, a vector of random Gaussians is chosen and multiplied by M. The result is added to the vector of best parameter values. To produce another perturbation, a different initial vector of independent random Gaussians is chosen, but the decomposition does not have to be repeated.